

PE&RS

May 2022

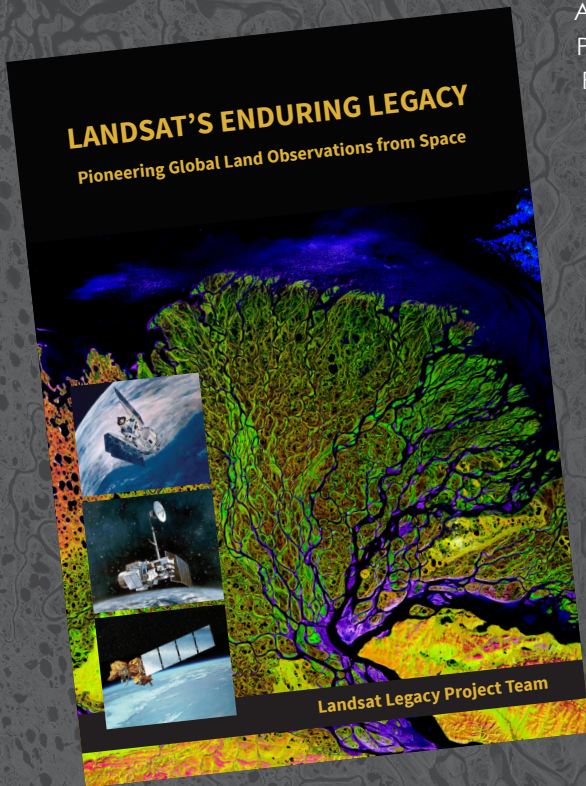
Volume 88, Number 5

PHOTOGRAMMETRIC ENGINEERING & REMOTE SENSING *The official journal for imaging and geospatial information science and technology*



LANDSAT'S ENDURING LEGACY

PIONEERING GLOBAL LAND OBSERVATIONS FROM SPACE



After more than 15 years of research and writing, the Landsat Legacy Project Team published, in collaboration with the American Society for Photogrammetry and Remote Sensing (ASPRS), a seminal work on the nearly half-century of monitoring the Earth's lands with Landsat. Born of technologies that evolved from the Second World War, Landsat not only pioneered global land monitoring but in the process drove innovation in digital imaging technologies and encouraged development of global imagery archives. Access to this imagery led to early breakthroughs in natural resources assessments, particularly for agriculture, forestry, and geology. The technical Landsat remote sensing revolution was not simple or straightforward. Early conflicts between civilian and defense satellite remote sensing users gave way to disagreements over whether the Landsat system should be a public service or a private enterprise. The failed attempts to privatize Landsat nearly led to its demise. Only the combined engagement of civilian and defense organizations ultimately saved this pioneer satellite land monitoring program. With the emergence of 21st century Earth system science research, the full value of the Landsat concept and its continuous 45-year global archive has been recognized and embraced. Discussion of Landsat's future continues but its heritage will not be forgotten.

The pioneering satellite system's vital history is captured in this notable volume on Landsat's Enduring Legacy.

Landsat Legacy Project Team

Samuel N. Goward
Darrel L. Williams
Terry Arvidson
Laura E. P. Rocchio
James R. Irons
Carol A. Russell
Shaída S. Johnston

Landsat's Enduring Legacy

Hardback. 2017, ISBN 1-57083-101-7
Student \$36*
Member \$48*
Non-member \$60*

* Plus shipping

Order online at
www.asprs.org/landsat



ANNOUNCEMENTS

URISA's GIS Hall of Fame Honors persons and organizations that have made significant and original contributions to the development and application of GIS concepts, tools, and/or resources, or the GIS profession.

Their contributions have had a significant and enduring impact on the GIS field or profession, and their work has benefited society as a whole.

Persons inducted into the GIS Hall of Fame have, in their work and professional conduct, exemplified vision, leadership, perseverance, community-mindedness, professional involvement, and ethical behavior.

URISA's Hall of Fame laureates include:

- 2005 Inductees: Edgar Horwood, Ian McHarg, Roger Tomlinson, Jack Dangermond, Nancy Tosta, and the Harvard Lab
- 2006 Inductee: Gary Hunter
- 2007 Inductees: Don Cooke and Michael Goodchild
- 2009 Inductees: Will Craig and Carl Reed
- 2010 Inductee: C. Dana Tomlin
- 2011 Inductees: William Huxhold and Barry Wellar
- 2012 Inductees: National Aeronautics and Space Administration, Natural Resources Canada, Statistics Canada, United States Census Bureau, and United States Geological Survey
- 2014 Inductee: Charles Croner
- 2016 Inductees: Alex Miller, Mark Monmonier, and Waldo Tobler
- 2018 Inductees: Peter Burrough and the National Oceanic and Atmospheric Administration
- 2021 Inductee: URISA's GISCorps

Anyone may nominate a person or organization for induction to URISA's GIS Hall of Fame. Nominations are due on or before May 31, 2022.

Visit <https://www.urisa.org/awards/urisa-gis-hall-of-fame-eligibility-criteria-and-nominations/> to learn about URISA GIS Hall of Fame eligibility criteria, nominations, and review process.



Phase One has named Globe Flight GmbH as its reseller of unmanned aerial vehicle (UAV) solutions in Germany and Austria. Based in Barbing, Germany, Globe Flight plans to make the Phase One P3 DJI M300 payload a centerpiece in its comprehensive drone offerings for inspection, surveying, and other geospatial applications.

The Phase One P3 payload addresses the previously unmet commercial need for high-resolution drone imaging while covering large surface areas quickly and safely. The P3 enables

Globe Flight to offer its customers a complete fully integrated drone solution for the first.

“Our P3 DJI M300 payload is a perfect complement to Globe Flight's existing products because it opens the door to millimeter-level imaging that was not available with other UAV camera systems,” said Carsten Wieser, Area Sales Manager for Central and Northern Europe at Phase One. “The P3 will appeal to Globe Flight's current customers and attract additional users in inspection sectors requiring extremely detailed drone images to inspect their infrastructure.”

Globe Flight is an ideal business partner for Phase One in the region, and the two companies will collaborate in Germany and Austria to further cultivate the market for UAV applications.

The German firm is an acknowledged UAV expert, offering a wealth of comprehensive solutions that include DJI sales and maintenance, product testing, regulatory advice, and pilot training. Globe Flight has traditionally equipped customers with DJI drones for use in inspection, surveying, agriculture, and others. The firm expects the P3 will expand these applications into the following specific areas:

- Inspection: Powerlines and power masts, wind turbine, bridges, railroad tracks, roads, building facades and roofs, oil and gas facilities (including flare towers), cell-phone tower, solar panels, dams, digital twins.
- Surveying: High-accuracy and wide-area mapping.
- Agriculture: Phenotyping, precision agriculture.

The P3 DJI M300 is a plug-and-play system ready to fly on a DJI Matrice 300 drone with a user-selected option of either the Phase One iXM 100MP or 50MP camera mounted on a new gimbal with integrated laser rangefinder. Phase One offers other drone payloads including versions for MAVlink supported drones and the DJI M600 Pro. All are designed primarily for fast, efficient, and safe inspection of critical infrastructure, yet versatile enough to handle any end user application.

The high-resolution medium-format metric Phase One iXM cameras have four RSM lens options and boast a dynamic range that guarantees sharp image collection in high-contrast or low-light environments. The variety of lens options ensures large surface areas can be captured with millimeter-level detail – even at safe distances from the asset. The new gimbal with the integrated laser rangefinder ensures precise and fast focusing on every shot, eliminating blurry and out-of-focus images, so that large features can be covered in fewer images and shorter missions.

Learn more at <https://geospatial.phaseone.com>



LatConnect 60 (LC60), an Earth observation and data fusion company based in Perth, Australia, has signed an agreement to work with Gilmour Space Technologies in Queensland to build and launch the first microsatellite in a planned high-resolution hyperspectral imaging constellation. The smart satellites will be placed in 30-degree inclined orbits for frequent revisit data capture over the Earth's equatorial and mid-latitude regions.

"HyperSight 60 will deliver geospatial insights for mid-latitude areas at a level of detail and frequency not possible with other commercial remote sensing systems," said Venkat Pillay, LC60 CEO and Founder. "The addition of Gilmour Space to the LC60 team contributes significantly to the future success of our ambitious plans."

Under the agreement, Gilmour Space will develop the first 100-kilogram HyperSight 60 satellite on its G-class satellite bus (G-Sat), which will be launched on Gilmour's Eris rocket from the Bowen Orbital Spaceport in Queensland, ideally located to place satellites into equatorial and mid inclined orbits. The microsatellite and subsequent constellation will be owned and operated by LC60.

"This agreement would be our second G-class satellite mission on Eris, and we're excited to be working with the pioneering team at LC60 to bring this significant capability to market," said Gilmour Space CEO, Adam Gilmour.

The first HyperSight 60 microsatellite is planned for launch in Q4 2024. Once the entire eight-satellite constellation is operational, an hourly revisit rate will be possible at mid-latitude locations between 30 degrees north and south in Australia,

Asia, South America, and Africa. This revisit, combined with the spectral bands collected in high- and medium-spatial resolution, will deliver timely information-rich insights for Agriculture, Forestry, Environmental, Mineral/Oil & Gas, Climate Change, Maritime, and Defence applications.

Established in 2019, LC60 currently owns exclusive rights to 80-centimeter imagery captured over Australia, with global access from a high-resolution multispectral satellite. The Perth-based company has leveraged this imagery along with other geospatial data sets to develop advanced artificial intelligence and machine learning-based data fusion and analysis algorithms for a variety of applications. Most notably, LC60 is now delivering insights to assist Southeast Asian palm and rubber plantations in improving productivity while enhancing environmental sustainability.

LC60 is also focused on designing 'smart' satellites equipped with onboard AI-based computing technology. For the HyperSight 60 constellation, this will enable 'tip-and-cue' capabilities among satellites within the constellation and allow pre-processing of data, including radiometric and geometric correction, to occur in orbit before the data is downlinked to the ground.

"For HyperSight 60 and other planned LC60 constellations, our unique approach to onboard AI sensors, combined with advanced data fusion on the ground, will fill gaps in the insights that can be gleaned from current remote sensing systems," said Pillay.

For more information, contact info@latconnect60.com.

CALENDAR

- 27 May, **ASPRS GeoByte—Deep Fake Geography? A Humanistic GIS Reflection upon Geospatial Artificial Intelligence**. For more information, visit <https://www.asprs.org/geobytes.html>.
- 23 September, **ASPRS GeoByte—Allen Coral Atlas: A New Technology for Coral Reef Conservation**. For more information, visit <https://www.asprs.org/geobytes.html>.
- 3-6 October, **GIS-PRO 2022**, Boise, Idaho. For more information, visit <https://www.urisa.org/gis-pro>.
- 23-27 October, **Pecora 22**, Denver, Colorado. For more information, visit <https://pecora22.org/>.



293 SIGNATURES INTRODUCING THE MURRAY STATE ASPRS STUDENT CHAPTER!

COLUMNS

- 285** GIS Tips & Tricks—Using GIS to Hunt for Easter Eggs – Part 2
- 287** Book Review— *Maths for Map Makers*
- 289** Grids and Datums Update
This month we look at the Kingdom of Sweden

ANNOUNCEMENTS

- 292** ASPRS Certifications
- 293** Signatures
The Column of the Student Advisory Council
- 295** In Memoriam— J. Ronald Eyton
- 297** Headquarters News
- 297** New ASPRS Members
Join us in welcoming our newest members to ASPRS.
- 298** GeoBytes

Call for *PE&RS* Special Issue Submissions

- 296** Modelling, Representation, and Visualization of the Remote Sensing Data for Forestry Management

DEPARTMENTS

- 281** Industry News
- 282** Calendar
- 299** Who's Who in ASPRS
- 301** ASPRS Sustaining Members
- 322** In-Press *PE&RS* Articles

303 Smartphone Digital Photography for Fractional Vegetation Cover Estimation

Gaofei Yin, Yonghua Qu, Alexandre Verger, Jing Li, Kun Jia, Qiaoyun Xie, and Guoxiang Liu

Accurate ground measurements of fractional vegetation cover (FVC) are key for characterizing ecosystem functions and evaluating remote sensing products. The increasing performance of cameras equipped in smartphones opens new opportunities for extensive FVC measurement through citizen science initiatives. However, the wide field of view (FOV) of smartphone cameras constitutes a key source of uncertainty in the estimation of vegetation parameters, which has been largely ignored. We designed a practical method to characterize the FOV of smartphones and improve the FVC estimation.

311 A Low-Cost and Portable Indoor 3D Mapping Approach Using Biaxial Line Laser Scanners and a One-Dimension Laser Range Finder Integrated with Microelectromechanical Systems

Xuzhe Duan, Qingwu Hu, Pengcheng Zhao, and Shaohua Wang

Existing indoor 3D mapping solutions suffer from high cost and poor portability. In this article, a low-cost and portable indoor 3D mapping approach using biaxial line laser scanners and a one-dimension laser range finder integrated with microelectromechanical systems is proposed.

323 Alternative Procedure to Improve the Positioning Accuracy of Orthomosaic Images Acquired with Agisoft Metashape and DJI P4 Multispectral for Crop Growth Observation

Toshihiro Sakamoto, Daisuke Ogawa, Satoko Hiura, and Nobusuke Iwasaki

Vegetation indices (VIs), such as the green chlorophyll index and normalized difference vegetation index, are calculated from visible and near-infrared band images for plant diagnosis in crop breeding and field management. The DJI P4 Multispectral drone combined with the Agisoft Metashape Structure from Motion/Multi View Stereo software is some of the most cost-effective equipment for creating high-resolution orthomosaic VI images. However, the manufacturer's procedure results in remarkable location estimation inaccuracy (average error: 3.27–3.45 cm) and alignment errors between spectral bands (average error: 2.80–2.84 cm). We developed alternative processing procedures to overcome these issues.

333 Robust Dynamic Indoor Visible Light Positioning Method Based on CMOS Image Sensor

Senzhen Sun, Guangyun Li, Yangjun Gao, and Li Wang

A real-time imaging recognition and positioning method based on visible light communication flat light source is proposed.

343 Comparing the Sensitivity of Pixel-Based and Sub-Watershed-Based Analytic Hierarchy Process to Weighting Criteria for Flood Hazard Estimation

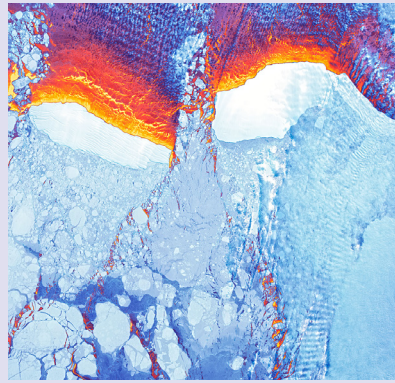
Hongping Zhang, Zhenfeng Shao, Wenfu Wu, Xiao Huang, Jisong Sun, Jinqi Zhao, and Yewen Fan

In flood hazard estimation via the analytic hierarchy process (AHP), using the pixel as the basic unit might lead to accuracy relying on the optimal weighting criteria. To this end, considering the sub-watershed as the basic unit is new. In this article, taking the Chaohu Basin in Anhui Province, China, as a study case, the accuracy of the sensitivity of the pixel-based and sub-watershed-based AHP models influenced by weighting criteria was compared.

See the Cover Description on Page 284

COVER DESCRIPTION

In summer 2019, a rift that began to accelerate across the Brunt Ice Shelf threatened to release an iceberg about twice the size of New York City. But as another Antarctic summer comes to an end, the ice shelf stubbornly continues to hold together. It has even escaped—so far—collisions with numerous icebergs that drifted nearby and threatened to pummel the shelf like an icy wrecking ball.



Throughout the austral summer of 2021-22, bergs in the eastern Weddell Sea drifted south with the Antarctic Coastal Current. Iceberg A-23A—currently the world's largest iceberg—floated freely after wiggling loose from the seafloor where it had been “grounded” (stuck) for decades. And in January 2022, iceberg D-28 rounded the Stancomb-Wills Glacier Tongue, floating roughly 4,300 kilometers (2,600 miles) from where it broke free of the Amery Ice Shelf in 2019.

The drift of the icebergs has slowed as daylight hours have waned and temperatures have dropped, allowing sea ice to start growing in earnest on the Weddell Sea. The bergs will eventually become fully encased in seasonal sea ice for the austral winter. But for now, their enormous size makes them effective bulldozers, still capable of plowing through the sea ice and leaving paths of open water behind them. Notice also the striking cloud bands near the sides of icebergs D-30A and D-28. These are likely the result of vortices in the air produced by the edges of the thick, table-like bergs.

More bands of clouds are visible north of the bergs. Clouds like these, known as cloud streets or convective roll clouds, often line up when strong, cold winds blow over comparatively warm ocean water. In this instance, the air blowing off Antarctica was “quite cold,” according to Bart Geerts, an atmospheric scientist at University of Wyoming. Geerts inferred from the ERA5, a reanalysis product from the European Centre for Medium-Range Weather Forecasts (ECMWF), that the winds that day were blowing from the southwest and would have been about -20°C (-4°F).

The relative warmth of seawater behind the icebergs and within leads in the sea ice is apparent in this month's cover image, acquired on March 9 by the Landsat 8 satellite. The image is false-color, created by blending data from the satellite's Operational Land Imager (for detail and texture) and its Thermal Infrared Sensor (TIRS). The warmest areas (yellow, orange, and red) depict open water and thin, newly formed sea ice. The coldest areas (blue and white) are older, thicker ice, including the icebergs and broken ice rubble in their paths.

<https://landsat.visibleearth.nasa.gov/view.php?id=149592>

NASA Earth Observatory images by Joshua Stevens, using Landsat data from the U.S. Geological Survey, and MODIS data from NASA EOSDIS LANCE and GIBS/Worldview. Story by Kathryn Hansen with image interpretation by Christopher Shuman, NASA/UMBC, and Bart Geerts, University of Wyoming.

Landsat imagery courtesy of NASA Goddard Space Flight Center and U.S. Geological Survey

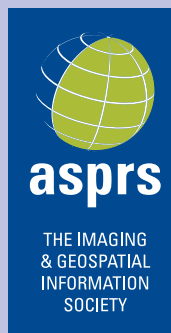
Be a part of ASPRS Social Media:

 facebook.com/ASPRS.org

 linkedin.com/groups/2745128/profile

 twitter.com/ASPRSorg

 youtube.com/user/ASPRS



PHOTOGRAMMETRIC ENGINEERING & REMOTE SENSING

JOURNAL STAFF

Publisher ASPRS

Editor-In-Chief Alper Yilmaz

Director of Publications Rae Kelley

Electronic Publications Manager/Graphic Artist

Matthew Austin

Photogrammetric Engineering & Remote Sensing is the official journal of the American Society for Photogrammetry and Remote Sensing. It is devoted to the exchange of ideas and information about the applications of photogrammetry, remote sensing, and geographic information systems. The technical activities of the Society are conducted through the following Technical Divisions: Geographic Information Systems, Photogrammetric Applications, Lidar, Primary Data Acquisition, Professional Practice, Remote Sensing Applications, and Unmanned Autonomous Systems Division. Additional information on the functioning of the Technical Divisions and the Society can be found in the Yearbook issue of *PE&RS*.

Correspondence relating to all business and editorial matters pertaining to this and other Society publications should be directed to the American Society for Photogrammetry and Remote Sensing, 8550 United Plaza Boulevard, Suite 1001, Baton Rouge, LA 70809, including inquiries, memberships, subscriptions, changes in address, manuscripts for publication, advertising, back issues, and publications. The telephone number of the Society Headquarters is 301-493-0290; the fax number is 225-408-4422; web address is www.asprs.org.

PE&RS. *PE&RS* (ISSN0099-1112) is published monthly by the American Society for Photogrammetry and Remote Sensing, 425 Barlow Place, Suite 210, Bethesda, Maryland 20814-2144. Periodicals postage paid at Bethesda, Maryland and at additional mailing offices.

SUBSCRIPTION. For the 2022 subscription year, ASPRS is offering two options to our *PE&RS* subscribers — an e-Subscription and the print edition. e-Subscribers can add printed copies to their subscriptions for a small additional charge. Print and Electronic subscriptions are on a calendar-year basis that runs from January through December. We recommend that customers who choose print and e-Subscription with print renew on a calendar-year basis.

The rate for a Print subscription for the USA is \$1105.00 USD, for Canadian* is \$1164.00 USD, and for Non-USA is \$1235.00 USD.

The rate for e-Subscription (digital) Site License for the USA and Non-USA is \$1040.00 USD and for Canadian* is \$1089.00 USD.

The rate for e-Subscription (digital) plus Print for the USA is \$1405.00 USD, for Canadian* is \$1464.00 USD, and for Non-USA is \$1435.00 USD.

*Note: e-Subscription, Print subscription, and e-Subscription plus Print for Canada includes 5% of the total amount for Canada's Goods and Services Tax (GST #135123065). **PLEASE NOTE: All Subscription Agencies receive a 10.00 USD discount.**

POSTMASTER. Send address changes to *PE&RS*, ASPRS Headquarters, 8550 United Plaza Boulevard, Suite 1001, Baton Rouge, LA 70809. CDN CPM #40020812).

MEMBERSHIP. Membership is open to any person actively engaged in the practice of photogrammetry, photointerpretation, remote sensing and geographic information systems; or who by means of education or profession is interested in the application or development of these arts and sciences. Membership is for one year, with renewal based on the anniversary date of the month joined. Membership Dues include a 12-month electronic subscription to *PE&RS*. To receive a print copy of *PE&RS* there is an additional postage fee of \$60.00 USD for U.S. shipping; \$65.00 USD for Canadian shipping; or \$75.00 USD for international shipping per year. Annual Individual Member dues for members residing in the U.S. and Other Foreign Members are \$150.00 USD and \$158.00 USD for Canadians. Annual Student Member dues for members residing in the U.S. are \$50.00 USD; \$53.00 USD for Canadian; and \$60.00 USD for Other Foreign Members. A tax of 5% for Canada's Goods and Service Tax (GST #135123065) is applied to all members residing in Canada.

COPYRIGHT 2022. Copyright by the American Society for Photogrammetry and Remote Sensing. Reproduction of this issue or any part thereof (except short quotations for use in preparing technical and scientific papers) may be made only after obtaining the specific approval of the Managing Editor. The Society is not responsible for any statements made or opinions expressed in technical papers, advertisements, or other portions of this publication. Printed in the United States of America.

PERMISSION TO PHOTOCOPY. The copyright owner's consent that copies of the article may be made for personal or internal use or for the personal or internal use of specific clients. This consent is given on the condition, however, that the copier pay the stated per copy fee through the Copyright Clearance Center, Inc., 222 Rosewood Drive, Danvers, Massachusetts 01923, for copying beyond that permitted by Sections 107 or 108 of the U.S. Copyright Law. This consent does not extend to other kinds of copying, such as copying for general distribution, for advertising or promotional purposes, for creating new collective works, or for resale.

Using GIS to Hunt for Easter Eggs – Part 2¹

While writing GIS software is a big business and no laughing (or trivial) matter, ever since the early days of computer software programs, the authors have displayed their sense of humor, and creativity, by placing little “hidden features or Easter eggs” in their coding. Sometimes these hidden features would display the coders names when a special key sequence or click-pattern was detected. Other times, hidden features, likened to Easter eggs, would be revealed with key combinations. In this month’s column, I highlight two GIS Tips & Tricks that are hard-to-find and/or hard-to-remember.

HARD-TO-FIND TIP #1—YOU WANT TO CHANGE THE WAY YOUR MOUSE WHEEL WORKS

In ArcGIS-Desktop the default mouse wheel direction is to Zoom-OUT when rolling the mouse wheel forward, but in ArcGIS-Pro, the default is just the opposite; rotating the mouse wheel forward Zooms IN. Global Mapper’s default works like ArcGIS Pro. This can get very confusing and frustrating when switching between GIS programs, but there are options, albeit hidden, i.e., hard-to-find, in different menus.

FOR ARCGIS DESKTOP (10.X)

Use the Customize | ArcMap Options... from the Main Toolbar (Figure 1) and select the General Tab from the ArcMap Options dialog (Figure 2). Toward the bottom of the dialog are the options for the Mouse Wheel and Continuous Zoom/Pan graphic. Use the radio buttons to customize to your preferences.

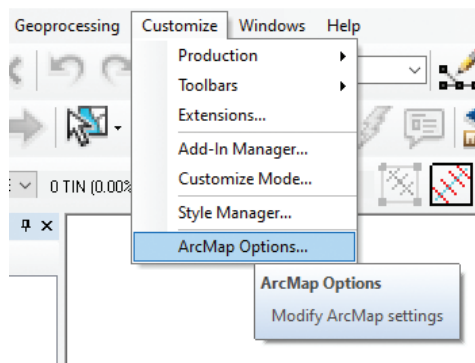


Figure 1. The Customize | ArcMap Options window in ArcGIS Desktop.

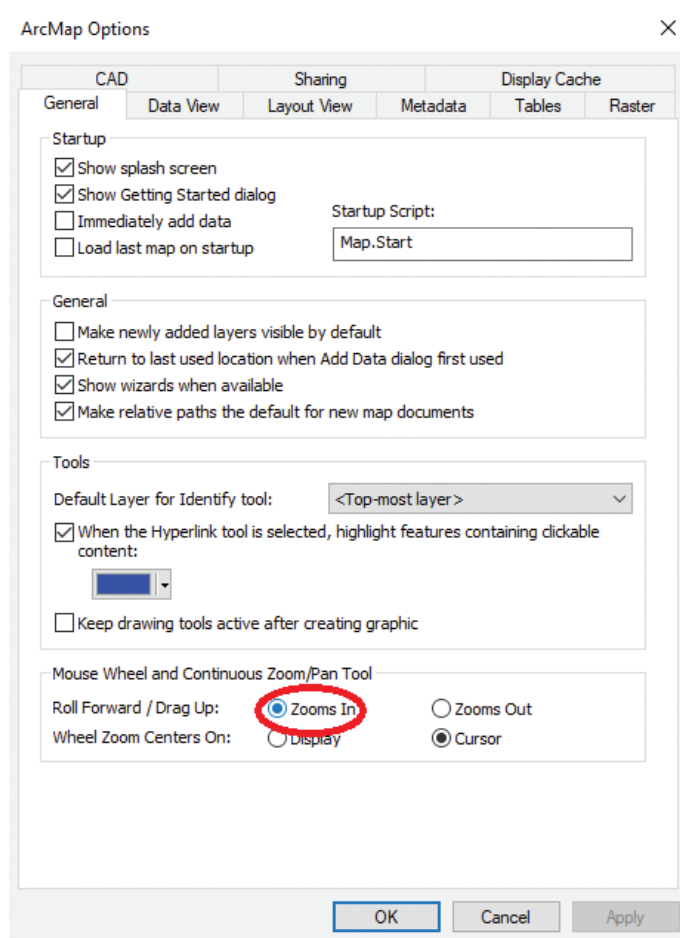


Figure 2. Change the behavior of the mouse wheel using the radio buttons

EXTRA HINT FOR ARCGIS DESKTOP

On this same dialog box, if you are planning on sharing your map document with others in your organization, it might be a good idea to check the:

“Make relative paths the default for new map documents” in the General portion of the dialog box.

Photogrammetric Engineering & Remote Sensing
Vol. 88, No. 5, May 2022, pp. 285-286.
0099-1112/22/285-286

© 2022 American Society for Photogrammetry
and Remote Sensing
doi: 10.14358/PERS.88.5.285

¹Using GIS to Hunt for Easter Eggs – Part 1 was published in the April 2021 issue of PE&RS.

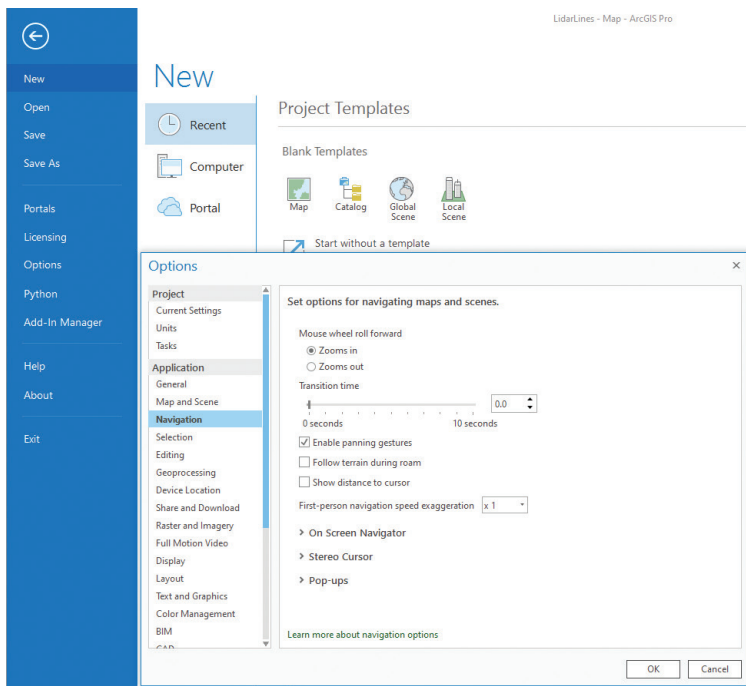


Figure 3. Use the Options | Navigation menu in ArcGIS Pro to modify the mouse wheel behavior.

FOR ARCGIS PRO (2.x)

Use the Project | Options and go to the Navigation Tab (Figure 3). On the top dialog, use the radio button to select your preference for the mouse wheel behavior.

IN GLOBAL MAPPER

The default is to Zoom-IN when rotating the mouse wheel forward. To change the behavior, use the Tools | Configuration Menu (Figure 4) and select the General tab. Midway on the General Tab is a checkbox to alter the mouse wheel direction (Figure 5).

BONUS MOUSE WHEEL TIP

While editing vector files, holding the <CTRL> key while “wheeling” may provide finer control over the zoom increment (thanks to Todd Waldorf of Dewberry for this one.)

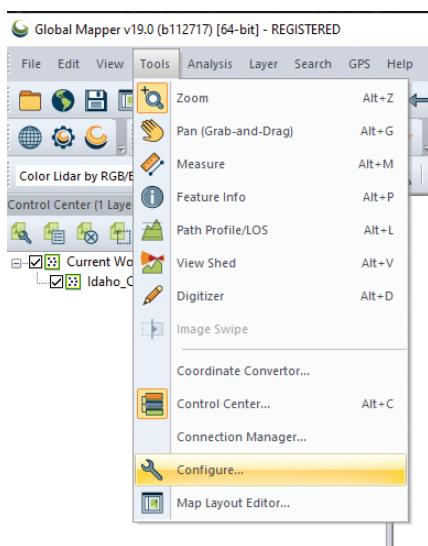


Figure 4. The Global Mapper Tools | Configuration options from the main menu bar.

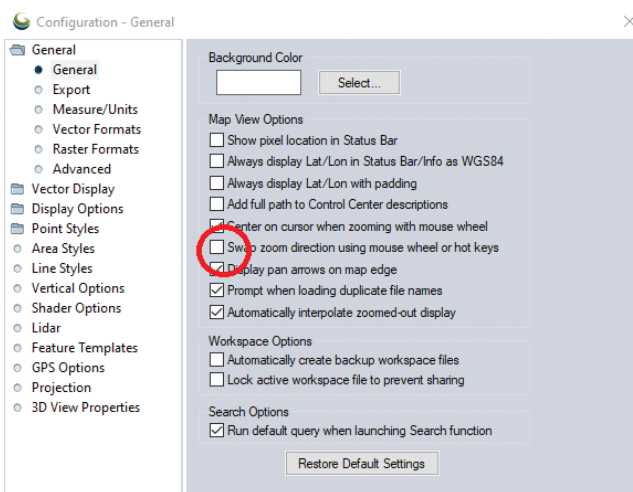


Figure 5. The “Swap zoom direction using mouse wheel or hot keys” checkbox in Global Mapper.

HARD-TO-REMEMBER TIP #2—ACCIDENTALLY CLOSING THE TABLE OF CONTENTS WINDOW IN ARCGIS DESKTOP

This is one of those newbie things that I allow my students to ask me 5 times before I start deducting points from their grade. And every semester, I have at least 20% of the class repeatedly ask... What happened to my Table of Contents? While the solution is actually not technically hidden, it is easy to forget.

IN ARCGIS-DESKTOP

To recover a closed Table of Contents, use the Windows | Table of Contents from the main menu (Figure 6).

You can also open the Arc

Catalog window and a Search window from this dropdown.

And that is all there is to a few simple, sometimes hard to find, GIS tricks. Easter eggs and other hard-to-find tricks can be found in all software packages. Please feel free to share yours with us. Send your questions, comments, and tips to GISTT@ASPRS.org.

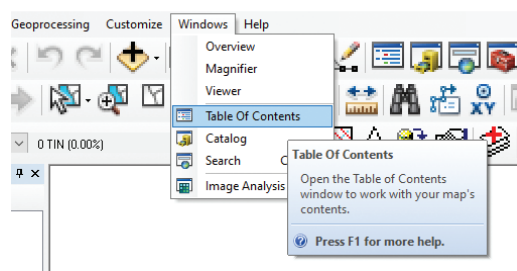


Figure 6. Opening the Table of Contents Window from the Main Menu bar.

Al Karlin, Ph.D., CMS-L, GISP is with Dewberry’s Geospatial and Technology Services group in Tampa, FL. As a senior geospatial scientist, Al works with all aspects of Lidar, remote sensing, photogrammetry, and GIS-related projects.

As some folks who know me know, I tend to gravitate to indices, I might even start reading a book in the appendices and seem to as I age to find that harder and harder to abstain from. I suppose years of work on updating a glossary that has yet to see the light of day may have played a part in driving me to that but in truth often savvy authors hide their best gems in the safety of an appendix.

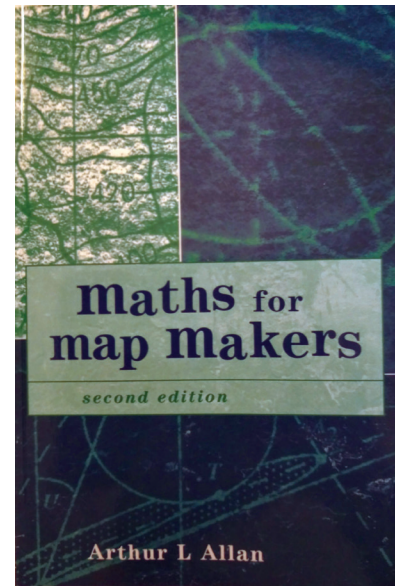
My first impression of “*Maths for Mapmakers*” came many years ago, being published first in 1997 while I was still a student. This impression might have been a groan or a comment something like, “*Maths*, what is that!?” but being so long ago I don’t rightly recall. Needless to say since that time, reissued, twice this text has brought *Maths* to a large swath of mapmakers for nearly a generation.

The book consists of 394 pages, divided into 13 chapters and a reference section including 4 appendices, a summary of formulae and an index. The author encourages all readers to pause for the “How to Read this Book” section and this reviewer concurs wholeheartedly. Here the author sections his book, placing chapters 1-5, which include (1) Numbers and Calculation, (2) Plane Geometry, (3) Trigonometry, (4) Plane Coordinates, (5) Problems in Three Dimensions, into a group that should be read and the problems worked in order as if one was building or reinforcing the foundation of mathematical understanding in mapping. Whereas the later chapters 6-13, which include (6) Areas and Volumes, (7) Matrices, (8) Vectors, (9) Calculus, (10) Conic Sections, (11) Spatial Trigonometry, (12) Solutions of Equations, (13) Least Squares Estimation, can be worked more like case studies on these foundations and not necessarily in the order they are found in the book. Essentially splitting the book into lower-level and upper-level courses in mapping mathematics.

Each chapter has a list of both formulae and “key words” or vocabulary words that should have been defined within its pages. I remember as a student the frustration and relief when I finally understood the chapter 6 key word “Hero’s Formula” was in the chapter 6 formula list as “ $\Delta = \frac{1}{2} bc \sin A$ ” and that was the same as the area of a triangle I already knew from Chapter 3, $\Delta = \sqrt{s(s-a)(s-b)(s-c)}$, where $2s = a + b + c$ [see, Equation (3.31) and Equation (6.2)]. Of course, had I not started my homework before reading the chapter, I probably would have had less frustration. Nevertheless, I did get an opportunity to fumble around in chapter 3 to refresh my acquaintance with triangles and their areas which did me no harm in the end.

Another anecdote of floundering around in Chapter 3 comes from Section (3.6) *Coordinate Axes and Bearings*. The complete anecdote is too lengthy for this book review, but

¹Dale, Peter “*Introduction to mathematical techniques used in GIS*,” CRC Press/Taylor & Francis, [2014].



Math for Map Makers

by Arthur L. Allan. Second Edition, 2011 reprint, Whittles Publishing, Scotland, UK. Originally published 1997.

Reviewed by Melissa J. Rura-Porterfield, Ph.D.
Memphis, Tennessee.

suffice to say in using Peter Dale’s book¹ “*Introduction to Mathematical Techniques Used in GIS*,” I came across his clarification of the difference between how a mathematician and a surveyor measure an angle [see, page 67, Figure (5.9) in Dale’s book] and although, this may sound like the beginning of a bad science joke; if you want to know the difference between how a mathematician, a surveyor, a cartographer, and a geographer measure an angle that is on page 63 in Figure (4.1) of Allan’s book. Dale’s explanation of just the mathematician and the surveyor is better equated to Section (3.6) in Allan’s book, but don’t start there, go to Figure (4.1) first and use it like the Rosetta Stone for angle measurements.

Although each chapter is the source of many useful exercises used to learn mathematics in mapping, one of the chief complaints of this text is there is no answer key printed in the book for these exercises. And subsequent printings have pages with ink shortage running down the left side margin. Generally, it is the margin calculator symbol to indicate

Photogrammetric Engineering & Remote Sensing
Vol. 88, No. 5, May 2022, pp. 287-288.
0099-1112/22/287-288

© 2022 American Society for Photogrammetry
and Remote Sensing
doi: 10.14358/PERS.88.5.287

an exercise problem that is obscured but in some places also words in a paragraph are also obscured. Moreover, the formulae and “key word” lists are in every chapter but as this reviewer looked for a list of figures for reference to her great disappointment there is none. The strength and usefulness of the many figures warranted a list that could be referenced. This reviewer understands the unnecessary extra work of naming each figure but indexing a Figure’s or Table’s chapter and section could have been very helpful.

List of Figures/Tables	Name	Chapter	Section
Figure (2.5 – 2.7)	Reference Grid	2	4
Figure (2.8)	Parallelogram, rectangle, square, and rhombus	2	5
Figure (2.9 - 2.10)	Pythagoras’s theorem for a right angled triangles	2	6

My take-home jewel from this text is in Appendix 3, page 368, another Rosette Stone, this time for Least Squares Estimation. How many times have I heard someone say, “He uses the Ohio State least squares notation, I don’t get it.” Or “He must have learned that notation from Purdue, I am lost?!” Here, we are all reminded that we may speak using many different notations, to solve many similar problems using similar assumptions to find and adjust for error. We must learn to communicate. Don’t give up, look-up! The answer is to be found!

Appendix A3: Notation for Least Squares

Author	Observation Matrix	Weight Matrix	Normal Equations Matrix	Dispersion Matrix
Allan ⁷	$Ax + L = v$ $Ax + Cv + L = 0$	W	$Nx = b$	D
Cooper ^{1,6}	$Ax = B + V$ $Ax + Bv = b$	W	$A^T W x = A^T b$ Note the lower case t	Q
American Manuel of Photogrammetry ²	$B\Delta - l = v$ $B\Delta - l = Av$	P	$B^T P \Delta = B^T P l$	Q
Mikhail ³	$A(l + v) = d$ $Av + B\Delta = f$ $C\Delta = g$	W	N	Q
Wolf ⁴	$AX = L + V$	W	$Nx = A^T L$	Q
Koch ⁵	$X\beta = y + e$	P	$X^T X \beta = X^T y$	D

¹M.A.R. Cooper, 1987, *Control Surveys in Civil Engineering*, Collins (ISBN 0-00-383183-3,381Pages)

²American Society of Photogrammetry, 1966, *Manual of Photogrammetry*, Library of Congress Catalog No 65-20813 Vol 1

³E. M. Mikhail, 1976, *Observations and Least Squares*, Dun-Donnelley, (ISBN 0-7002-2481-5, 497 Pages)

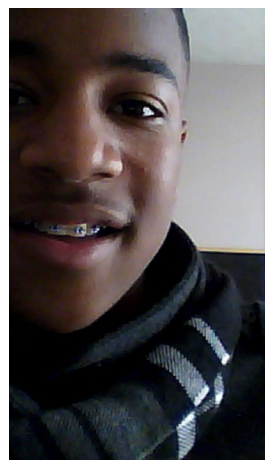
⁴P.R. Wolf and C.D. Ghilani, 1997, *Adjustment Computations*, Wiley (ISBN 0-471-16833-5, 564 pages)

⁵K.R. Koch, 1997, *Parameter Estimation and Hypothesis Testing in Linear Models*, Springer (ISBN 3-540-65257-4 325 pages)

⁶M.A.R. Cooper and P.A. Cross, 1988, Statistical Concepts and the Application in Photogrammetry and Surveying, *Photogrammetric Record*, Vol XIII, No 73, 645-678

⁷A.L. Allan and N. Atkinson, “Back to Basics’ Series Nos 14 to 24 – Least Squares Statistics and all that, Survey Review, Vols 35 and 36 Nos 272 to 282

This reviewer does recommend this text to a large swath “of geomatics including surveying, cartography and photogrammetry, geography and civil engineering and for the use in industry or academia” as the book’s back cover suggests, but I suppose many of us have known that for years.



Too young to drive the car? Perhaps! But not too young to be curious about geospatial sciences.

The ASPRS Foundation was established to advance the understanding and use of spatial data for the betterment of humankind. The Foundation provides grants, scholarships, loans and other forms of aid to individuals or organizations pursuing knowledge of imaging and geospatial information science and technology, and their applications across the scientific, governmental, and commercial sectors.

Support the Foundation, because when he is ready so will we.

asprsfoundation.org/donate





& GRIDS & DATUMS

BY Clifford J. Mugnier, CP, CMS, FASPRS

The Grids & Datums column has completed an exploration of every country on the Earth. For those who did not get to enjoy this world tour the first time, *PE&RS* is reprinting prior articles from the column. This month's article on the Kingdom of Sweden was originally printed in 2004 but contains updates to their coordinate system since then.

Inhabited during the Stone Age, several independent tribes lived in Sweden by the 9th century A.D. During that time, those adventurous tribes were among the Scandinavians known as the Vikings. Loosely united and converted to Christianity a couple centuries later, the Swedes conquered the Finns; they joined Norway and Denmark, and finally broke away in 1537 under Gustav I Vasa. Sweden became a constitutional monarchy in 1809.

Sweden is mostly flat with gently rolling lowlands; there are mountains in the west along the Norwegian border, and the kingdom is slightly larger than California. The lowest point is the reclaimed bay of Lake Hammarsjön, near Kristiansstad (-2.41 m); the highest point is Kebnekaise (2,111 m).

According to the Lantmäteriet, "The '*geometriska jordeböcker*' are the oldest large-scale maps in Sweden. One of the main tasks of the Land Survey following its establishment in 1628 was to carry out the mapping of villages and individual farms and their lands. It was primarily Crown farms that were the focus of interest. Cultivated fields and meadowland were mapped and information concerning yields and other information related to income and economic matters was collected. It is not clear whether the original purpose of the mapping was, in fact, to form the basis for taxation, but it can definitely be seen as the predecessor to the Swedish land use maps (*Ekonomiska kartan*). The maps are unevenly distributed across Sweden. They are collected in large volumes sorted according to parish and district. The '*geometriska jordeböcker*' should not be confused with the Crown's standard '*jordböcker*' which cover landed properties and contain fiscal information about them. The Crown's '*jordböcker*' can be looked upon as being the first Swedish real property register and the '*geometriska jordeböcker*' as the first cadastral index maps. There are around sixty

THE KINGDOM OF SWEDEN



volumes for the period between 1630 and 1650. Most of the maps are at a scale of 1:5000. We have only included in this series the volumes that have been scanned and are in digital format. To find older '*geometriska jordeböcker*' which are not yet scanned, you should go to the series Cadastral Maps. In The Land Survey map archives there are more than a hundred volumes of maps titled '*geometriska jordeböcker*' dating from the latter half of the 1600s and the early part of the 1700s. The maps are at varying scales, although most of them are large-scale maps. They mainly comprise farm maps that were produced for taxation purposes, maps to be used as the basis for the recruitment of and provision of material support of soldiers, and maps needed for the organization of the return of land by the Church to the Crown."

During the early 18th century, the French scientist, Maupertuis joined with the Swedish astronomer, Celsius on the French expedition to Lapland for the determination of the length of a degree of the meridian arc. This was considered

Photogrammetric Engineering & Remote Sensing
Vol. 88, No. 5, May 2022, pp. 289-291.
0099-1112/22/289-291

© 2022 American Society for Photogrammetry
and Remote Sensing
doi: 10.14358/PERS.88.5.289

an expedition for insurance in case the sister trip to South America (Ecuador, *PE&RS* May 1999), was not conclusive in proving the shape of the Earth. The area chosen for the chain of north-south triangles is now the southern land border between Sweden and Finland. Starting at the Lutheran church steeple in the city of Torneå (Torne) on the Gulf of Bothnia, the chain extended northwards along the Torne River to the (now) Finnish town of Pello. Maupertuis published his book on the Lapland expedition in 1737.

Soon after the commencement of the constitutional monarchy, the military survey of the kingdom was begun in 1811. Sweden gave up Swedish Pomerania in return for Norway, which entered into a personal union with Sweden (1814-1905). A civilian mapping authority for the compilation of an economic map was formed in 1859. The military and civilian mapping agencies were consolidated in 1894 and was known as the *Rikets Allmänna Kartverk* (RAK). After a series of consolidations and mergers, the current national mapping organization of the National Land Survey (*Statens Lantmäteriet*) was formed in 1985.

According to a personal communication from Dr. Lars Sjöberg of 7 November 1980, “The first systematic triangulation of Sweden started in 1805. All calculations were made on the ellipsoid, for Northern Sweden on Svanberg’s ellipsoid and for Southern Sweden on Clarke 1880. For official maps (in general scale 1:100,000) Spens’ projection, was used for Southern Sweden (up to Lat 61° 30′) and a conform conic projection for Northern Sweden. In 1903 a new triangulation started in Southern Sweden. The calculations were made in plane coordinates (x, y) (Gauss-Hannover’s projection and Bessel’s ellipsoid). The scale in the net was determined from a Danish baseline, which was measured in 1838. A new measurement of the baseline was made in 1911 and that measurement differed significantly from the earlier one. In 1938, when 5 Swedish baselines and 6 azimuths had been measured, the scale and orientation of the nets (obtained from the above measurements) were compared. The measurements of the Swedish baselines agreed better with the 1911 measurements than with the observations of 1838. It was then decided to enlarge the net with a factor 1.00002 and turn it clockwise 0.00005 radians around a point in Southern Sweden. Up till then all calculations had been made in 6 different zones with the longitude of origin referring to ‘Stockholms gamla observatorium’ (The Old observatory of Stockholm), which is 18° 03′ 29.8″ E of Greenwich. The longitude of origin for each zone was 6° 45′ W, 4° 30′ W, 2° 15′ W, 0°, 2° 15′ E, and 4° 30′ E of Stockholm’s *gamla observatorium*. This system is still in use for large scale maps. [*Ed’s note: this letter from Dr. Sjöberg was dated 1980.*] In 1938, *Rikets Allmänna Kartverk* decided to reduce the number of projection zones to 3, namely 2° 15′ W, 0°, and 4° 30′ E for official maps with FE 1,500,000 m, 2,500,000 m and 3,500,000 m, respectively. In 1945, RAK decided to use only one projection zone for official maps namely 2° 15′ W with FE 1,500,000 m.

Common for all zones are that latitude of origin is 0° and FN is 0. The scale factor along the central meridian m_0 is 1.0000. For some official maps there is also a grid net in the UTM projection. This net is based upon the European Datum 1950 with $m_0 = 0.9996$ and FE 500,000 m.”

I later wrote back to Dr. Sjöberg in July of the following year and inquired about the Spens projection. In Dr. Sjöberg’s reply of 7 August 1981, “The Spens projection differs somewhat from the Lambert conic projection. Spens’ projection satisfied the following conditions:

1. The scale factor (m_0) along the parallels $\varphi_1 = 65^\circ 50' 20.4''$ and $\varphi_2 = 55^\circ 21' 19.4''$ are equal.
2. The minimum scale factor between φ_1 and φ_2 equals m_0^{-1} . The first condition yields $\log n = 9.9407276-10$ and $\varphi_0 = 60^\circ 44' 29.6''$

(These are Spens’ results from 1817 used in the tables of Spens projection. The correct values are $\log n = 9.94072828-10$ and $\varphi_0 = 60^\circ 44' 30.2''$.) From the second condition one obtains $m_0 = 0.997903542$. The x-axis of the Spens projection is the meridian 5° W of the Old Observatory of Stockholm, directed southward. The origin is located at the parallel circle 72°. The Spens projection was described by P.G. Rosen (1876) in *Den vid Svenska Topografiska Kartverket användes projektionsmetoden*, 32 pp. As far as I know there is no word ‘Gradblättern.’ ‘Karten’ means maps and ‘Gradblättern’ ‘degree maps.’ However I think you refer to the polyconic projection used for the old ‘Generalstabskarten’ in the north of Sweden. This means that the conic projection is used repeatedly at each $\frac{1}{2}^\circ$ parallel. Each map is made as a ‘Gradblatt’ limited by parallel circles of every $\frac{1}{2}^\circ$ and meridian of equidistance $1\frac{1}{2}^\circ$. Clarke’s ellipsoidal parameters were used. The arctriangulation in Lapland (Tornedalen) carried out in 1730-1736 under the supervision of the Paris Academy was repeated in 1801-1803. From these latter measurements Svanberg computed the Earth dimensions (published 1805).”

According to a paper published (in German) by Professor im Generalstabe Karl D. P. Rosén, Stockholm 1933, the Svanberg ellipsoid parameters used were $a = 6,376,797$ m and $1/f = 304.2506$. Similarly, the published parameters for the Clarke 1880 ellipsoid as used for the Northland projection were $a = 6,378,249.2$ m and $1/f = 293.465$. The specific formulae used in Sweden were discussed in 1951 by G.A. Rune in *Tabeller Till Gauss Hannoverska Projektion, Tables for Gauss’s Hanoverian Projection* where he states (in English) in the Preface, “For facilitating the computation of the modern triangulation of Sweden, begun in 1903, the General Staff professor of that time Dr. Karl D. P. Rosén introduced the Gauss’s Hanoverian projection, often called the Gauss-Krüger or, briefly, the Gauss’s projection, a projection well fitting Sweden with its marked extension in the meridian.” Note that the defining parameters of the Bessel 1841 ellipsoid are: $a = 6,377,397.155$ m and $1/f = 299.1528128$. All of the Swedish classical datums have the same origin at the

Old Stockholm Gamla Observatory where: $\Phi = 59^{\circ} 20' 32.7''$ N and $\Lambda = 18^{\circ} 03' 29.8''$ E. The triangulation of Sweden from 1903-1938 consisted of 170 triangles and was observed with Wanschaff and Hildebrand instruments achieved an average Ferrero's formula accuracy of 0.41". The later Swedish triangulation of 1939-1953 consisted of 222 triangles and was observed with Wild T-3 theodolites and achieved an average Ferrero's formula accuracy of 0.40". That classical triangulation is defined as the RT 38 (*rikstrianguleringen* 1903-1950) datum. It has been replaced with RT 90 also called *Rikets Koordinatsystem* 1990, which is a local geodetic datum based on the Swedish third national triangulation (1967-1982), and is also referenced to the Bessel 1841 ellipsoid. The corresponding plane coordinate system is denoted **NT 90 2.5 gon V 0:-15** and is obtained by a Gauss-Krüger Transverse Mercator projection of the RT 90 latitudes and longitudes. The Central Meridian is $\lambda_0 = 15^{\circ} 48' 29.8''$ E, the scale factor at origin $m_0 = 1.0$, and FE = 1,500 km. The Central Meridian was originally interpreted as "2.5 Gon West of the Old Observatory of Stockholm," but is now defined as relative to Greenwich (1 Gon = 0.9 degrees).

According to the *Lantmäteriet*, "The original map sheet system in Sweden is based on a grid in RT 90 2.5 gon V 0:-15 with the SW corner at (North. = 6100 000 m, East. = 1200 000 m), and NE corner at (North. = 7700 000 m, East. = 1900 000 m). This area is divided into 50 km squares, which are enumerated with 0 - 32 in South-North direction, and lettered with A - N in West-East direction. Each 50 km square can be subdivided into four 25 km topographic map sheet squares, or subdivided into 100 5x5 km cadastral map sheets, which are enumerated from South to North by 0 - 9. and lettered from West to East by a - j. This original basic map sheet system has been modified in several ways for the modern series of maps, but the basic grid square notation is still frequently used, for instance in the numbering of geodetic control points. For larger scale mapping (>1:10000) there are six different zones of Transverse Mercator projections used in Sweden, in order to reduce the map projection errors. The other 5 zones apart from '2.5 gon V' differ only in the longitude of the central meridians, which are spaced by 2° 15'. The boundaries of the projection zones are adjusted to follow administrative borders if possible. The coordinate system 'RT 90 5 gon V 61:-1' has the map projection parameters: Central meridian: 13° 33' 29".8 East Greenwich, False Easting: 100 000 m, False Northing: -6,100,000 m. Example of a point's coordinates in different coordinate systems: x (Northing) = 6,200,000.000; y (Easting) = 1,300,000.000 in 'RT 90 2.5 gon V 0:-15' x (Northing) = 6,195,783.588; y (Easting) = 1,440,736.999 in 'RT 90 5 gon V 0:-15' x (Northing) = 95,783.588; y (Easting) = 40,736.999 in 'RT 90 5 gon V 61:-1'."

"SWEREF 99 is a Swedish realization of ETRS 89. The processing of the GPS data was performed according to the EUREF guidelines and was based on observations made on permanent reference stations in Sweden (SWEPOS), Den-

mark, Finland (FinnRef), and Norway (SATREF) during the GPS-weeks 1014-1019 (June-July 1999).

SWEREF 99 coincides with WGS 84[G730] and WGS 84[G873] within some decimeters. Coordinates can be transformed from the Swedish coordinate datum RT 90, to SWEREF 99 through a 7-parameter transformation given below (estimated accuracy of 7 cm, 1 sigma, 2D). The ellipsoid used with SWEREF 99 is GRS 80: $a = 6378137 \frac{1}{f}$ = 298.257222101. SWEREF 99 replaces SWEREF 93 (the former realization of ETRS 89). If one prefers to define a transformation in the direction RT 90 to SWEREF 99, use the following parameters: $\Delta X = +414.1$ m, $R_x = +0.855$ arc seconds, $\Delta Y = +41.3$ m, $R_y = -2.141$ arc seconds, $\Delta Z = +603.1$ m, $R_z = +7.022$ arc seconds, and $\delta = 0.0$ ppm (scale = 1.0)."

For example latitude, longitude and height above the Bessel 1841 ellipsoid in RT 90: $\phi = 58^{\circ} 00' 01.213296''$ $\lambda = 17^{\circ} 00' 11.683659''$ $h = -5.397$ m, latitude, longitude and height above the GRS 80 ellipsoid in SWEREF 99: $\phi = 58^{\circ} 00' 00.0''$, $\lambda = 17^{\circ} 00' 00.0''$ $h = 30.000$ m. Much to my surprise, when I carefully examined the published parameters, I realized that the rotation convention is the same as that used by the United States and by Australia. Thanks to Professor Lars Sjöberg now of the Geodesy Group at the Royal Institute of Technology in Stockholm for his patient help many years ago.

The Kingdom of Sweden Update

Sweden operates the Nordic Geodetic Commission (NKG) Analysis Center and currently operates 90 GNSS station sites in cooperation with the EUREF permanent network. As of 2018, there were over 3900 current subscriptions to the SWEPOS (Swedish National network of permanent GNSS stations operated by Lantmäteriet). Of interest is that SWEPOS offers not only dual-frequency correction services, but a single frequency DGNSS service has been offered since 2016, something not offered by the U.S. National Geodetic Survey. The new national height system RH2000 was implemented in 2005 and consists of about 50,000 passive benchmarks. So far 247 municipalities have implemented the replacement of RH2000 for their legacy height systems. Sweden had upgraded its FG-5 Absolute Gravity Meter to an FG-5X (Like LSU currently uses), and has observed at 14 sites as well as at 96 sites with A-10 Absolute Gravity Meters and at 200 sites with Relative Gravity Meters. Furthermore, the superconducting gravity meter at Onsala Space Observatory installed in 2009 has been regularly calibrated by Lantmäteriet's FG-5/FG-5X in June 2018 which was the seventh performed calibration.

The contents of this column reflect the views of the author, who is responsible for the facts and accuracy of the data presented herein. The contents do not necessarily reflect the official views or policies of the American Society for Photogrammetry and Remote Sensing and/or the Louisiana State University Center for GeoInformatics (C⁴G).

This column was previously published in *PE&RS*.

STAND OUT FROM THE REST

EARN ASPRS CERTIFICATION

ASPRS congratulates these recently Certified and Re-certified individuals:

CERTIFIED MAPPING SCIENTISTS GIS/LIS

Xiangheng Yang, Certification #GS309

Effective January 24, 2022, expires January 24, 2027

CERTIFIED MAPPING SCIENTIST LIDAR

Jan Lee Van Sickle, Certification #L069

Effective December 9, 2021, expires December 9, 2026

CERTIFIED PHOTOGRAMMETRIST

Benjamin Downey, Certification #CP1666

Effective January 28, 2022, expires January 28, 2027

James B Gillis, Certification #CP1660

Effective August 25, 2021, expires August 25, 2026

Christopher Reagan, Certification #CP1663

Effective January 14, 2022, expires January 14, 2027

CERTIFIED LIDAR TECHNOLOGIST

Daniel Grosche, Certification #LT071

Effective February 4, 2022, expires February 4, 2025

Jacob Gresham, Certification #LT070

Effective October 4, 2021, expires October 4, 2024

CERTIFIED GIS/LIS TECHNOLOGIST

Devin Gerzich, Certification #GST310

Effective February 3, 2022, expires February 3, 2025

Tracy Ray, Certification #GST311

Effective February 8, 2022, expires February 8, 2025

RECERTIFIED PHOTOGRAMMETRIST

Paul Badr, Certification #R1011CP

Effective May 20, 2022, expires May 20, 2027

Qassim Abdullah, Certification #R900CP

Effective February 12, 2022, expires February 12, 2027

Jeffrey L. Padgett, Certification #R760CP

Effective February 20, 2021, expires February 20, 2026

Robert H. Tuck, Certification #R907CP

Effective February 12, 2022, expires February 12, 2027

Gerard J. Gouldson, Certification #R1058CP

Effective December 6, 2021, expires December 6, 2026

John F. Schuenemann, Certification #R1614CP

Effective January 30, 2022, expires January 30, 2027

Douglas Johnson, Certification #R1512CP

Effective November 7, 2021, expires November 7, 2026

Barbora Ubar, Certification #R1611CP

Effective January 12, 2022, expires January 12, 2027

Joshua Persson, Certification #R1316CP

Effective December 26, 2021, expires December 26, 2026

Cody Condron, Certification #R1616CP

Effective April 11, 2022, expires April 11, 2027

Sagar Shriram Deshpande, Certification #R1527CP

Effective March 14, 2022, expires March 14, 2027

Thomas Jeff Young, Certification #R1010CP

Effective March 21, 2022, expires March 21, 2027

RECERTIFIED MAPPING SCIENTISTS GIS/LIS

Peter Cormish, Certification #R250GS

Effective February 7, 2022, expires February 7, 2027

Connie Li Krampf, Certification #R247GS

Effective December 27, 2021, expires December 27, 2026

Jason Zilka, Certification #R286GS

Effective July 15, 2021, expires July 16, 2026

RECERTIFIED MAPPING SCIENTIST – REMOTE SENSING

Christopher Lippitt, Certification #R188RS

Effective November 5, 2020, expires November 5, 2025

Radha Krishna Kandukuri, Certification #R197RS

Effective October 18, 2021, expires October 18, 2026

RECERTIFIED MAPPING SCIENTISTS LIDAR

Srinivasan S. Dharmapuri, Certification #R012L

Effective April 30, 2022, expires April 30, 2027

ASPRS Certification validates your professional practice and experience. It differentiates you from others in the profession. For more information on the ASPRS Certification program: contact certification@asprs.org, visit <https://www.asprs.org/general/asprs-certification-program.html>.



INTRODUCING THE MURRAY STATE ASPRS STUDENT CHAPTER!

Student chapters represent an important part of our ASPRS community. The Student Advisor Council uses this column to shine the light on these hard-working students to honor their work and to introduce them to our larger geospatial community! This month we are highlighting the Murray State student chapter, based in Murray State University, Kentucky. This chapter is in the ASPRS Mid-South region.

The Murray State chapter consists of members majoring in various backgrounds, but who all are working diligently to inspire students of how awe-inspiring and powerful the subject photogrammetry and remote sensing can be. As of right now, since the chapter is relatively new, there are roughly seven members including Pamela Rodriguez (President), Logan McGowan (Vice President), Haley Stiles (Secretary), Atherton Milford (Treasurer), Melanie Johnson (Public Relations), Marshall Thompson, and Steven Collett. Together, this chapter is collectively working towards planning educational events around campus about the everyday usage of remote sensors, promoting ASPRS through upcoming workshops that can be available to others to learn GIS software, and encouraging others to become ASPRS members to learn about career opportunities and connect with mentors in the workforce.

Although COVID has made it difficult for this chapter to plan events, the Murray State Chapter is optimistic



about planning new events and activities in the future and is committed to sharing any opportunities to students in the meantime. To learn more, email Pamela Rodriguez prodriguez2@murraystate.edu.

If you are interested in participating in SAC activities:

- Join us every other Thursday from 10-11 am PST!
- Join us via this zoom link: <https://tinyurl.com/SACASPRSMeting>

				
<p>Pamela Rodriguez President</p>	<p>Logan McGowan Vice President</p>	<p>Atherton Milford Treasurer</p>	<p>Melanie Johnson Public Relations</p>	<p>Haley Stiles Secretary</p>

ASPRS STUDENT ADVISORY COUNCIL

LAUREN MCKINNEY-WISE
COUNCIL CHAIR
OSCAR DURAN
DEPUTY COUNCIL CHAIR
CHUKWUMA JOHN OKOLIE
COMMUNICATIONS COUNCIL MEMBER

TBD
EDUCATION & PROFESSIONAL NETWORKING CHAIR
ALI ALRUZUQ
DEPUTY EDUCATION & PROFESSIONAL NETWORKING CHAIR
TESINI PRECIOSO DOMBO
COMMUNICATIONS COUNCIL MEMBER

RABIA MUNSAF KHAN
COMMUNICATIONS COUNCIL CHAIR
KENNETH EKPETERE
CHAPTERS COMMITTEE CHAIR
FREDA ELIKEM DORBU
COMMUNICATIONS COUNCIL MEMBER



WHITTLES PUBLISHING

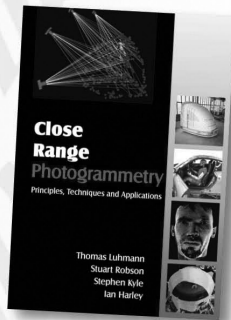
SIMPLY BRILLIANT BOOKS

ASPRS
MEMBER EXCLUSIVE

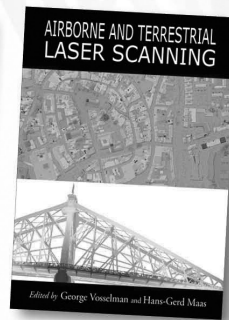
20%
DISCOUNT

ON ALL WHITTLES PUBLISHING BOOKS
USING CODE WPASPRS2

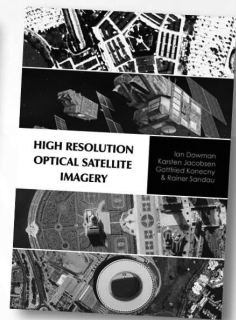
WHITTLES PUBLISHING'S STABLE OF CLASSIC GEOMATICS BOOKS INCLUDES THE THREE WINNERS OF THE PRESTIGIOUS KARL KRAUS MEDAL AWARDED BY ISPRS



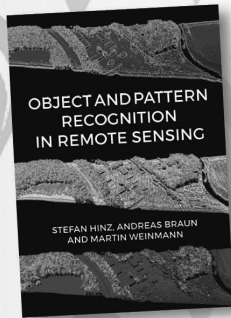
978-1870325-73-8
(Available as a CD)



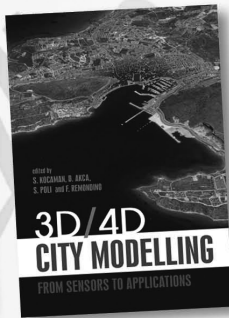
978-1904445-87-6



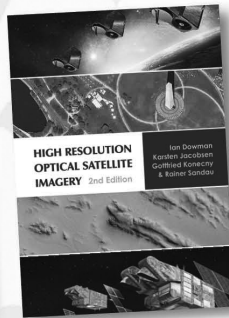
ISBN? Website only has 2nd edition



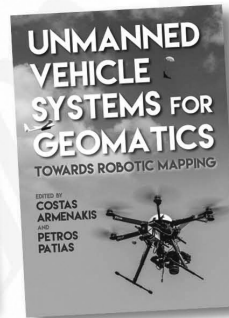
978-184995-128-9



978-184995-475-4



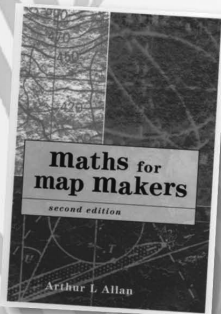
978-184995-390-0



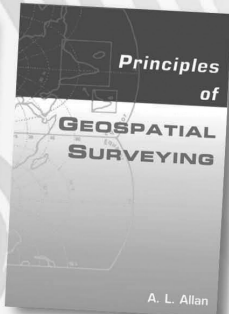
978-184995-127-2

OUR LIST CONTINUES TO EXPAND WITH THESE NEW TITLES

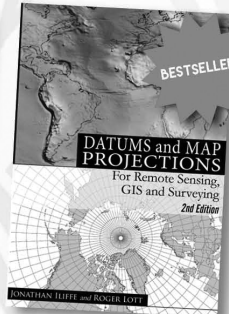
BROWSE OUR WEBSITE TO SEE OUR FULL RANGE OF ACCLAIMED GEOMATICS BOOKS



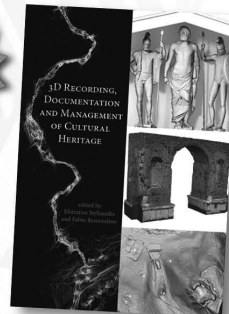
978-1870325-99-8



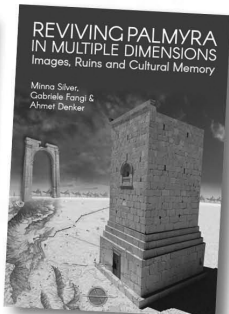
978-1904445-21-0



978-1904445-47-0



978-184995-168-5



978-184995-296-5

WWW.WHITTLES PUBLISHING.COM

J. Ronald Eyton

1942-2022

It is with a heavy heart that we announce the passing of our faculty colleague, Ron Eyton, on March 14, 2022. His death, in a hospital in Vancouver, BC, following a sudden illness was unexpected.

Ron was raised in Atikokan near present Thunder Bay, Ontario. Ron's father was a chemist at a local iron mine and helped Ron develop his life-long love of experimentation, photography, and cartography. Summer jobs in and around the mines convinced Ron to pursue a career in academic cartography. In a span of ten years, Ron completed degrees from Rochester Institute of Technology (AAS photographic science), the University of North Dakota (PhB, MS physical geography and geology), and the University of Illinois (PhD physical geography and photogrammetry). Ron's dissertation fitting first-degree trend surfaces to the flood plain and two terrace surfaces along a section of the Ohio River to determine if the terraces were of fluvial or lacustrine origin was published in the Geological Society of America Bulletin.

In the ten years following his doctorate, Ron held a variety of academic appointments at the Assistant (University of Illinois, University of South Carolina) and Associate (Penn State University, University of Alberta) Professor level. He was promoted to Professor of Earth and Atmospheric Sciences at Alberta however an institutional reorganization brought Ron to Texas State University in the Fall of 1995.

Ron was an important member of the Geography team which resulted in the Department of Geography being awarded the first doctoral program at Texas State University. Two sabbatical opportunities in his career resulted in visiting positions at the University of New South Wales and the University of Pittsburgh Semester at Sea program.

At the time of his retirement in 2006, Ron had supervised 10 doctoral and almost 30 master's students along with serving as a member of numerous doctoral and master's research advisory committees. Ron was best known to his students for his classes in cartography visualization and remote sensing. Ron wrote most of the analysis software used in these classes and freely shared his code with students. His photography hobby was made use of in the

classroom as his students were encouraged to fly with him and use his digital multiband camera systems to acquire and process their own data. His most popular class was "Digital Remote Sensing and Terrain Modeling" which he offered at both the undergraduate and graduate level.

Ron was committed to sharing the work of he and his students, publishing over 50 papers, and making over 30 professional presentations, many with his students as co-authors. Ron was in demand to share his expertise at invited lectures as well, making 46 presentation on digital terrain modeling and raster data processing to government and private sector groups in the US, Canada, and Australia. He also served as an instructor in short courses at annual meetings of the American Association of Geographers and the National Council on Geographic Education. His expertise and commitment to sharing was recognized with teaching and service awards at the local level as well as from the Canadian Institute of Geomatics and the American Society for Photogrammetry and Remote Sensing (ASPRS).

Retirement did not slow Ron. Accompanied by his spouse Lynne they traveled throughout the US and Canada, wherever Amtrack or VIA Rail would take them. After brief stops in southwest MN and eastern WA, they finally settled in Pemberton in the Sea to Sky country of Western British Columbia. We will all miss their annual Christmas calendar illustrated with images of their many travels. All of us send our best wishes to Lynne and their children Ben and Tammy. Our memory of Ron will always include a short sleeve white shirt, khaki shorts, and if outside, a white Tilly hat.

Persons wishing to remember Ron are asked to contribute to the ASPRS International Educational Literature Award (IELA). More information on the IELA and the ASPRS Foundation may be found at <https://www.asprs.org/education/asprs-awards-and-scholarships> and <https://www.asprsfoundation.org/>.

~ Richard W. Dixon and David R. Butler
Department of Geography and Environmental Studies
Texas State University

Modelling, Representation, and Visualization of the Remote Sensing Data for Forestry Management

Remote sensing data includes aerial photography, videography data, multispectral scanner (MSS), Radar, and laser to map and understand various forest cover types and features. An accurate digital model of a selected forest type is developed using forest inventory data in educational and experimental forestry and extensive databases. It includes the formalization and compilation of methods for integrating forest inventory databases and remote sensing data with three-dimensional models for a dynamic display of forest changes.

Big data technology employs vast amounts of forestry data for forestry applications that require real-time inquiry and calculation. The techniques and strategies of forestry data analysis are integrated into the big data forestry framework, enabling interfaces that other Programmes may call. Virtual Reality addresses constraints in forest management such as temporal dependence, irreversibility of decisions, spatial-quantitative change of characteristics, and numerous objectives. Virtual representations integrate various computer graphics systems with display and interface devices to create a spatial presence in an interactive 3 D environment. Visualization of plant species' growth patterns, changes in species and their composition, and other morphological properties of forests are enhanced using machine learning and regression analysis methods as part of a digital model. In modelling, deep learning (DL) replicates expert observations on hundreds or thousands of hectares of trees.

Remote sensing is being used to map the distribution of forest resources, global changes in flora with the seasonal variations, and the 3D structure of forests. Graphic Information System (GIS) based visualizations depict dynamics through animations and 3D geo model visualizations and allow advanced spatial analytics and modelling in geographical phenomena for forest management. Digital forest modelling includes integrating forest inventory data, forest inventory database formation, graphics objects of forest inventory allocations with a digital forest model, and technology for visualizing forest inventory data. It helps forecast changes and visualizes situational phenomena occurring in forests using data and models involving spatial-temporal linkages.

Standard aerial shots capture images that view unseen components to the naked eye, such as the Earth's surface's physical structure and chemical composition. The challenges in remote sensing models include insufficient Remote Sensing (RS), spatial, spectral, and temporal resolution to detect degradation accurately. High costs of RS, the gap between operational and scientific uses, and lack of information sharing are some of the challenges of RS for forest management. The list of topics of interest include but are not limited to the following:

- Advancement of forest surveillance through Geographical Information Systems
- State of the art and perspectives of modelling and visualization framework for Forest type mapping and assessment of distribution
- Futuristic Satellite data analysis for stock maps and forest inventory analysis
- Big data-enabled GIS framework for forest management information
- AI-based Space Remote Sensing For Forest Ecosystem Assessment
- Enhanced visualization through deep learning for forest management solutions
- Novel approaches of multi-temporal satellite data using digital image analysis for forest management
- Advance representation of discrete objects and continuous fields in virtual environments through VR framework
- Database framework for regional and plot-based forest allotment data for model representation and visualization
- Development of scalable models for area-based metrics from Light Detection and Ranging (lidar) devices and photographic structure-for-motion (SFM)

Deadline for Manuscript Submission—June 7, 2022

Submit your Manuscript to <http://asprs-pers.edmgr.com>

Guest Editors

Dr. Gai-Ge Wang, gai-gewang@outlook.com and wgg@ouc.edu.cn, *Department of Computer Science and Technology, Ocean University of China, China*

Dr. Xiao-Zhi Gao, xiao.z.gao@gmail.com and xiao-zhi.gao@uef.fi, *Machine Vision and Pattern Recognition Laboratory, School of Engineering Science, Lappeenranta University of Technology, Finland.*

Dr. Yan Pei, peiyan@u-aizu.ac.jp, *Computer Science Division, The University of Aizu, Japan.*

JOURNAL STAFF

Editor-In-Chief

Alper Yilmaz, Ph.D., PERSeditor@asprs.org

Associate Editors

Rongjun Qin, Ph.D., qin.324@osu.edu

Michael Yang, Ph.D., michael.yang@utwente.nl

Petra Helmholz, Ph.D., Petra.Helmholz@curtin.edu.au

Bo Wu, Ph.D., bo.wu@polyu.edu.hk

Clement Mallet, Ph.D., clemallet@gmail.com

Prasad Thenkabil, Ph.D., pthenkabil@usgs.gov

Ruisheng Wang, Ph.D., ruiswang@ucalgary.ca

Desheng Liu, Ph.D., liu.738@osu.edu

Valérie Gouet-Brunet, Ph.D., valerie.gouet@ign.fr

Dorota Iwaszczuk, Ph.D., dorota.iwaszczuk@tum.de

Qunming Wang, Ph.D., wqm11111@126.com

Filiz Sunar, Ph.D., fsunar@itu.edu.tr

Norbert Pfeifer, np@ipf.tuwien.ac.at

Jan Dirk Wegner, jan.wegner@geod.baug.ethz.ch

Hongyan Zhang, zhanghongyan@whu.edu.cn

Dongdong Wang, Ph.D., ddwang@umd.edu

Zhenfeng Shao, Ph.D., shaozhenfeng@whu.edu.cn

Ribana Roscher, Ph.D., ribana.roscher@uni-bonn.de

Sidike Paheding, Ph.D., spahedin@mtu.edu

Contributing Editors

Highlight Editor

Jie Shan, Ph.D., jshan@ecn.purdue.edu

Feature Articles

Michael Joos, CP, GISP, featureeditor@asprs.org

Grids & Datums Column

Clifford J. Mugnier, C.P., C.M.S., cjmce@lsu.edu

Book Reviews

Sagar Deshpande, Ph.D., bookreview@asprs.org

Mapping Matters Column

Qassim Abdullah, Ph.D., Mapping_Matters@asprs.org

Sector Insight

Lucia Lovison-Golob, Ph.D., lucia.lovison@sat-drones.com

Bob Ryerson, Ph.D., FASPRS, bryerson@kimgeomatics.com

GIS Tips & Tricks

Alvan Karlin, Ph.D., CMS-L, GISP akarlin@Dewberry.com

ASPRS Staff

Assistant Director — Publications

Rae Kelley, rkelley@asprs.org

Electronic Publications Manager/Graphic Artist

Matthew Austin, maustin@asprs.org

Advertising Sales Representative

Bill Spilman, bill@innovativemediasolutions.com

NEW ASPRS MEMBERS

ASPRS would like to welcome the following new members!

Sara Akbarnejad Nesheli

Syeda Saleha Fatim Ali

Amanda Anderson

Tania Septi Anggraini

Braxton Lee Anzalone

Bahaa Awad

Andrew Logan Beckwith

Jhony Armando Benavides-Bolanos

Megan Blaskovich

Will Bordash

Pouyan Boreshnavard

Hannah Bowman

Carly Lynn Bradshaw

Robert Cahalan

Shelby Elaine Campbell

Zachary Canter

Ahmed Elamin

Abigail Faxon

Haidar Fazeli

Connor B. Firat

Reed P. Gallagher

Tewodros Gebre

Anish Giri

Jeff R. Green

Joshua Elliott Halsey

Yuci Han

Jeff Hand, PhD

Akula Harika

Brittany Herzberg

Xinhao Hu

Karin Ingwersen

Yufang Jin

Nicholas Johnson

Sean Michael Jones

James Arthur Kenney

Nicholas Kunz

Matthew Laird

Chen Liang

Yuan Qing Lie

Chintan Bimal Maniyar

Nancy Marek, PhD

Anjana K. Menon

Kavach Mishra

Matthew Mollica

Caleb Ohionije Ogbeta

John Agbo Ogbodo

Nicholas Gregory Orban

Maria Park

Jonathan Roeder

Sreenidhi S

Rajneesh Sharma

Kim Solomon

William Raymond Stuart

Aylin Tuzcu Kokal

Shilpi Verma

Robert Pat Wallace, PE

Caiwang Zheng

FOR MORE INFORMATION ON ASPRS MEMBERSHIP, VISIT

[HTTP://WWW.ASPRS.ORG/JOIN-NOW](http://www.asprs.org/join-now)

Who at ASPRS Do I Contact for help with...

Membership/PE&RS Subscription

office@asprs.org

Advertising/Exhibit Sales

Bill Spilman — bill@innovativemediasolutions.com

PE&RS Editor-in-Chief

Alper Yilmaz — PERSeditor@asprs.org

Calendar — calendar@asprs.org

ASPRS Bookstore — office@asprs.org

ASPRS Foundation — foundation@asprs.org

425 Barlow Place, Suite 210, Bethesda, MD 20814

301-493-0290, 225-408-4422 (fax), www.asprs.org

GEOBYTES

<https://www.asprs.org/geobytes.html>

Deep Fake geography? A humanistic GIS Reflection upon Geospatial Artificial Intelligence

Presenter: Dr. Bo Zhao

When: May 27, 2022, 12:00 PM – 1:00 PM EDT

The ongoing development of Geospatial Artificial Intelligence (GeoAI) has raised deep concerns about the emergence of deep fake geography and its potentials in transforming the human perception of the geographic world (Zhao et al 2021). This seminar presents a humanistic GIS reflection upon GeoAI (Zhao 2022) and its social implications using an empirical study that dissected the algorithmic mechanism of falsifying satellite images with non-existent landscape features. To demonstrate our pioneering attempt at deep fake detection, a robust approach is then proposed and evaluated. Our proactive study warns of the emergence and proliferation of deep fakes in geography just as “lies” in maps. We suggest timely detections of deep fakes in geospatial data and proper coping strategies when necessary. More importantly, it is encouraged to cultivate critical geospatial data literacy and thus to understand the multi-faceted impacts of deep fake geography on individuals and human society.

Bo Zhao is an Associate Professor in the Department of Geography at the University of Washington, Seattle. His recent research interests include GIScience, geographical misinformation, and social implications of emerging GIS technologies, especially in the context of the United States or China.

GeoBytes are online seminars presented by ASPRS and sponsored by the ASPRS GIS Division, in cooperation with CaGIS.

Attention those seeking ASPRS Certification: ASPRS Online Seminars are a great way to gain Professional Development Hours!

Registration Emails for upcoming seminars are sent to all members with the registration link. Just click on the link in the email to get to the online registration for each seminar. After the live seminars have aired, a videotape of the seminar will be posted.

Allen Coral Atlas: A New Technology for Coral Reef Conservation

Presenter: Brianna Bambic

When: September 23, 2022, 12:00 PM – 1:00 PM EDT

Coral reef managers and decision makers at multiple scales need information, in near real time, to react to the increasing threats facing reefs. However, more than three quarters of the world’s coral reefs have never been mapped and lack monitoring. To address this knowledge gap and to support, inform, and inspire critical actions to manage and protect coral reefs, the Allen Coral Atlas combines high resolution satellite imagery, machine learning, and field data to produce globally consistent benthic and geomorphic maps and monitoring systems of the world’s coral reefs. The initiative’s goal is to help stakeholders ranging from local communities to regional and national governments reach their conservation targets and improve their coastal resilience. The multi-disciplinary partnership is led by Arizona State University, in collaboration with Planet, University of Queensland, and the Coral Reef Alliance.

Baseline maps have multiple uses, including: sustainable coastal development, site selection of marine protected areas, planning of restoration activities, and reef fisheries management. In this presentation, we will demonstrate how the Allen Coral Atlas supports data-driven management, conservation, and restoration of coral reefs at local, national, regional, and global scales. We have developed online courses to facilitate increased use and impact of the Atlas, and are collaborating with networks of individuals and institutions who can be alerted when changes are detected (e.g., large-scale bleaching or sedimentation events).

Brianna Bambic leads the Allen Coral Atlas Field Engagement team at the National Geographic Society and Arizona State University. With a coral reef biology and resource management background, she was an Independent Researcher for 7 years that culminated in a virtual reality experience of Half Moon Caye National Monument, Belize with a National Geographic Explorer Grant, helping communicate science to the public. Brianna received her MS in natural resource management from the University of Akureyri, Iceland in 2019. Her expertise includes coastal and marine management, global science communication, and developing capacity around remote sensing and mapping. With countless hours underwater and >700 logged dives, she loves spending time exploring the ocean.

WHO'S WHO IN ASPRS

Founded in 1934, the American Society for Photogrammetry and Remote Sensing (ASPRS) is a scientific association serving thousands of professional members around the world. Our mission is to advance knowledge and improve understanding of mapping sciences to promote the responsible applications of photogrammetry, remote sensing, geographic information systems (GIS) and supporting technologies.

BOARD OF DIRECTORS

BOARD OFFICERS

President

Christopher Parrish, Ph.D
Oregon State University

President-Elect

Lorraine B. Amenda, PLS, CP
Towill, Inc.

Vice President

Bandana Kar
Oak Ridge National Lab

Past President

Jason M. Stoker, Ph.D,
U.S. Geological Survey

Treasurer

Stewart Walker, Ph.D.
photogrammetry4u

Secretary

Harold Rempel
ESP Associates, Inc.

COUNCIL OFFICERS

ASPRS has six councils. To learn more, visit <https://www.asprs.org/Councils.html>.

Sustaining Members Council

Chair: Ryan Bowe
Deputy Chair: Melissa Martin

Technical Division Directors Council

Chair: Bill Swope
Deputy Chair: Hope Morgan

Standing Committee Chairs Council

Chair: David Stolarz
Deputy Chair: TBA

Early-Career Professionals Council

Chair: Madeline Stewart
Deputy Chair: Kyle Knapp

Region Officers Council

Chair: Demetrio Zourarakis
Deputy Chair: Jason Krueger

Student Advisory Council

Chair: Lauren McKinney-Wise
Deputy Chair: Oscar Duran

TECHNICAL DIVISION OFFICERS

ASPRS has seven professional divisions. To learn more, visit <https://www.asprs.org/Divisions.html>.

Geographic Information Systems Division

Director: Denise Theunissen
Assistant Director: Jin Lee

Lidar Division

Director: Ajit Sampath
Assistant Director: Mat Bethel

Photogrammetric Applications Division

Director: Ben Wilkinson
Assistant Director: Hank Theiss

Primary Data Acquisition Division

Director: Greg Stensaas
Assistant Director: Srinu Dharmapuri

Professional Practice Division

Director: Bill Swope
Assistant Director: Hope Morgan

Remote Sensing Applications Division

Director: Amr Abd-Ehrahman
Assistant Director: Tao Liu

Unmanned Autonomous Systems (UAS)

Director: Jacob Lopez
Assistant Director: Bahram Salehi

REGION PRESIDENTS

ASPRS has 13 regions to serve the United States. To learn more, visit <https://www.asprs.org/regions.html>.

Alaska Region

Cascadia Region

Robert Hariston-Porter

Eastern Great Lakes Region

Michael Joos, CP, GISP

Florida Region

Xan Fredericks

Heartland Region

Whit Lynn

Intermountain Region

Robert T. Pack

Mid-South Region

David Hughes

Northeast Region

North Atlantic Region

Pacific Southwest Region

John Erickson, PLS, CP

Potomac Region

Dave Lasko

Rocky Mountain Region

Western Great Lakes Region

Adam Smith

Digital Elevation Model Technologies and Applications The DEM Users Manual, 3rd Edition

Edited by David F. Maune, PhD, CP
and Amar Nayegandhi, CP, CMS

To order, visit
<https://www.asprs.org/dem>

The 3rd edition of the DEM Users Manual includes 15 chapters and three appendices. References in the eBook version are hyperlinked. Chapter and appendix titles include:

1. Introduction to DEMs
*David F. Maune, Hans Karl Heidemann,
Stephen M. Kopp, and Clayton A. Crawford*
 2. Vertical Datums
Dru Smith
 3. Standards, Guidelines & Specifications
David F. Maune
 4. The National Elevation Dataset (NED)
*Dean B. Gesch, Gayla A. Evans,
Michael J. Oimoen, and Samantha T. Arundel*
 5. The 3D Elevation Program (3DEP)
*Jason M. Stoker, Vicki Lukas, Allyson L. Jason,
Diane F. Eldridge, and Larry J. Sugarbaker*
 6. Photogrammetry
J. Chris McGlone and Scott Arko
 7. IfSAR
Scott Hensley and Lorraine Tighe
 8. Airborne Topographic Lidar
Amar Nayegandhi and Joshua Nimetz
 9. Lidar Data Processing
Joshua M. Novac
 10. Airborne Lidar Bathymetry
Jennifer Wozencraft and Amar Nayegandhi
 11. Sonar
Guy T. Noll and Douglas Lockhart
 12. Enabling Technologies
*Bruno M. Scherzinger, Joseph J. Hutton,
and Mohamed M.R. Mostafa*
 13. DEM User Applications
David F. Maune
 14. DEM User Requirements & Benefits
David F. Maune
 15. Quality Assessment of Elevation Data
Jennifer Novac
- Appendix A. Acronyms
Appendix B. Definitions
Appendix C. Sample Datasets

This book is your guide to 3D elevation technologies, products and applications. It will guide you through the inception and implementation of the U.S. Geological Survey's (USGS) 3D Elevation Program (3DEP) to provide not just bare earth DEMs, but a full suite of 3D elevation products using Quality Levels (QLs) that are standardized and consistent across the U.S. and territories. The 3DEP is based on the National Enhanced Elevation Assessment (NEEA) which evaluated 602 different mission-critical requirements for and benefits from enhanced elevation data of various QLs for 34 Federal agencies, all 50 states (with local and Tribal input), and 13 non-governmental organizations.

The NEEA documented the highest Return on Investment from QL2 lidar for the conterminous states, Hawaii and U.S. territories, and QL5 IfSAR for Alaska.

Chapters 3, 5, 8, 9, 13, 14, and 15 are "must-read" chapters for users and providers of topographic lidar data. Chapter 8 addresses linear mode, single photon and Geiger mode lidar technologies, and Chapter 10 addresses the latest in topobathymetric lidar. The remaining chapters are either relevant to all DEM technologies or address alternative technologies including photogrammetry, IfSAR, and sonar.

As demonstrated by the figures selected for the front cover of this manual, readers will recognize the editors' vision for the future – a 3D Nation that seamlessly merges topographic and bathymetric data from the tops of the mountains, beneath rivers and lakes, to the depths of the sea.

Co-Editors

David F. Maune, PhD, CP and
Amar Nayegandhi, CP, CMS

PRICING

Student (must submit copy of Student ID)	\$50 +S&H
ASPRS Member	\$80 +S&H
Non-member	\$100 +S&H
E-Book (only available in the Amazon Kindle store)	\$85

SUSTAINING MEMBERS

ACI USA Inc.

Weston, Florida
<https://acicorporation.com/>
Member Since: 2/2018

Aerial Services, Inc.

Cedar Falls, Iowa
www.AerialServicesInc.com
Member Since: 5/2001

Airworks Solutions Inc.

Boston, Massachusetts
Member Since: 3/2022

Applanix

Richmond Hill, Ontario, Canada
<http://www.applanix.com>
Member Since: 7/1997

Ayres Associates

Madison, Wisconsin
www.AyresAssociates.com
Member Since: 1/1953

CT Consultants

Mentor, Ohio
Member Since: 3/2022

Dewberry

Fairfax, Virginia
www.dewberry.com
Member Since: 1/1985

Esri

Redlands, California
www.esri.com
Member Since: 1/1987

GeoCue Group

Madison, Alabama
<http://www.geocue.com>
Member Since: 10/2003

Geographic Imperatives LLC

Centennial, Colorado
Member Since: 12/2020

GeoWing Mapping, Inc.

Richmond, California
www.geowingmapping.com
Member Since: 12/2016

Half Associates, Inc.

Richardson, Texas
www.halff.com
Member Since: 8/2021

Keystone Aerial Surveys, Inc.

Philadelphia, Pennsylvania
www.kasurveys.com
Member Since: 1/1985

Kucera International

Willoughby, Ohio
www.kucerainternational.com
Member Since: 1/1992

L3Harris Technologies

Broomfield, Colorado
www.l3harris.com
Member Since: 6/2008

Merrick & Company

Greenwood Village, Colorado
www.merrick.com/gis
Member Since: 4/1995

NV5 Geospatial

Sheboygan Falls, Wisconsin
www.quantumspatial.com
Member Since: 1/1974

Pickett and Associates, Inc.

Bartow, Florida
www.pickettusa.com
Member Since: 4/2007

Riegl USA, Inc.

Orlando, Florida
www.rieglusa.com
Member Since: 11/2004

Robinson Aerial Surveys, Inc.(RAS)

Hackettstown, New Jersey
www.robinsonaerial.com
Member Since: 1/1954

Sanborn Map Company

Colorado Springs, Colorado
www.sanborn.com
Member Since: 10/1984

Scorpius Imagery Inc.

Newark, Delaware
aerial@scorpiusimagery.com
Member Since: 6/2021

Surdex Corporation

Chesterfield, Missouri
www.surdex.com
Member Since: 12/2011

Surveying And Mapping, LLC (SAM)

Austin, Texas
www.sam.biz
Member Since: 12/2005

T3 Global Strategies, Inc.

Bridgeville, Pennsylvania
<https://t3gs.com/>
Member Since: 6/2020

Terra Remote Sensing (USA) Inc.

Bellevue, Washington
www.terraremot.com
Member Since: 11/2016

Towill, Inc.

San Francisco, California
www.towill.com
Member Since: 1/1952

Woolpert LLP

Dayton, Ohio
www.woolpert.com
Member Since: 1/1985

SUSTAINING MEMBER BENEFITS

Membership

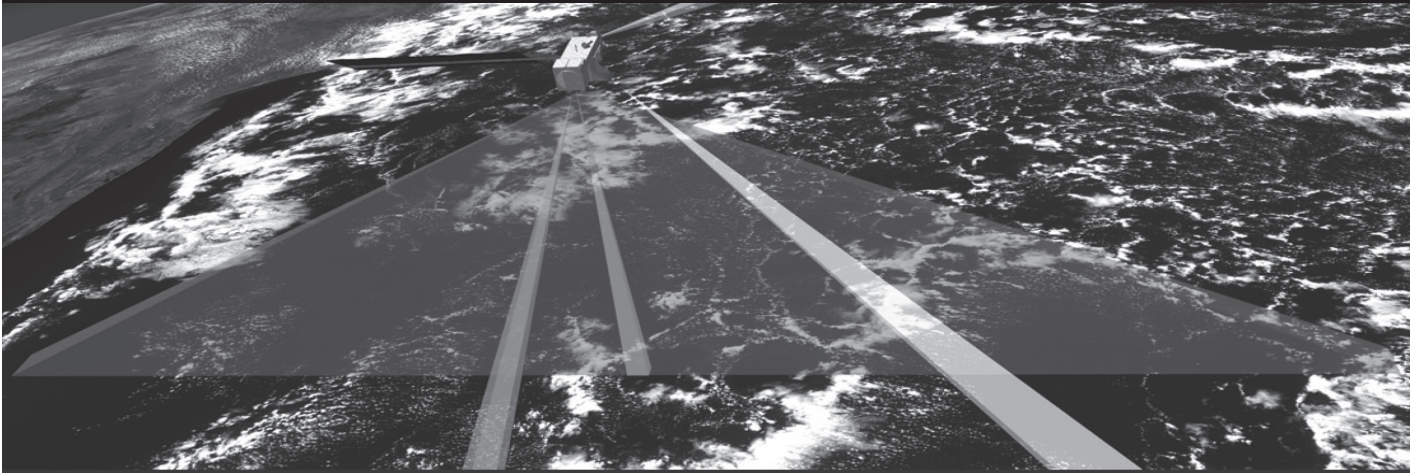
- ✓ Provides a means for dissemination of new information
- ✓ Encourages an exchange of ideas and communication
- ✓ Offers prime exposure for companies

Benefits of an ASPRS Membership

- Complimentary and discounted Employee Membership*
- E-mail blast to full ASPRS membership*
- Professional Certification Application fee discount for any employee
- Member price for ASPRS publications
- Discount on group registration to ASPRS virtual conferences
- Sustaining Member company listing in ASPRS directory/website
- Hot link to company website from Sustaining Member company listing page on ASPRS website
- Press Release Priority Listing in PE&RS Industry News
- Priority publishing of Highlight Articles in PE&RS plus, 20% discount off cover fee
- Discount on PE&RS advertising
- Exhibit discounts at ASPRS sponsored conferences (exception ASPRS/ILMF)
- Free training webinar registrations per year*
- Discount on additional training webinar registrations for employees
- Discount for each new SMC member brought on board (Discount for first year only)

*quantity depends on membership level

The 4th Edition of the *Manual of Remote Sensing*!



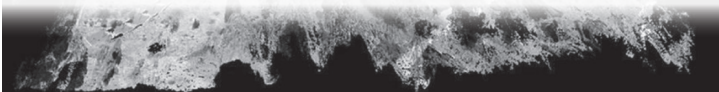
MANUAL OF REMOTE SENSING

Fourth Edition



The *Manual of Remote Sensing, 4th Ed.* (MRS-4) is an “enhanced” electronic publication available online from ASPRS. This edition expands its scope from previous editions, focusing on new and updated material since the turn of the 21st Century. Stanley Morain (Editor-in-Chief), and co-editors Michael Renslow and Amelia Budge have compiled material provided by numerous contributors who are experts in various aspects of remote sensing technologies, data preservation practices, data access mechanisms, data processing and modeling techniques, societal benefits, and legal aspects such as space policies and space law. These topics are organized into nine chapters. MRS4 is unique from previous editions in that it is a “living” document that can be updated easily in years to come as new technologies and practices evolve. It also is designed to include animated illustrations and videos to further enhance the reader’s experience.

MRS-4 is available to ASPRS Members as a member benefit or can be purchased by non-members. To access MRS-4, visit <https://my.asprs.org/mrs4>.



edited by: Stanley A. Morain,
Michael S. Renslow and Amelia M. Budge

Smartphone Digital Photography for Fractional Vegetation Cover Estimation

Gaofei Yin, Yonghua Qu, Aleixandre Verger, Jing Li, Kun Jia, Qiaoyun Xie, and Guoxiang Liu

Abstract

Accurate ground measurements of fractional vegetation cover (FVC) are key for characterizing ecosystem functions and evaluating remote sensing products. The increasing performance of cameras equipped in smartphones opens new opportunities for extensive FVC measurement through citizen science initiatives. However, the wide field of view (FOV) of smartphone cameras constitutes a key source of uncertainty in the estimation of vegetation parameters, which has been largely ignored. We designed a practical method to characterize the FOV of smartphones and improve the FVC estimation. The method was assessed in a mountainous forest based on the comparison with *in situ* fisheye photographs. After the FOV correction, the agreement of smartphone and fisheye FVC estimates highly improved: root-mean-square error (RMSE) of 0.103 compared to 0.242 of the original smartphone FVC estimates without considering the FOV effect, mean difference of 0.074 versus 0.213, and coefficient of determination R^2 of 0.719 versus 0.353. Smartphone cameras outperform traditional fisheye cameras: the overexposure and low vertical resolution of fisheye photographs introduced uncertainties in FVC estimation while the insensitivity to exposure and high spatial resolution of smartphone cameras make photograph acquisition and analysis more automatic and accurate. The smartphone FVC estimates highly agree with the GF-1 satellite product: RMSE = 0.066, bias = 0.007, and R^2 = 0.745. This study opens new perspectives for the validation of satellite products.

Gaofei Yin and Guoxiang Liu are with the Faculty of Geosciences and Environmental Engineering, Southwest Jiaotong University, Chengdu 610031, China (yingf@swjtu.edu.cn).

Gaofei Yin and Aleixandre Verger are with CREAM, 08193 Bellaterra (Cerdanyola del Vallès), Catalonia, Spain.

Gaofei Yin and Aleixandre Verger are with CSIC, Global Ecology Unit, CREAM-CSIC-UAB, 08193 Bellaterra (Cerdanyola del Vallès), Catalonia, Spain.

Yonghua Qu and Kun Jia are with the State Key Laboratory of Remote Sensing Science, Beijing Key Laboratory for Remote Sensing of Environment and Digital Cities, Institute of Remote Sensing Science and Engineering, Faculty of Geography Science, Beijing Normal University, Beijing 100875, China.

Aleixandre Verger is with Desertification Research Centre CIDE-CSIC, 46113 Montcada, València, Spain.

Jing Li is with the State Key Laboratory of Remote Sensing Science, Jointly Sponsored by Aerospace Information Research Institute, Chinese Academy of Sciences and Beijing Normal University, Beijing 100101, China.

Jing Li is with the University of Chinese Academy of Sciences, Beijing 100049, China.

Qiaoyun Xie is with the University of Technology Sydney, Faculty of Science, Sydney NSW 2007, Australia.

Contributed by Desheng Liu, June 30, 2021 (sent for review October 12, 2021; reviewed by Yanjun Su, Barry N Haack, Tianqi Zhang).

Introduction

Fractional vegetation cover (FVC), defined as the fraction of ground surface covered by green vegetation in the nadir direction, plays a key role in the partition between soil and vegetation contributions in the energy and water cycles between surface and atmosphere (Baret *et al.* 2013; Mu *et al.* 2018). FVC is a key controlling factor in many terrestrial processes, including photosynthesis, respiration, and evapotranspiration, and it has been extensively used to monitor vegetation dynamics and ecosystem change (Arnell 2015; Bonan and Doney 2018).

Currently, FVC can be long term monitored at the local-to-global scale through remote sensing technology (Jiapaer *et al.* 2011; Mu *et al.* 2018; Okin *et al.* 2013). Several FVC satellite products are already available including Copernicus Global Land Service (Baret *et al.* 2013; Verger *et al.* 2014), European Organization for the Exploitation of Meteorological Satellites (EUMETSAT) Satellite Application Facility on Land Surface Analysis (LSA SAF) (García-Haro *et al.* 2018), Global Land Surface Satellite (GLASS) (Jia *et al.* 2019), and GaoFen-1 (GF-1) (Jia *et al.* 2016) products. *In situ* FVC measurements are indispensable for the calibration and validation of these FVC estimation algorithms and products (Laliberte *et al.* 2007; Mu *et al.* 2015; White *et al.* 2000). Optical instruments based on gap fraction measurements are commonly used for *in situ* estimation of FVC which corresponds to the complementary of the gap fraction in the nadir direction. The Li-Cor plant canopy analyser (PCA) and digital hemispherical photography (DHP) are widely used (Demarez *et al.* 2008; Garrigues *et al.* 2008; Leblanc *et al.* 2005; LI-COR 1991; Mougin *et al.* 2014). They both measure the gap fraction under the canopy over the whole upper hemisphere. The gap fraction in the nadir direction should be firstly extracted to properly calculate FVC. For PCA, only the reading of the innermost ring (with view zenith ranging 0° to 7°) is appropriate for FVC estimation (LI-COR 1991). For DHP, there is only one pixel per image in the exact nadir direction. Therefore, a range of 0° – 10° zenith angles around the nadir is typically used to achieve a proper trade-off between the estimation accuracy and spatial representativeness (Mougin *et al.* 2014).

Notwithstanding the popularity of PCA and DHP in *in situ* estimation, they still face several disadvantages. PCA is expensive to purchase and to maintain. DHP significantly reduces the cost but is prominently sensitive to photographic exposure setting (Macfarlane *et al.* 2014; Zhang *et al.* 2005). Automatic exposure significantly distorts gap fraction estimation, so several methods were proposed to determine the optimum exposure (Macfarlane *et al.* 2014; Zhang *et al.* 2005). However, the implementation of these methods is difficult for most common users (Pueschel *et al.* 2012). In addition, the performance of DHP is also limited by the mixed-pixel problem caused by its wide field of view (FOV) (Baret *et al.* 2010; Liu *et al.* 2013; Macfarlane 2011).

An alternative for *in situ* FVC estimation is the digital cover photography (DCP) from consumer-grade digital single lens reflex cameras (Chianucci and Cutini 2013; Chianucci *et al.* 2014). DCP cameras have a narrow FOV, generally ranging from 15° to 30° , and the FOV effects do not need dedicatedly consideration (Chen *et al.* 2016; Mu *et al.* 2015). Further, since the sky luminance is relatively homogenous

Photogrammetric Engineering & Remote Sensing
Vol. 88, No. 5, May 2022, pp. 303–310.
0099-1112/22/303–310

© 2022 American Society for Photogrammetry
and Remote Sensing
doi: 10.14358/PERS.21-00038R2

**PEER-REVIEWED CONTENT
IS ONLY AVAILABLE TO
ASPRS MEMBERS AND SUBSCRIBERS**

**FOR MORE INFORMATION VISIT
MY.ASPRS.ORG**

**PEER-REVIEWED CONTENT
IS ONLY AVAILABLE TO
ASPRS MEMBERS AND SUBSCRIBERS**

**FOR MORE INFORMATION VISIT
MY.ASPRS.ORG**

**PEER-REVIEWED CONTENT
IS ONLY AVAILABLE TO
ASPRS MEMBERS AND SUBSCRIBERS**

**FOR MORE INFORMATION VISIT
MY.ASPRS.ORG**

**PEER-REVIEWED CONTENT
IS ONLY AVAILABLE TO
ASPRS MEMBERS AND SUBSCRIBERS**

**FOR MORE INFORMATION VISIT
MY.ASPRS.ORG**

**PEER-REVIEWED CONTENT
IS ONLY AVAILABLE TO
ASPRS MEMBERS AND SUBSCRIBERS**

**FOR MORE INFORMATION VISIT
MY.ASPRS.ORG**

**PEER-REVIEWED CONTENT
IS ONLY AVAILABLE TO
ASPRS MEMBERS AND SUBSCRIBERS**

**FOR MORE INFORMATION VISIT
MY.ASPRS.ORG**

**PEER-REVIEWED CONTENT
IS ONLY AVAILABLE TO
ASPRS MEMBERS AND SUBSCRIBERS**

**FOR MORE INFORMATION VISIT
MY.ASPRS.ORG**

A Low-Cost and Portable Indoor 3D Mapping Approach Using Biaxial Line Laser Scanners and a One-Dimension Laser Range Finder Integrated with Microelectromechanical Systems

Xuzhe Duan, Qingwu Hu, Pengcheng Zhao, and Shaohua Wang

Abstract

Existing indoor 3D mapping solutions suffer from high cost and poor portability. In this article, a low-cost and portable indoor 3D mapping approach using biaxial line laser scanners and a one-dimension laser range finder integrated with microelectromechanical systems is proposed. A multiple-sensor calibration approach is presented to perform the extrinsic calibration of the integrated 3D mapping system. The 2D point cloud acquired by the horizontal laser scanner and the orientation information obtained by the microelectromechanical systems are used as inputs for a simultaneous localization and mapping framework to estimate the 2D poses. The height information acquired by the laser range finder is then fused to obtain the 3D pose, which is applied to restore the actual position and orientation of the 2D point cloud generated by the tilted laser scanner to reconstruct the 3D point cloud of the indoor environment. The experimental results—three typical indoor scenes—demonstrate that the proposed approach can achieve accuracies of 3 cm and 2°. Therefore, the proposed approach is a low-cost, portable, and accurate solution for indoor 3D mapping.

Introduction

Multiple-sensor-integration mobile mapping technology is a cutting-edge technology that integrates positioning, attitude determination, and measurement (D. Li 2006). Different from traditional measurement, which requires the instrument to be fixed at several predetermined stations, mobile measurement technology realizes measurements in motion and avoids the waste of human and time resources caused by the migration of instruments among multiple stations. It also improves the degree of freedom of the platform and solves the problem of blind spots that can exist with traditional methods. A typical mobile measurement system consists of a laser scanner, an optical camera, a global navigation satellite system (GNSS), and an inertial measurement unit (IMU); the GNSS and IMU are responsible for determining the trajectory of the platform, whereas the laser scanner and the optical camera are applied to sense the surrounding environment (Puente *et al.* 2013; Zhao *et al.* 2018).

Generalized mobile measurement refers to the collection of spatial position and attribute data of roadside features with mobile vehicles as platforms (D. Li 2006; Gong *et al.* 2015). However, with continuous improvements in the quality of life, the spatial information of the indoor environment—which accounts for more than 90% of the time spent by human beings—has begun to receive more and more attention. Accurate indoor 3D spatial information can be applied to many fields, such as indoor navigation for mobile robots, digital reconstruction and conservation of ancient ruins, and emergency escape guidance for sudden indoor disasters. The rapid establishment of accurate indoor

maps has become a prerequisite for building information modeling/management, indoor location-based services, and augmented and virtual reality applications (Dominguez Martin *et al.* 2011; Zlatanova and Isikdag 2015; Chen and Clarke 2020).

Ensuring that the sensor's position can be determined while it is in motion is a precondition for the effective implementation of mobile measurement solutions. However, it is often not possible to obtain valid GNSS satellite signals to evaluate the trajectory of the platform in indoor environments (Li *et al.* 2020). Simultaneous localization and mapping (SLAM) is a popular technology for solving indoor localization problems. It aims to build a model of the surrounding environment and estimate the platform's own motion state by using a specific sensor without prior environmental information (Dissanayake *et al.* 2001). The increasing maturity of SLAM technology provides strong technical support for indoor mobile measurement, which has addressed the problem of how platforms can “localize themselves” in the absence of GNSS signals.

SLAM can be divided into visual SLAM and laser SLAM, depending on the sensor type. The positioning and mapping technology that uses a monocular, stereo, or depth camera as the only exteroceptive sensor is called visual SLAM (Davison *et al.* 2007; Comport *et al.* 2010; Fuentes-Pacheco *et al.* 2015; Forster *et al.* 2017; Mur-Artal and Tardós 2017). It has the characteristics of small size, low power consumption, and rich information acquisition, which can provide rich environment texture information (Di *et al.* 2019). With the continuous optimization of image-matching algorithms, research on visual SLAM has grown stronger (J. Li *et al.* 2017; Li *et al.* 2020; Mao *et al.* 2020; Cao *et al.* 2021). However, since cameras are susceptible to visual-field limitations, bad weather, backlight, and other unsatisfactory conditions, visual SLAM is often very dependent on the working environment, and has low accuracy (Huang *et al.* 2018).

Laser SLAM has gradually become the most popular area of research in the field of SLAM. Benefiting from the characteristics of a laser scanner, laser SLAM has the advantages of high measurement accuracy, high directionality, and low computational effort (Debeunne and Vivet 2020; Wei *et al.* 2020). According to the mathematical optimization framework adopted, laser SLAM can be further divided into filter-based and graph optimization-based. FastSLAM is a typical filter-based laser SLAM scheme (Montemerlo *et al.* 2002). In this algorithm, the platform's poses are estimated by a particle filter, and each particle is propagated by the kinematics model. For the propagated particles, the weight is calculated by the observation model and the map is constructed according to the estimated poses. On this basis, a Gmapping scheme that uses a Rao-Blackwellized particle filter to synchronize the position and orientation of the platform has been proposed (Grisetti *et al.* 2007). Gmapping solves FastSLAM's problems of high memory consumption

Xuzhe Duan, Qingwu Hu, Pengcheng Zhao, and Shaohua Wang are with the School of Remote Sensing and Information Engineering, Wuhan University, Wuhan 430079, China (shwang@whu.edu.cn).

Contributed by Rongjun Qin, June 30, 2021 (sent for review August 5, 2021; reviewed by Kaleel M Al-Durgham, Ruofei Zhong).

Photogrammetric Engineering & Remote Sensing
Vol. 88, No. 5, May 2022, pp. 311–321.

0099-1112/22/311–321

© 2022 American Society for Photogrammetry
and Remote Sensing

doi: 10.14358/PERS.21-00037R2

**PEER-REVIEWED CONTENT
IS ONLY AVAILABLE TO
ASPRS MEMBERS AND SUBSCRIBERS**

**FOR MORE INFORMATION VISIT
MY.ASPRS.ORG**

**PEER-REVIEWED CONTENT
IS ONLY AVAILABLE TO
ASPRS MEMBERS AND SUBSCRIBERS**

**FOR MORE INFORMATION VISIT
MY.ASPRS.ORG**

**PEER-REVIEWED CONTENT
IS ONLY AVAILABLE TO
ASPRS MEMBERS AND SUBSCRIBERS**

**FOR MORE INFORMATION VISIT
MY.ASPRS.ORG**

**PEER-REVIEWED CONTENT
IS ONLY AVAILABLE TO
ASPRS MEMBERS AND SUBSCRIBERS**

**FOR MORE INFORMATION VISIT
MY.ASPRS.ORG**

**PEER-REVIEWED CONTENT
IS ONLY AVAILABLE TO
ASPRS MEMBERS AND SUBSCRIBERS**

**FOR MORE INFORMATION VISIT
MY.ASPRS.ORG**

**PEER-REVIEWED CONTENT
IS ONLY AVAILABLE TO
ASPRS MEMBERS AND SUBSCRIBERS**

**FOR MORE INFORMATION VISIT
MY.ASPRS.ORG**

**PEER-REVIEWED CONTENT
IS ONLY AVAILABLE TO
ASPRS MEMBERS AND SUBSCRIBERS**

**FOR MORE INFORMATION VISIT
MY.ASPRS.ORG**

**PEER-REVIEWED CONTENT
IS ONLY AVAILABLE TO
ASPRS MEMBERS AND SUBSCRIBERS**

**FOR MORE INFORMATION VISIT
MY.ASPRS.ORG**

**PEER-REVIEWED CONTENT
IS ONLY AVAILABLE TO
ASPRS MEMBERS AND SUBSCRIBERS**

**FOR MORE INFORMATION VISIT
MY.ASPRS.ORG**

**PEER-REVIEWED CONTENT
IS ONLY AVAILABLE TO
ASPRS MEMBERS AND SUBSCRIBERS**

**FOR MORE INFORMATION VISIT
MY.ASPRS.ORG**

IN-PRESS ARTICLES

- Gaofei Yin. Smartphone Digital Photography for Fractional Vegetation Cover Estimation.
- Xuzhe Duan, Qingwu Hu, Pengcheng Zhao, and Shaohua Wang. A low-cost and portable indoor 3D mapping approach using biaxial line laser scanners and a one-dimensional laser rangefinder integrated with MEMS.
- Toshihiro Sakamoto, Daisuke Ogawa, Satoko Hiura, Nobusuke Iwasaki. Alternative procedure to improve the positioning accuracy of orthomosaic images acquired with Agisoft Metashape and DJI P4 Multispectral for crop growth observation
- Guangyun Li, Senzhen Sun, Yangjun Gao, Li Wang. Robust Dynamic Indoor Visible Light Positioning Method Based on CMOS Image Sensor.
- Zhenfeng Shao, Hongping Zhang, Wenfu Wu, Xiao Huang, Jisong Sun, Jinqi Zhao, Yewen Fan. Comparing the sensitivity of pixel-based and sub-watershed-based AHP to weighting criteria for flood hazard estimation.
- Gang Qiao, Hongwei Li. Lake Water Footprint Determination Using Linear Clustering-based Algorithm and Lake Water Changes in the Tibetan Plateau from 2002 to 2020.
- Jason Parent, Chandi Witharana, Michael Bradley. Classifying and georeferencing indoor point clouds with ARCGIS.
- Paul Pope, Brandon Crawford, Anita Lavadie-Bulnes, Emily Schultz-Fellenz, Damien Milazzo, Kurt Solander, Carl Talsma. Towards Automated/Semi-Automated Extraction of Faults from Lidar Data
- Li Tan, Guoming Li, Xin Liu, Aike Kan. Feature-based convolutional neural network for very-high-resolution urban imagery classification
- Ravi Dwivedi, Syed Azeemuddin. Conjunctive use of Landsat-8 OLI and MODIS Data for Delineation of Burned Areas
- Chih-Hung Hsu, Che-Hao Chang, Chih-Tsung Hsu, Shiang-Jen Wu, Po-Hsien Chung. Hydrological Topography Dataset (HTD) - the Dataset for High Resolution 2D Urban Flood Modeling.
- Xiaojun Yang, Feilin Lai. Improving land cover classification over a large coastal city through stacked generalization with filtered training samples.
- Xiaoyue Wang, Hongxin Zhang, Dailiang Peng. Evaluation of urban vegetation phenology using 250 m MODIS vegetation indices.
- Zhijia Xu, Xingzheng Lu, Wenliang Wang, Ershuai Xu, Rongjun Qin, Yiru Niu, Xu Qiao, Feng Yang, Rui Yan. Monocular Video Frame Optimization through Feature-based Parallax Analysis for 3D Pipe Reconstruction.
- Lin Ding, Hanchao Zhang, Deren Li. Monitoring and Analysis of Urban Sprawl based on Road Network Data and High-resolution Remote Sensing Imagery: A Case Study of China's Provincial Capitals.
- Xueyan Li, Heqing Zhang, Zhenxin Wang, Junfeng Song. Transformer for the Building Segmentation of Urban Remote Sensing.

Alternative Procedure to Improve the Positioning Accuracy of Orthomosaic Images Acquired with Agisoft Metashape and DJI P4 Multispectral for Crop Growth Observation

Toshihiro Sakamoto, Daisuke Ogawa, Satoko Hiura, and Nobusuke Iwasaki

Abstract

Vegetation indices (VIs), such as the green chlorophyll index and normalized difference vegetation index, are calculated from visible and near-infrared band images for plant diagnosis in crop breeding and field management. The DJI P4 Multispectral drone combined with the Agisoft Metashape Structure from Motion/Multi View Stereo software is some of the most cost-effective equipment for creating high-resolution orthomosaic VI images. However, the manufacturer's procedure results in remarkable location estimation inaccuracy (average error: 3.27–3.45 cm) and alignment errors between spectral bands (average error: 2.80–2.84 cm). We developed alternative processing procedures to overcome these issues, and we achieved a higher positioning accuracy (average error: 1.32–1.38 cm) and better alignment accuracy between spectral bands (average error: 0.26–0.32 cm). The proposed procedure enables precise VI analysis, especially when using the green chlorophyll index for corn, and may help accelerate the application of remote sensing techniques to agriculture.

Introduction

Remote sensing is a cost-effective tool for monitoring crop growth in vast fields. In the past, agricultural research commonly used multispectral images obtained by spaceborne or airborne remote sensing sensors for field monitoring (Boegh *et al.* 2002; Maas and Rajan 2008; Borgogno-Mondino *et al.* 2018). Recently, the use of drones (unmanned aerial vehicles) has become more popular, especially for field-scale agricultural observations and management (Huang *et al.* 2018; Maes and Steppe 2019; Peter *et al.* 2020). One of the reasons is that drone-based remote sensing provides multispectral images of crop lines with higher spatial and temporal resolution. Another reason is the advent of reasonably priced small drones equipped with dedicated cameras and Structure from Motion/Multi View Stereo (SfM/MVS) software, such as Agisoft Metashape Professional (Agisoft LLC, St. Petersburg, Russia) and Pix4D mapper (Pix4D, Lausanne, Switzerland), which enable beginners in remote sensing to create orthomosaic images. These technological advancements allow phenological observation of seasonal changes in crop growth with higher spatial resolution (Malambo *et al.* 2018; Che *et al.* 2020).

Toshihiro Sakamoto* is with Institute for Agro-Environmental Sciences, NARO, 3-1-3 Kannondai, Tsukuba, Ibaraki, Japan (*corresponding author: sakamt@affrc.go.jp).

Daisuke Ogawa is with Institute of Crop Science, NARO, 2-1-2 Kannondai, Tsukuba, Ibaraki, Japan.

Satoko Hiura is with Tohoku Agricultural Research Center, NARO, 4 Akahira, Shimo-kuriyagawa, Morioka, Iwate, Japan.

Nobusuke Iwasaki is with Institute for Agro-Environmental Sciences, NARO, 3-1-3 Kannondai, Tsukuba, Ibaraki, Japan.

Contributed by Rongjun Qin, September 9, 2021 (sent for review September 17, 2021; reviewed by Xiao Ling, Zhijia Xu).

In the field of breeding, drones are used as a high-throughput phenotyping tool for the monitoring of various phenotypic features, such as vegetation fraction, plant height, and disease symptoms (Reynolds *et al.* 2020). Recently, we developed image analysis methods for evaluating the vegetation fraction and plant architecture of rice using data obtained with a DJI Phantom 4 Pro drone (P4P; DJI, Shenzhen, China), which has an RGB camera equipped with a 1-in. sensor (Ogawa *et al.* 2019, 2021). Until 2019, in reports of high-throughput phenotyping with drone remote sensing technology, RGB images were more commonly used than multispectral images (Vargas *et al.* 2019; Zhang *et al.* 2020; Svensgaard *et al.* 2021; Tang *et al.* 2021). This was because small drones equipped with an RGB camera were cheaper than large drones or sophisticated small drones equipped with a multispectral camera, such as the Bluegrass Fields drone (Parrot, Paris, France) (Sun *et al.* 2019; Qi *et al.* 2021). In October 2019, DJI launched a new small drone, named P4 Multispectral (P4M), designed for agricultural monitoring. It has a six-lens multispectral camera, spectral sunlight sensor, and high-precision global navigation satellite system (GNSS) receiver for automatic navigation flight using real-time kinematic (RTK). On the other hand, the Metashape SfM/MVS software has the largest market share in business and research applications, such as 3D work progress control for civil engineering work and orthomosaic image creation for agricultural environmental monitoring. A Google Scholar search for the key words “Metashape” (or “Photoscan”) and “Pix4D” yielded 11,750 and 5,390 hits, respectively (date of search: 9 August 2021). According to the results of a questionnaire survey conducted by the Forest Agency of Japan among forest owner cooperatives, forestry organizations, and local governments in 2020, 55% of the respondents had used Metashape, whereas only 6.1% had used Pix4D (Blue Innovation Co. Ltd 2020). The advantages of Metashape are that there are numerous blogs that explain how to use it and that it is highly price competitive in terms of its low initial cost and no upgrade fees (up to version 1.99) regardless of its versatility.

Although Metashape and P4M are among the most cost-effective combinations of aerial photography equipment for creating multispectral orthomosaic images, Metashape does not have a dedicated processing mode for P4M data until at least version 1.7.3, build 12473 (64 bit). Instead, the Agisoft Helpdesk web page officially introduces how to process the P4M data by using a general processing flow called a “multi-camera system” (Agisoft Helpdesk Portal 2021) (last updated on 25 May 2021). As a preliminary experiment, we created a multispectral orthomosaic image from P4M-derived aerial images by following the manufacturer's tutorial, and we visually assessed the quality of the tutorial-derived multispectral orthomosaic image by overlaying it onto an orthomosaic image created from P4P-derived aerial RGB color

Photogrammetric Engineering & Remote Sensing
Vol. 88, No. 5, May 2022, pp. 323–332.
0099-1112/22/323–332

© 2022 American Society for Photogrammetry
and Remote Sensing
doi: 10.14358/PERS.21-00064R2

images. In doing so, the following issues were found: (1) The positions of ground control points (GCPs) on orthomosaic images derived from P4M and P4P did not agree with each other. (2) There were obvious misalignment errors between spectral band images in the P4M-derived multispectral orthomosaic images; therefore, when the GCPs were visualized in false color composite (near-infrared [NIR]-red-green) images, the edges of the white squared parts of GCPs were colored with a gradient from blue to red. These misalignment issues would negatively influence data analysis. In the Agisoft user forum (<https://www.agisoft.com/forum/index.php?topic=12894.msg57129#msg57129>), a similar issue has been pointed out with regard to the processing of multispectral images using Metashape. However, no specific solution has been presented. Therefore, it is necessary to improve the methodology to create orthomosaic images from a series of P4M multispectral images using the Metashape software.

In this study, we comprehensively evaluated the absolute location accuracy and band alignment accuracy of multispectral orthomosaic images created based on the tutorial procedure. In addition, we devised alternative processing procedures that combine the other general processing steps of Metashape to improve multispectral orthomosaic image quality. Finally, we demonstrated that the alternative processing procedures provided higher accuracy in terms of geolocation and image alignment between the spectral bands than the manufacturer's tutorial procedure.

Experimental Fields

The experimental fields were located on the campus of the NARO Institute for Agro-Environmental Sciences in Tsukuba, Japan (36°01'29" N, 140°06'37.2" E; Figure 1A and 1B, see next page). The target crops for aerial photography were forage dent corn (*Zea mays* L. cv. New dent 100) and paddy rice (*Oryza sativa* L. cv. Koshihikari). Twelve plots (1.28×1.28 m) were set as regions of interest in nine concrete-framed fields of 8×8 m. The amount of chemical nitrogen fertilizer was varied from 0 to 25 kg N/10 a in the six corn plots and from 0 to 8 kg N/10 a in the six rice plots (Figure 1C). Corn seeds were sowed by hand on 27 May 2021, with a row width of 75 cm and an inter-hill space of 20 cm. Rice seedlings were transplanted by hand on 2 June 2021, with a row width of 30 cm and an inter-hill space of 18 cm.

Twenty ground control points (GCPs) had been painted onto the concrete ground using black and white paint for road signs. Half of the GCPs (numbers 1, 4, 7, 8, 11, 14, 15, 17, 18, and 20) were used for internal camera calibration for SfM/MVS analysis using Metashape. The other half (numbers 2, 3, 5, 6, 9, 10, 12, 13, 16, and 19) were used for location accuracy verification of the multispectral orthomosaic images acquired with the three procedures evaluated.

Materials

The P4M drone was automatically controlled by dedicated flight control software, DJI GS Pro (2.0.16 [10657] (DJI), installed on an iPad mini (Apple Inc., Elk Grove, Calif., USA). The P4M can take five spectral images (blue [450 ± 16 nm], green [560 ± 16 nm], red [650 ± 16 nm], red edge [730 ± 16 nm], NIR [840 ± 26 nm]) and one RGB color image simultaneously. Automatic flight photography using the P4M was conducted at two flight heights (20 and 30 m) around 8:30 A.M. on 6 July 2021 and around 13:00 P.M. on 13 July 2021. We investigated four aerial photo sets assembled from photographs acquired at two different observation dates and two different flight heights. We acquired 204 sets of multispectral images on 6 July and 185 on 13 July at a height of 20 m (resolution: 1.1 cm/pixel) and 114 on each of 6 July and 13 July at a height of 30 m (resolution: 1.6 cm/pixel). The parameters of automatic flight photography using DJI GS Pro were set as listed in Table 1.

The P4M was automatically operated in RTK positioning mode coupled with the use of high-precision GNSS correction information distribution service of the Virtual Reference Station (JENObA Co., Ltd, Tokyo, Japan). The images of the MicaSense Calibration Reflectance Panel (MicaSense Inc., Seattle, Wash., USA) (Mamaghani and Salvaggio 2019), which were used for reflectance calibration, were taken before and after each flight with manual operation. The range of

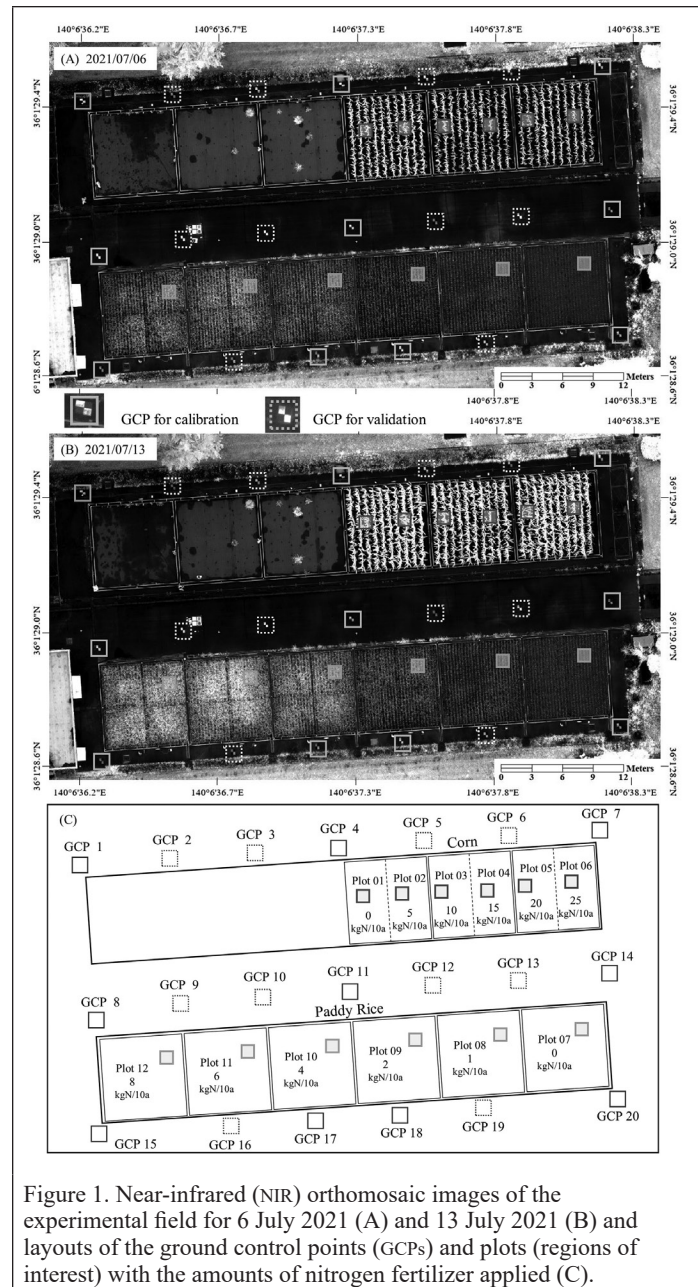


Figure 1. Near-infrared (NIR) orthomosaic images of the experimental field for 6 July 2021 (A) and 13 July 2021 (B) and layouts of the ground control points (GCPs) and plots (regions of interest) with the amounts of nitrogen fertilizer applied (C).

Table 1. Flight parameters used in the experiments.

Parameter	Description
Shooting angle	Parallel to main path
Capture mode	Capture at time interval
Flight course mode	Inside mode
Flight speed	1.3 m/s
Front overlap ratio	80%
Side overlap ratio	80%
Course angle	184°
Gimbal pitch angle	-90°

the automatic flight route at 20-m height was partially narrower than that at 30 m to prevent collision with trees. Accordingly, GCP1 and GCP2 are not shown in aerial images at 20-m height.

Agisoft Metashape Professional SfM/MVS software was used to create multispectral orthomosaic images from the aerial images. The latest software version (version 1.7.3, build 12473 [64 bit], 5 July 2021) was

installed. A general-purpose remote sensing software, ENVI 5.6 (API version 3.6; Harris Geospatial, Broomfield, Colo., USA), was used for postprocessing, including format conversion and image subset and layer stacking of spectral band images.

Methods

Processing Procedures for Creating Multispectral Orthomosaic Images Using Metashape

We considered the official processing procedure communicated on the Agisoft Helpdesk Portal Web page (Agisoft Helpdesk Portal 2021) to be the most common standard procedure when analyzing P4M data with Agisoft Metashape Professional version 1.7.3, build 12473 (64 bit), and named it “tutorial procedure” (TP). We newly developed two alternative processing procedures—alternative procedure 1 (AP1) and alternative procedure 2 (AP2)—and compared them with TP. The work flows of the procedures evaluated are shown in Figure 2.

The major common aspects of data processing in the three methods are as follows. RTK positioning information of each spectral camera, stored as XMP metadata in the header file of each TIFF file, was used for internal camera calibration, along with precisely surveyed coordinate information of the GCP markers. The unit for the height of the coordinate information of GCP markers was the ellipsoid height in accordance with the RTK positioning information of the multispectral camera.

Universal Transverse Mercator (UTM) (zone: 54 N; datum: WGS84) was used for map projection of the orthomosaic images. The output spatial resolution was set to 1 cm/pixel regardless of flight height. The 16-bit unsigned integer pixel values of the orthomosaic images exported from Metashape were divided by 32,768 for conversion to 32-bit float pixel values of spectral reflectance ranging from 0.0 to 1.0. The output orthomosaic images were cropped to obtain 6000×3400-pixel square regions with a fixed location based on the geographic

information (Figure 1A and 1B). Assuming the use of multispectral orthomosaic images for crop growth monitoring, we assessed the impact of the three procedures on observed values of vegetation indices (VIs), including the green chlorophyll index (CI_{green}) and normalized difference vegetation index (NDVI) (Rouse *et al.* 1974).

Agisoft TP

The main feature of TP is the use of a dedicated processing mode named the “multi-camera system” in Metashape (Figure 2A), in which all spectral band images are imported at once into a working folder named “chunk.” The advantage of the “multi-camera system” mode is that the time-consuming manual work of defining the GCP marker locations needs to be done only for default blue band images, not for the other four spectral bands, resulting in a shorter processing time. A digital surface model (DSM) was made from a high-quality dense cloud that was built as a common data set for all spectral bands. Multispectral orthomosaic images were built in reference to the DSM and were exported as a single TIFF file containing five spectral band images.

AP1

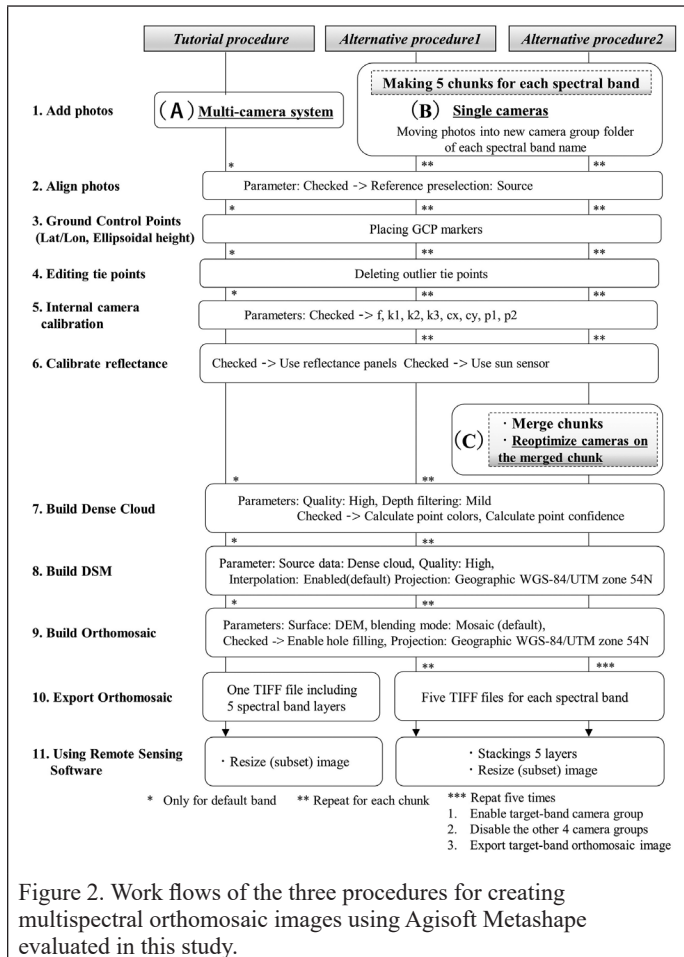
AP1 used a general processing flow named “single camera” in Metashape instead of the “multi-camera system” mode. First, we created five chunks of working folders named after the spectral bands (blue, green, red, red edge, and NIR) in a working project file (Figure 2B). Next, the multispectral band images were imported separately into each chunk with the corresponding spectral band. The following steps were repeated as many times as the number of chunks (spectral bands) created: manual placement of GCP marker locations on each image, internal camera calibration, dense cloud building, DSM, and creation of single-band orthomosaic images. The single-band orthomosaic images were individually exported from each chunk. Therefore, the workload of AP1 was estimated to be approximately five times that of TP. In addition, the five TIFF files were layer stacked into a single file containing multispectral band images using the general-purpose remote sensing software ENVI or IDL5.6.

AP2

AP2 was a further improvement of AP1. AP2 also preliminarily created five chunks in the working project file. Furthermore, AP2 created new subfolders called “camera group folder” within each chunk and named the subfolders according to the corresponding spectral band. The original spectral band images were separately moved into the new subfolders. This was a preliminary step to make it easier to merge the five chunks described later. Internal camera calibration was repeated for every chunk. The major process difference between AP1 and AP2 was that the separately created chunks were merged into one common chunk to integrate tie points and GCP markers for each spectral band in AP2. Then internal camera calibration was reconducted for the newly merged common chunk using the integrated tie points and GCP markers to establish one common camera parameter for all spectral bands (Figure 2C). Only one common dense cloud or DSM layer was created in the merged chunk. Single-band orthomosaic images were repeatedly created as follows. For example, when creating a blue band orthomosaic image, the other subfolders of the camera group folder (green, red, red-edge, and NIR) were preliminarily disabled before building the blue band orthomosaic. These steps were repeated as many times as the number of spectral bands in the merged chunk. The way of stacking the five TIFF files into one file was the same as in AP1.

Accuracy Assessment of Estimated GCP Locations

Coordinate data of the GCPs (latitude, longitude, and ellipsoid height) were measured by postprocessing static (PPS) surveys using GNSS data acquired simultaneously from two paired GNSS receivers. GNSS rover data of each GCP marker were logged by compact GNSS receivers using a NEO-M8P RTK GNSS receiver board (Etehs SIA, Riga, Latvia) for more than 30 minutes. Data of a GNSS continuously operating reference station named “Tsukuba 3” were used as base station data. The station is located 9 km away from the experimental field and is operated by the Geographical Survey Institute of Japan. The PPS surveys were conducted using an open-source program package for GNSS positioning, RTKLIB (version 2.4.3b34) (<http://www.rtklib.com>). The GNSS-derived



GCP coordinate information was converted from latitude and longitude to the UTM coordinate system for comparison with the estimated coordinate information of the corresponding GCPs for verification based on the orthomosaic images. UTM coordinate information of the GCPs was manually read for each spectral band individually using ENVI/IDL 5.6 software.

Accuracy Assessment of Misalignment Between Five Spectral Band Images

The relative alignment error between five spectral band images was evaluated according to the following criteria, without using the ground-truth coordination data measured by the GNSS receiver. For each single GCP, information of five coordinates could be read as the P4M-derived multispectral orthomosaic image comprised of five spectral band images.

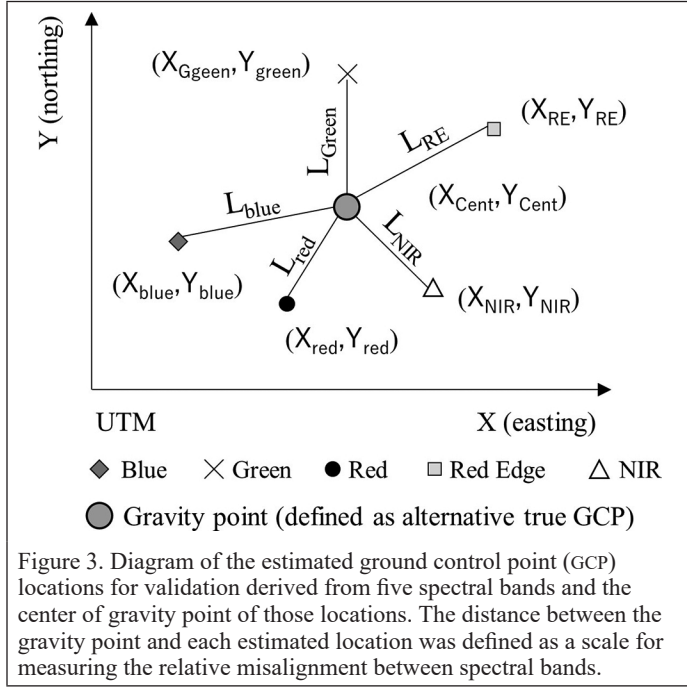


Figure 3. Diagram of the estimated ground control point (GCP) locations for validation derived from five spectral bands and the center of gravity point of those locations. The distance between the gravity point and each estimated location was defined as a scale for measuring the relative misalignment between spectral bands.

As shown in Figure 3, we assumed the center of gravity of the five coordinate points as hypothetical true GCP location rather than the GNSS receiver-derived coordinate location. The coordinate information of the gravity point (X_{grav}, Y_{grav}) was calculated with Equation 1. Next, the five distances (L_{band}) from the gravity point to these five points were calculated with Equation 2. The average value of the five distances was defined as a scale (S_{mis}) to measure the relative misalignment between spectral bands (Equation 3):

$$X_{grav} = \frac{1}{5} \sum_{i=band} X_i, \quad Y_{grav} = \frac{1}{5} \sum_{i=band} Y_i \quad (1)$$

$$L_{band} = \sqrt{(X_{grav} - X_{band})^2 + (Y_{grav} - Y_{band})^2} \quad (2)$$

$$S_{mis} = \frac{1}{5} \sum_{i=band} L_i \quad (3)$$

where band is blue, green, red, red edge, or NIR.

VI_s

We evaluated the effect of quality differences of the multispectral orthomosaic images due to the different processing procedures on observed VI values. CI_{green} and NDVI were calculated using Equations 4 and 5:

$$CI_{green} = \frac{\rho_{NIR}}{\rho_{green}} \quad (4)$$

$$NDVI = \frac{\rho_{NIR} - \rho_{red}}{\rho_{NIR} + \rho_{red}} \quad (5)$$

where ρ_{NIR} , ρ_{green} , and ρ_{red} are spectral reflectance values (0–1.0) in the NIR (840 ± 26 nm), red (650 ± 16 nm), and green (560 ± 16 nm) bands.

CI_{green} is correlated with the canopy chlorophyll content, which is the amount of chlorophyll per unit area (Wu *et al.* 2012; Schlemmer *et al.* 2013; Inoue *et al.* 2016; Clevers *et al.* 2017) or nitrogen concentration in plant leaves (Cai *et al.* 2019). CI_{green} is widely used as a remote sensing-based indicator useful for estimating photosynthetic carbon assimilation in various fields (Peng and Gitelson 2011; Zhang *et al.* 2015). Gitelson *et al.* (2003, 2005) found that CI_{green} is related to canopy photosynthesis of irrigated maize. It can be used as an alternative indicator to the product of light use efficiency (ϵ) and fraction of absorbed photosynthetically active radiation (fPAR) in the light use efficiency model (Peng and Gitelson 2012) described by the following equation (Monteith 1972) to estimate gross primary production (GPP):

$$GPP = \epsilon \times fPAR \times PAR \quad (6)$$

$$GPP \propto CI_{green} \times PAR \quad (7)$$

NDVI remains the most popular multipurpose VI used for crop monitoring of various features, including leaf nitrogen concentration, aboveground biomass, fraction of absorbed photosynthetically active radiation, and damage caused by diseases (Thenkabail *et al.* 1994; Franke and Menz 2007; Sakamoto *et al.* 2012; Shibayama *et al.* 2012). In recent years, with the advent of affordable small drones with multispectral cameras, many researchers who are starting to apply drone-based remote sensing for crop growth monitoring in Japan tend to use NDVI as a de facto standard VI under a national trend in precision agriculture research called “smart agriculture” (Morimoto and Hayashi 2017; Guan *et al.* 2019; Osaki 2019; Inoue 2020).

Comparison of Pixel-Level or Region-Averaged VIs at Fixed Locations Between Multispectral Orthomosaic Images Obtained at 20- and 30-m Flight Height

The effect of misalignment due the processing procedure on the VI was evaluated as follows. Multispectral orthomosaic images with a 1-cm pixel resolution were generated from the data sets acquired on the same day but at different flight heights. A one-by-one comparison of pixel-level VI and region-averaged VI was performed for the 12 plots for each procedure evaluated in anticipation of the creation of gridded vegetation growth maps for designing variable-rate fertilization in precision agriculture (Veroustraete 2015; McKinnon 2016; Saiz-Rubio and Rovira-Más 2020). The square (grid) size for measuring region-averaged VIs was varied at seven levels (2×2, 4×4, 8×8, 16×16, 32×32, 64×64, and 128×128 pixels) to investigate the effect of square size on the observed VI value. If there is no misalignment effect, the observed VI should consistently be approximately the same at the same location regardless of the flight height. The lower the misalignment effect, the closer the data points in a scatter plot are distributed to the one-by-one straight trend line. In other words, the procedure that showed the highest correlation or lowest root mean square error (RMSE) between VI images obtained at different flight heights could be regarded as having the best performance without a misalignment problem.

Results and Discussion

Location Estimation Accuracy of GCPs for Verification

Figure 4 shows the GCP location estimation error for verification based on the GNSS-derived true position. Some of the TP-derived results had errors of more than 6 cm at any combination of flight height and observation date (Figure 4A1–4). When using TP, the number (percentage) of GCPs with errors of less than 1.5 and 3.0 cm were 40 (21.1%) and 97 (51.1%) out of the total (190) GCPs, respectively. Although it was unclear why the TP-derived location error tended to be more spread out in the east–west direction than in the north–south direction, this error trend may be related to the fact that the GCP locations were widely

spread in the east–west direction in the experimental fields. The AP1-derived results had little directional error variation, especially in the east–west direction, and the variability of error was substantially smaller than that of the TP results. AP1 did not produce errors of more than 6 cm (Figure 4B1–4). The number of GCPs with errors less than 1.5 and 3.0 cm were 103 (54.2%) and 173 (91.1%) out of the total (190) GCPs, respectively. The AP2-derived results showed similar overall

trends in error variation as the AP1 results. There was no GCP with an error greater than 6 cm based on the GNSS-derived true locations. When we focused on local trends in error variation, we observed a smaller variability of the errors, especially between spectral bands, than in AP1 (Figure 4C1–4). When using AP2, the number of GCPs with errors of less than 1.5 and 3.0 cm were 125 (65.8%) and 185 (97.6%) out of the total (190) GCPs, respectively. Thus, AP2 produced the smallest error.

Table 2 shows a summary of statistics for errors in the estimated GCP locations. The average values of the GCP location estimation error of TP for all spectral bands were 2.70–3.01 cm at 20-m flight height and 3.78–3.85 cm at 30-m flight height. The GCP location estimation error of TP was about twice that of AP2 (average error: 1.35–1.40 cm at 20 m, 1.30–1.36 cm at 30 m). Only for the red band, which had the best location estimation accuracy, was the estimation error comparable between AP1 and AP2, although we used mainly the default blue-band images for placing GCP markers manually and internal camera calibration. Unlike in the case of TP, when AP1 and AP2 were used, there were no extreme differences in location estimation errors depending on specific spectral cameras. The estimation location accuracy of AP2 was comparable to that of a drone designed for surveying work, that is, the DJI Phantom 4 RTK (Taddia *et al.* 2020).

Table 3 summarizes paired t-test results of GCP location estimation error comparison between TP and AP1 and between AP1 and AP2. The location estimation error of AP1 was significantly smaller than of TP at the 1% level in two-tailed tests. The average location estimation error of AP2 was smaller than that of AP1; except for a few cases, no significant difference was found between these procedures for data obtained at 20-m flight height. However, at the 1% level, the location estimation error of AP2 was significantly smaller than that of AP1 only for data obtained at 30-m flight height. These data clearly indicated that the absolute location estimation accuracy of TP was inferior to that of AP1 and AP2. Considering that the positioning accuracy of the PPS survey using GNSS data used to measure the coordinates of the GCPs is approximately 1 cm, the estimation accuracy of AP1 and AP2 can be considered almost similar.

The most interesting finding in this study was that estimation accuracy typically depended on the spectral cameras position when using TP; the spectral cameras showing better location estimation results, in order from best to worst, were red, NIR, green, red edge, and blue. This tendency was commonly observed regardless of the observation date or flight height. The multispectral cameras of the P4M are arranged in a 3×2 horizontal and vertical pattern. The red and NIR band cameras, which had the best and second-best location estimation accuracy, respectively, are placed in the center of the arrangement, while the green, red-edge, and blue band cameras are placed in the four corners. RTK-measured position information of each spectral camera

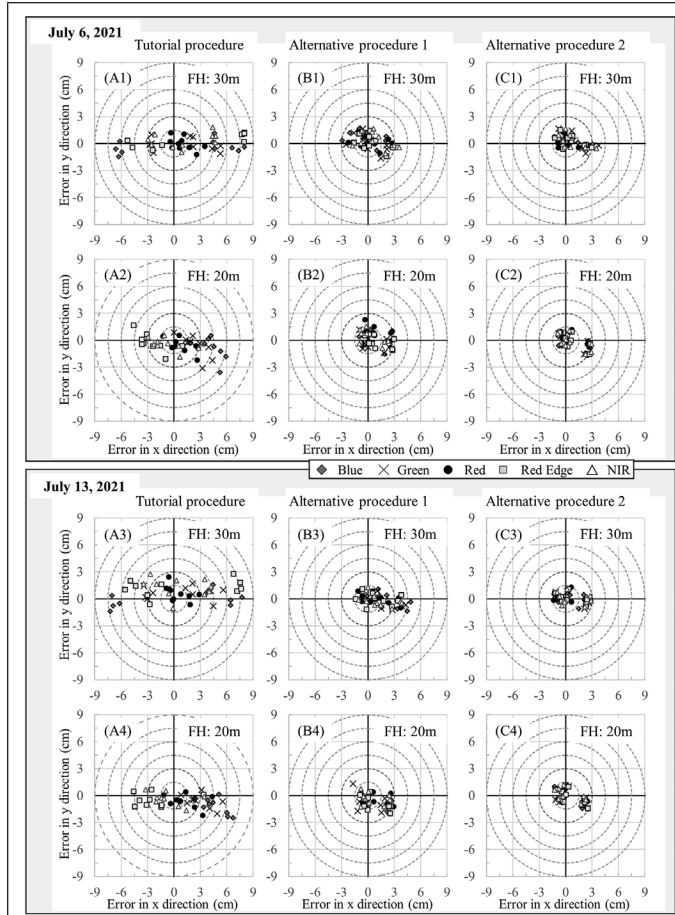


Figure 4. Comparison of GCP location estimation errors by the three procedures (A1–4: tutorial procedure [TP]; B1–4: alternative procedure 1 [AP1]; C1–4: alternative procedure [AP2]) and at different flight heights.

Table 2. Summary of GCP location estimation errors at each spectral band and flight level among the three procedures evaluated on 6 and 13 July 2021.

Date	Flight Height	Band	TP		AP1		AP2	
			30 m	20 m	30 m	20 m	30 m	20 m
			Average (SD), cm					
6 July 2021	30 m	Blue	6.12 (1.19)	4.40 (1.42)	1.78 (0.66)	1.39 (0.79)	1.22 (0.83)	1.36 (1.07)
		Green	3.22 (1.29)	2.68 (1.47)	1.64 (0.73)	1.32 (0.85)	1.43 (1.14)	1.29 (0.97)
		Red	1.42 (1.04)	1.61 (1.11)	1.41 (0.86)	1.77 (0.88)	1.22 (0.67)	1.42 (1.06)
		Red edge	5.22 (2.70)	2.93 (1.16)	1.59 (1.02)	1.48 (1.15)	1.46 (0.79)	1.46 (1.16)
		NIR	2.94 (1.68)	1.87 (0.82)	1.82 (0.92)	1.43 (0.53)	1.46 (0.99)	1.46 (1.19)
		All	3.78 (2.35)	2.70 (1.53)	1.65 (0.83)	1.48 (0.84)	1.36 (0.87)	1.40 (1.04)
13 July 2021	30 m	Blue	6.06 (1.44)	4.84 (1.57)	2.09 (1.73)	1.37 (1.08)	1.27 (0.67)	1.47 (0.67)
		Green	3.36 (1.20)	3.10 (1.63)	1.96 (1.38)	1.54 (0.72)	1.26 (1.00)	1.34 (0.70)
		Red	1.41 (0.91)	1.89 (1.41)	1.66 (1.20)	1.37 (1.06)	1.40 (0.81)	1.29 (0.87)
		Red edge	5.36 (2.14)	3.22 (1.05)	1.80 (1.14)	1.50 (1.16)	1.27 (0.90)	1.32 (0.94)
		NIR	3.04 (1.31)	2.00 (0.88)	1.77 (1.26)	1.33 (0.86)	1.30 (1.03)	1.34 (0.67)
		All	3.85 (2.20)	3.01 (1.67)	1.86 (1.31)	1.42 (0.95)	1.30 (0.85)	1.35 (0.75)

GCP = ground control point; TP = tutorial procedure; AP1 = alternative procedure 1; AP2 = alternative procedure 2; SD = standard deviation; NIR = near infrared.

was individually recorded in the header of TIFF image. Latitude and longitude coordinate information was recorded with a resolution of up to eight decimal places, which corresponded to a millimeter-level of resolution. This implies that the P4M is designed to record GNSS-derived positional information with sufficient resolution to understand the relative positions between individual spectral cameras. Our results suggested that the algorithm used in “multi-camera system” mode in TP may not properly use the precise RTK position information of each spectral camera during internal camera calibration, which may have resulted in systematic alignment errors between spectral bands, at least when using Agisoft Metashape Professional, version 1.7.3, build 12473 (64 bit). Accuracy evaluation in the height direction of the orthomosaic images was not the subject of this study because the height difference between the GCP markers placed on the concrete ground was less than 2.6 cm, which is not sufficient for quantitative verification.

Alignment Error Between Five Spectral Band Images

Table 4 summarizes paired *t*-test results comparing the average distance from the gravity point to the estimated GCP locations (S_{mis}) between TP and AP1 and between AP1 and AP2. The TP-derived alignment error between spectral bands was an order of magnitude larger than those for AP1 and AP2. The average S_{mis} derived from TP was 2.82 cm ($n = 190$), which was 525% to 972% larger than those derived with AP1 (0.52 cm) and AP2 (0.29 cm). The alignment accuracy differed significantly between TP and AP1 and between AP1 and AP2 at the 1% level in two-tailed tests. The misalignment distance of AP2 was 46% smaller than that of AP1. Considering that the average corn and rice leaf widths are approximately 9 and 1 cm, respectively, a few centimeter-level misalignments between spectral bands of multispectral orthomosaic images derived from TP would produce an error of magnitude that cannot be ignored in VI calculations to evaluate leaf color. The results suggested that the additional step in AP2, that is, integrating tie points and GCP markers created separately for the five spectral bands into a merged chunk, effectively reduces the alignment error between spectral band images from AP1.

Figure 5 shows the false color composite of NIR-red-green images and spectral reflectance images of GCP10, Plot 03 (corn), and Plot 07 (rice). The center points of the GCP markers were manually traced with crosshairs for each spectral band and superimposed on a single partial figure. In addition, the boundaries between the background and the vegetation in the middle row were manually traced and superimposed on Plots 03 and 07. As can be seen from the superimposition of the

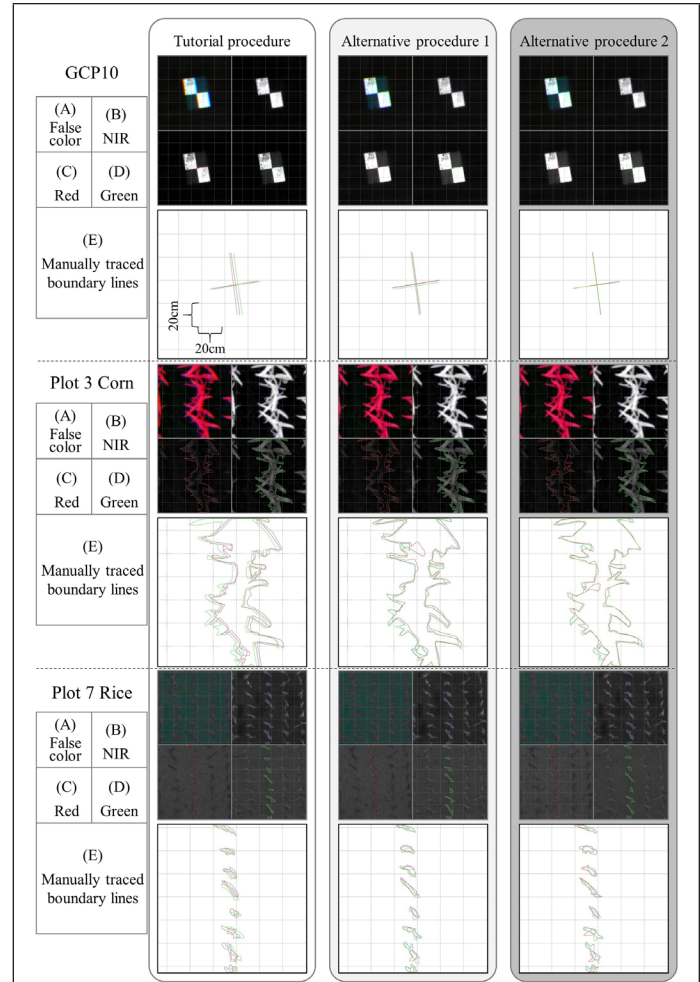


Figure 5. Enlarged false color composite of near-infrared (NIR)-red-green images of Plot 03, Plot 07, and GCP10 (A) on 6 July 2021, spectral band images with manually traced lines of vegetation and center of the ground control point (GCP) marker (B–D) and superimposed images.

Table 3. Average GCP location estimation errors of five spectral bands at each flight level among the three procedures evaluated on 6 and 13 July 2021.

Flight Height (m)	n	TP		Paired <i>t</i> -Test		AP1		Paired <i>t</i> -Test		AP2	
		Mean (V), cm		<i>p</i> -Value		Mean (V), cm		<i>p</i> -Value		Mean (V), cm	
6 July 2021	30	50	3.78 (5.51)		4.79×10^{-7}	**	1.65 (0.68)		2.87×10^{-3}	*	1.36 (0.76)
	20	45	2.70 (2.33)		8.97×10^{-6}	**	1.48 (0.70)		2.89×10^{-1}		1.40 (1.09)
	All	95	3.27 (4.26)		4.97×10^{-11}	**	1.57 (0.69)		2.20×10^{-3}	*	1.38 (0.90)
13 July 2021	30	50	3.85 (4.82)		7.81×10^{-7}	**	1.86 (1.71)		5.32×10^{-5}	**	1.30 (0.73)
	20	45	3.01 (2.80)		5.05×10^{-8}	**	1.42 (0.90)		3.89×10^{-1}		1.35 (0.56)
	All	95	3.45 (4.00)		8.48×10^{-13}	**	1.65 (1.36)		9.04×10^{-5}	**	1.32 (0.64)

GCP = ground control point; TP = tutorial procedure; AP1 = alternative procedure 1; AP2 = alternative procedure 2; V = variance.

* $p < 0.05$, ** $p < 0.01$.

Table 4. Summary of alignment errors between spectral bands at each flight level among the three procedures evaluated on 6 and 13 July 2021.

Flight Height (m)	n	TP		Paired <i>t</i> -Test		AP1		Paired <i>t</i> -Test		AP2	
		Average (SD), cm		<i>p</i> -Value		Average (SD), cm		<i>p</i> -Value		Average (SD), cm	
6 July 2021	30	50	3.42 (5.01)		2.08×10^{-12}	**	0.55 (0.050)		2.62×10^{-3}	**	0.41 (0.048)
	20	45	2.11 (1.49)		3.71×10^{-9}	**	0.67 (0.064)		6.43×10^{-13}	**	0.22 (0.024)
	All	95	2.80 (3.74)		1.78×10^{-18}	**	0.61 (0.059)		1.62×10^{-12}	**	0.32 (0.045)
13 July 2021	30	50	3.43 (4.86)		8.99×10^{-13}	**	0.47 (0.053)		3.97×10^{-6}	**	0.28 (0.025)
	20	45	2.18 (1.86)		4.61×10^{-10}	**	0.46 (0.055)		1.21×10^{-6}	**	0.23 (0.018)
	All	95	2.84 (3.80)		3.64×10^{-20}	**	0.47 (0.054)		1.57×10^{-11}	**	0.26 (0.022)

SD = standard deviation; TP = tutorial procedure; AP1 = alternative procedure 1; AP2 = alternative procedure 2.

* $p < 0.05$, ** $p < 0.01$.

traced lines, the spectral reflectance images derived from TP were misaligned by a few centimeters. The trace lines of AP1 were more closely overlaid than those of TP; however, a misalignment between the red and green band images was still noticeable. The misalignment between spectral band images of AP2 was further reduced compared to that of AP1, especially for GCP10 and Plot 03. The cross lines for GCP10 nearly perfectly overlapped and were centered on the GCP marker. Similar improvement was seen in Plot 03 (corn). As for Plot 07 (rice), there was no obvious improvement in the alignment error between AP1 and AP2, while there was an improvement in AP1 or AP2 versus TP. Possibly, the difference in misalignment could not be visualized by manual tracing, as rice leaves are substantially smaller than corn leaves, making it harder to recognize the edges between the background and vegetation. We cannot conclude whether AP1 or AP2 is more suitable based on visual assessment of Plot 03 alone; however, AP2 provided more accurate coordinate information and reduced the interspectral band misalignment error.

Comparison of Pixel-Level VIs Derived Multispectral Orthomosaic Images Acquired at Different Heights at the Same Location

Figure 6 shows scatter plots of the VIs for the 12 plots ($N = 128 \times 128 \times 12 = 196,608$ pixels) based on multispectral orthomosaic images obtained at different flight heights (20 or 30 m) with the three processing procedures. The TP-derived results (Figure 6A1–6A4) showed the largest data variability and the lowest correlation coefficients regardless of the observation date or VI. The scatter plots obtained with AP2 showed a smaller variability and higher correlation coefficients than those obtained with AP1, especially for CI_{green} (Figure 6B1, 6B2, 6C1, 6C2). However, when using NDVI, there was no obvious difference between the two procedures in terms of degree of agreement (Figure 6B3, 6B4, 6C3, 6C4).

Table 5 summarizes the correlation coefficients between the pixel-level VIs per plot. The correlation coefficients tended to be lower on 13 July than on 6 July for both CI_{green} and NDVI. This was probably due to the limited dynamic range of VI within each plot and vegetation growth in one week. The vegetation cover fraction (i.e., the area percentage of vegetation covering the background area) rapidly increased with the leaf expansion during this phenological stage. Thus, the percentage of vegetated pixels within each plot increased in one week, and the dynamic range of VI was proportionally biased toward vegetated pixels over background pixels. Interestingly, AP2-derived CI_{green} values had the highest correlation coefficients in all plots and on both observation

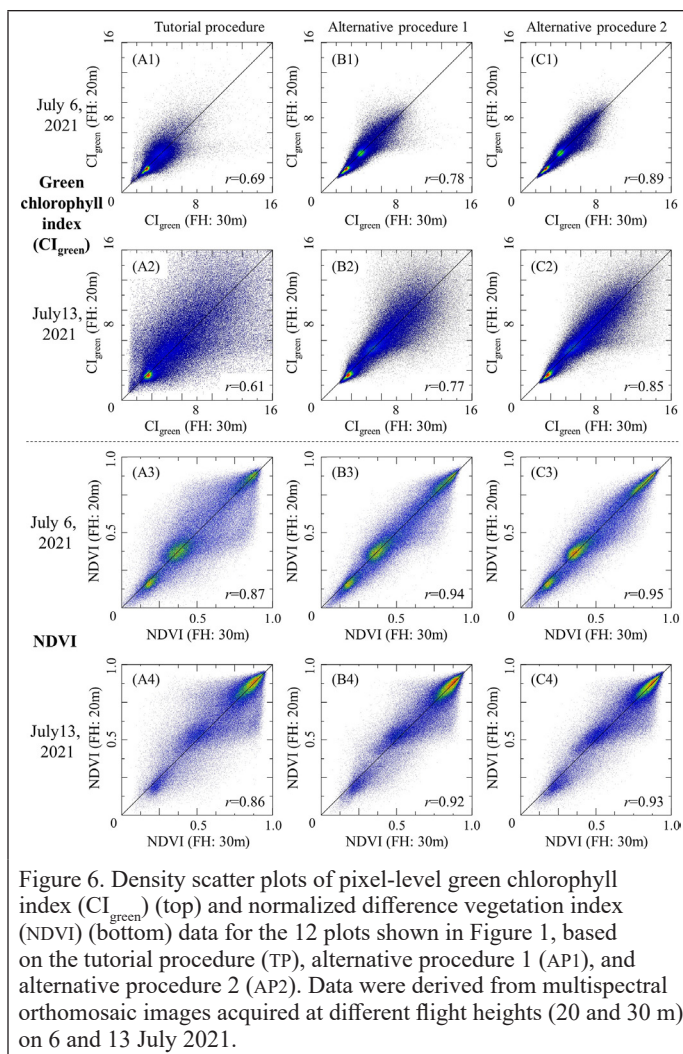


Figure 6. Density scatter plots of pixel-level green chlorophyll index (CI_{green}) (top) and normalized difference vegetation index (NDVI) (bottom) data for the 12 plots shown in Figure 1, based on the tutorial procedure (TP), alternative procedure 1 (AP1), and alternative procedure 2 (AP2). Data were derived from multispectral orthomosaic images acquired at different flight heights (20 and 30 m) on 6 and 13 July 2021.

Table 5. Correlation coefficients of pixel-level CI and NDVI data between multispectral orthomosaic images obtained at 20- and 30-m flight heights.^a

Plot	Crop	Fertilizer (N kg/10 acres)	CI_{green} Correlation Coefficient (r)						NDVI Correlation Coefficient (r)					
			6 July 2021			13 July 2021			6 July 2021			13 July 2021		
			TP	AP1	AP2	TP	AP1	AP2	TP	AP1	AP2	TP	AP1	AP2
1	Corn	0	0.65	0.52	0.80	0.54	0.16	0.56	0.82	0.95	0.97	0.66	0.77	0.76
2		5	0.51	0.56	0.80	0.50	0.43	0.64	0.71	0.88	0.91	0.67	0.71	0.68
3		10	0.62	0.60	0.77	0.56	0.51	0.73	0.81	0.92	0.95	0.70	0.71	0.75
4		15	0.73	0.56	0.79	0.55	0.63	0.71	0.85	0.90	0.95	0.75	0.71	0.78
5		20	0.65	0.53	0.66	0.54	0.49	0.59	0.82	0.91	0.92	0.66	0.61	0.67
6		25	0.71	0.58	0.79	0.71	0.67	0.76	0.81	0.89	0.94	0.80	0.74	0.76
7	Rice	0	0.39	0.68	0.82	0.35	0.62	0.74	0.67	0.82	0.89	0.63	0.44	0.60
8		1	0.69	0.82	0.93	0.57	0.80	0.88	0.82	0.89	0.93	0.73	0.69	0.78
9		2	0.61	0.80	0.87	0.39	0.73	0.77	0.78	0.896	0.901	0.61	0.66	0.65
10		4	0.66	0.85	0.91	0.42	0.74	0.81	0.80	0.95	0.92	0.67	0.77	0.69
11		6	0.58	0.85	0.90	0.39	0.62	0.72	0.78	0.94	0.92	0.73	0.58	0.56
12		8	0.58	0.83	0.83	0.24	0.54	0.60	0.68	0.93	0.87	0.54	0.48	0.40
All			0.69	0.78	0.89	0.61	0.77	0.85	0.87	0.94	0.95	0.86	0.92	0.93

CI = chlorophyll index; NDVI = normalized difference vegetation index; CI_{green} = green chlorophyll index; TP = tutorial procedure; AP1 = alternative procedure 1; AP2 = alternative procedure 2.

^aBoldface values indicate higher correlation coefficients than those obtained with the other procedures.

dates. AP2-derived NDVI values also tended to have higher correlation coefficients than those obtained with the other procedures in most cases. The highest correlation coefficients were observed for plots 1–9 on 6 July and for plots 3–5 and 8 on 13 July.

As shown in Figure 6, NDVI was less sensitive than CI_{green} to absolute and relative misalignment related to the procedure used. The robustness of NDVI to the misalignment problem of multispectral orthomosaic images was highlighted with the increase in vegetative fraction in each plot. The difference in sensitivity of NDVI and CI_{green} to misalignment can be interpreted based on the difference in reflectance between leaf and background. As shown in Figure 5, the contrast between the leaf cover and background in the green reflectance images was higher than that in the red reflectance images, especially for corn (Viña *et al.* 2004). As for NDVI, the NIR reflectance of leaves was approximately 50% and was nearly ten times higher than that of the background, whereas the red reflectance of leaves and background were similar and low (a few percents). Therefore, NDVI is intrinsically less sensitive to changes in red reflectance than to changes in NIR reflectance (Gitelson 2004) given how it is calculated (Equation 5). In contrast, CI_{green} is intrinsically more susceptible to misalignment between these spectral band images, especially at the borders between leaf and background areas, as it considers the ratio of NIR to green reflectance (Equation 4).

Comparison of Region-Averaged VIs Derived from Multispectral Orthomosaic Images Acquired at Different Flight Heights

Figure 7 compares region-averaged VIs derived from orthomosaic images acquired at different heights for the 12 plots using seven different grid sizes. Determination coefficients were calculated using all plot data, without considering the observation dates ($N = 24$ [12 plots \times 2 days]). The determination coefficients obtained with TP were consistently smaller than those obtained with AP1 and AP2 for both CI_{green} and NDVI. AP2 showed the best performance in terms of the degree of agreement of the observed value of region-averaged VIs under different aerial photography conditions, especially for CI_{green} (Figure 7A). The determination coefficients plateaued at a grid size of 32×32 pixels for all three procedures and both VIs. As for the region-averaged NDVI, there were no substantial differences between AP1 and AP2 results (Figure 7B). When focusing on the effect of grid size for region averaging, the determination coefficients for CI_{green} decreased more rapidly than those for NDVI with decreasing grid size. This was also due to the lower sensitivity of NDVI to the alignment error between spectral bands. Even when using TP, the determination coefficient of the region-averaged NDVI based on a 2×2 -pixel grid was high, 0.895, which was 0.15 greater than that of CI_{green} . However, there were still noticeable negative effects of a low alignment accuracy on the observed value of the region-averaged NDVI, especially when comparing TP with the other procedures. Increasing the grid size for region averaging could mitigate the negative effects, and the optimal grid size for the spatial resolution (flight level) of aerial photography using the P4M, which ranges from 1.1 cm/pixel (20 m) to 1.6 cm/pixel (30 m), was 32×32 pixels.

Figure 8 shows scatter plots of region-averaged VIs with the grid size fixed at 32×32 pixels. The RMSEs for rice and corn were compared to investigate the effect of the processing procedure applied on the results. The scatter plot of CI_{green} obtained with TP in Figure 8A1 shows that region-averaged CI_{green} of corn was more affected by misalignment than that of paddy rice (RMSE = 0.61, which was the worst error observed). The difference in the RMSE of CI_{green} between AP1 and AP2 was low; thus, both procedures showed comparable accuracy. In contrast, the 32×32 -pixel-based region-averaged NDVI showed no differences in accuracy regardless of the processing procedure applied or the crop species. This result suggested that calculating region-averaged VIs using a 32×32 -pixel grid size is an effective way to minimize the negative effect of misalignment on observed values, except for the CI_{green} of corn. Moreover, the region-averaged NDVI is more robust to the misalignment problem than CI_{green} regardless of crop species.

This study focused on evaluating the geometric correction results of the proposed procedures and its improvement effect on VIs without a detailed analysis of the effects on radiometric correction. Although Fawcett *et al.* (2020) suggested that drone-derived NDVI had relatively

good agreement with those derived from an airborne imaging spectrometer and an optical satellite image in a maize field, they demonstrated that drone-based hemispherical-conical reflectance factor values exhibited bias when compared to spectroradiometer measurement data, particularly over lower reflective surfaces. Meanwhile, although the commercial SfM/MVS software packages can easily perform radiometric correction, details on their calculation algorithms are not disclosed. Therefore, we believe that further verification of the accuracy of radiometric correction is necessary in future studies.

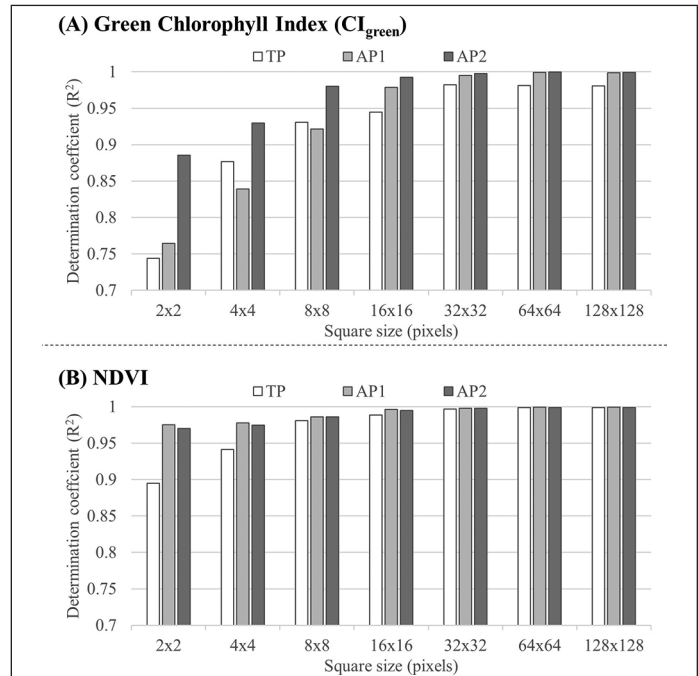


Figure 7. Determination coefficients of region-averaged green chlorophyll index (CI_{green}) (A) and normalized difference vegetation index (NDVI) (B) data based on the tutorial procedure (TP), alternative procedure 1 (AP1), and alternative procedure 2 (AP2). Data were derived from multispectral orthomosaic images acquired at different flight heights.

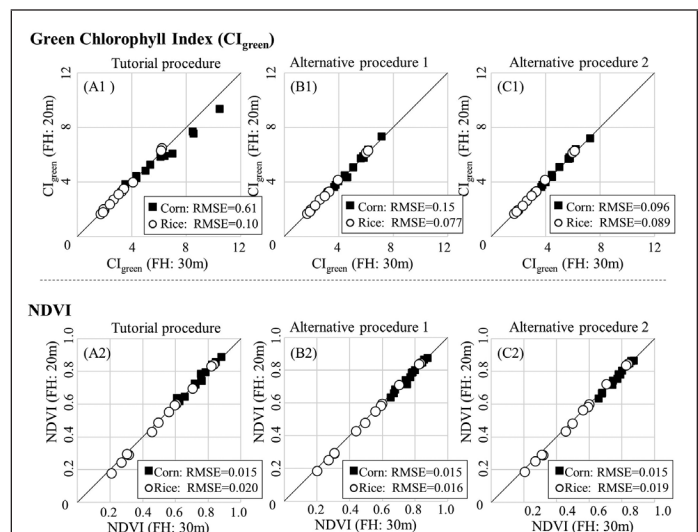


Figure 8. Scatter plots of region-averaged green chlorophyll index (CI_{green}) (A) and normalized difference vegetation index (NDVI) (B) data based on the tutorial procedure (TP), alternative procedure 1 (AP1), and alternative procedure 2 (AP2). Data were derived from multispectral orthomosaic images acquired at different flight heights. The grid size for region averaging was set to 32×32 pixels (32×32 cm).

Conclusion

We examined the location estimation accuracy of three processing procedures to propose an appropriate procedure for creating high-quality multispectral orthomosaic images acquired with the P4M in conjunction with the Agisoft Metashape SIM/MVS software. The standard processing procedure (TP) that can be found on the Agisoft Helpdesk website showed remarkable inaccuracy in terms of location estimation and alignment between spectral band images in this study. The degree of alignment error caused by TP obviously varied depending on the spectral camera. This finding suggested the presence of a program bug in the processing flow of the “multi-camera system” mode of Agisoft Metashape (as of version 1.7.3, build 12473 [64 bit]) that interferes with internal camera calibration using RTK-derived precise position information individually recorded by the multispectral camera. Here, we developed alternative processing procedures (AP1 and AP2) for P4M data analysis using Agisoft Metashape. AP1 uses the “single camera” generic processing mode to individually import P4M-derived aerial images by spectral band to separately create five single-band orthomosaic images. Then the five single-band orthomosaic images are stacked in a single file containing five spectral band images. The location estimation error of AP1 was significantly reduced to about half of that of TP. Compared to using TP, the absolute location estimation accuracy of GCPs for verification in AP1 was significantly improved by the altered procedure, which processed the multispectral images separately by spectral band. AP2 has one more processing step than AP1. It merges the five chunks of tie points and GCP markers created separately for each spectral band into a single chunk and then reconducts internal camera calibration. The alignment accuracy between spectral bands of AP2 was significantly better than that of AP1. We conclude that band-to-band misalignment can be minimized by a second internal camera calibration after integrating tie points and GCP markers preliminarily processed for each spectral band separately. While the mean absolute location estimation error of AP2 was 1.32–1.38 cm, the mean of band-to-band misalignment was 0.26–0.32 cm.

The effect of the differences in the processing procedures on observed NDVI and CI_{green} value was investigated in 12 plots cropped with corn and paddy rice. The use of region-averaged VIs based on at least 32×32-pixel square size was effective to minimize the negative impact of misalignment on observed VI values for all procedures. Overall, AP2 yielded the best location estimation and band alignment accuracy of multispectral orthomosaic images among all procedures evaluated, especially for monitoring corn growth with the P4M drone. The proposed alternative procedure for the Agisoft Metashape software (for version 1.7.3, build 12473 [64 bit]) in conjunction with the P4M contributes to more precise VI analysis in crop breeding and field management in agriculture until the software flaws are fixed.

Acknowledgments

We gratefully acknowledge the support of Takahiro Ara, Toyoshi Omizu, Tomiyama Hirokazu, Naoki Nagata, Misaki Onaka, Yuki Muto, Ryouji Imse, and Dr. Shouji Taniguchi for field experiments and thank Dr. Mizuki Morishita for providing the P4M drone. We offer special thanks to Dr. Tsutomu Kanno, Dr. Yoshihito Sunaga, Yuki Akamatsu, and Kozue Suzuki for providing materials for the corn cultivation experiment. This study was partially supported by a grant from the Ministry of Agriculture, Forestry, and Fisheries of Japan (Smart-Breeding System for Innovative Agriculture, grant BAC1003) to D.O. We also appreciate the valuable comments and suggestions of the anonymous reviewers.

References

Agisoft Helpdesk Portal. 2021. DJI Phantom 4 Multispectral Data Processing. <<https://agisoft.freshdesk.com/support/solutions/articles/31000159853-dji-phantom-4-multispectral-data-processing>> Accessed 19 August 2021.

- Blue Innovation Co. Ltd. 2020. Implementation Report of the Project for Introduction and Demonstration of New Technologies for Forestation—Remote Sensing Training (in Japanese). <https://www.rinya.maff.go.jp/j/seibi/sinrin_seibi/attach/pdf/sinsei_kensa-13.pdf> Accessed 19 August 2021.
- Boegh, E., H. Soegaard, N. Broge, C. B. Hasager, N. O. Jensen, K. Schelde, and A. Thomsen. 2002. Airborne multispectral data for quantifying leaf area index, nitrogen concentration, and photosynthetic efficiency in agriculture. *Remote Sensing of Environment* 81(2–3):179–193.
- Borgogno-Mondino, E., A. Lessio, L. Tarricone, V. Novello, and L. de Palma. 2018. A comparison between multispectral aerial and satellite imagery in precision viticulture. *Precision Agriculture* 19(2):195–217.
- Cai, Y. P., K. Y. Guan, F. Nafziger, G. Chowdhary, B. Peng, Z. N. Jin, S. W. Wang, and S. B. Wang. 2019. Detecting in-season crop nitrogen stress of corn for field trials using UAV- and CubeSat-based multispectral sensing. *IEEE Journal of Selected Topics in Applied Earth Observations and Remote Sensing* 12(12):5153–5166.
- Che, Y. P., Q. Wang, Z. W. Xie, L. Zhou, S. W. Li, F. Hui, X. Q. Wang, B. G. Li, and Y. T. Ma. 2020. Estimation of maize plant height and leaf area index dynamics using an unmanned aerial vehicle with oblique and nadir photography. *Annals of Botany* 126(4):765–773.
- Clevers, J.G.P.W., L. Kooistra, and M.M.M. van den Brande. 2017. Using Sentinel-2 data for retrieving LAI and leaf and canopy chlorophyll content of a potato crop. *Remote Sensing* 9(5):405. <<https://doi.org/10.3390/rs9050405>>.
- Fawcett, D., C. Panigada, G. Tagliabue, M. Boschetti, M. Celesti, A. Evdokimov, K. Biriukova, R. Colombo, F. Miglietta, U. Rascher, and K. Anderson. 2020. Multi-scale evaluation of drone-based multispectral surface reflectance and vegetation indices in operational conditions. *Remote Sensing* 12(3):514. <[doi:10.3390/rs12030514](https://doi.org/10.3390/rs12030514)>.
- Franke, J. and G. Menz. 2007. Multi-temporal wheat disease detection by multi-spectral remote sensing. *Precision Agriculture* 8(3):161–172.
- Gitelson, A. A. 2004. Wide dynamic range vegetation index for remote quantification of biophysical characteristics of vegetation. *Journal of Plant Physiology* 161(2):165–173.
- Gitelson, A. A., S. B. Verma, A. Viña, D. C. Rundquist, G. Keydan, B. Leavitt, T. J. Arkebauer, G. G. Burba, and A. E. Suyker. 2003. Novel technique for remote estimation of CO₂ flux in maize. *Geophysical Research Letters* 30(9):1486. <[doi:10.1029/2002gl016543](https://doi.org/10.1029/2002gl016543)>.
- Gitelson, A. A., A. Viña, V. Ciganda, D. C. Rundquist, and T. J. Arkebauer. 2005. Remote estimation of canopy chlorophyll content in crops. *Geophysical Research Letters* 32(8):L08403. <<https://doi.org/10.1029/2005GL022688>>.
- Guan, S. L., K. Fukami, H. Matsunaka, M. Okami, R. Tanaka, H. Nakano, T. Sakai, K. Nakano, H. Ohdan, and K. Takahashi. 2019. Assessing correlation of high-resolution NDVI with fertilizer application level and yield of rice and wheat crops using small UAVs. *Remote Sensing* 11(2):112. <<https://doi.org/10.3390/rs11020112>>.
- Huang, Y. B., K. N. Reddy, R. S. Fletcher, and D. Pennington. 2018. UAV low-altitude remote sensing for precision weed management. *Weed Technology* 32(1):2–6.
- Inoue, Y. 2020. Satellite-and drone-based remote sensing of crops and soils for smart farming—A review. *Soil Science and Plant Nutrition* 66(6):798–810.
- Inoue, Y., M. Guerif, F. Baret, A. Skidmore, A. Gitelson, M. Schlerf, R. Darvishzadeh, and A. Olioso. 2016. Simple and robust methods for remote sensing of canopy chlorophyll content: A comparative analysis of hyperspectral data for different types of vegetation. *Plant Cell and Environment* 39(12):2609–2623.
- Maas, S. J. and N. Rajan. 2008. Estimating ground cover of field crops using medium-resolution multispectral satellite imagery. *Agronomy Journal* 100(2):320–327.
- Maes, W.H. and Steppe, K., 2019. Perspectives for remote sensing with unmanned aerial vehicles in precision agriculture. *Trends in Plant Science* 24(2):152–164.
- Malambo, L., S. C. Popescu, S.C. Murray, E. Putman, N. A. Pugh, D. W. Horne, G. Richardson, R. Sheridan, W. L. Rooney, R. Avant, M. Vidrinec, B. McCutchen, D. Baltensperger, and M. Bishop. 2018. Multitemporal field-based plant height estimation using 3D point clouds generated from small unmanned aerial systems high-resolution imagery. *International Journal of Applied Earth Observation and Geoinformation* 64:31–42.
- Managhani, B. and C. Salvaggio. 2019. Multispectral sensor calibration and characterization for sUAS remote sensing. *Sensors* 19(20):4453. <<https://doi.org/10.3390/s19204453>>.

- McKinnon, T., 2016. *Agricultural Drones: What Farmers Need to Know*. Agribotix white papers. <https://agribotix.com/whitepapers/farmers-need-know-agricultural-drones>.
- Monteith, J. L. 1972. Solar-radiation and productivity in tropical ecosystems. *Journal of Applied Ecology* 9(3):747–766.
- Morimoto, E. and K. Hayashi. 2017. Design of smart agriculture Japan model. *Advances in Animal Biosciences* 8(2):713–717.
- Ogawa, D., T. Sakamoto, H. Tsunematsu, N. Kanno, Y. Nonoue, and J. I. Yonemaru. 2021. Haplotype analysis from unmanned aerial vehicle imagery of rice MAGIC population for the trait dissection of biomass and plant architecture. *Journal of Experimental Botany* 72(7):2371–2382.
- Ogawa, D., T. Sakamoto, H. Tsunematsu, T. Yamamoto, N. Kanno, Y. Nonoue, and J. Yonemaru. 2019. Surveillance of panicle positions by unmanned aerial vehicle to reveal morphological features of rice. *PLoS One* 14(10): e0224386. <<https://doi.org/10.1371/journal.pone.0224386>>.
- Osaki, K., 2019. Utilization of digital cameras for proximal remote sensing. *Nihon Gazo Gakkaiishi* 58(6):651–658.
- Peng, Y. and A. A. Gitelson. 2011. Application of chlorophyll-related vegetation indices for remote estimation of maize productivity. *Agricultural and Forest Meteorology* 151(9):1267–1276.
- Peng, Y. and A. A. Gitelson. 2012. Remote estimation of gross primary productivity in soybean and maize based on total crop chlorophyll content. *Remote Sensing of Environment* 117:440–448.
- Peter, B. G., J. P. Messina, J. W. Carroll, J. J. Zhi, V. Chimonyo, S. P. Lin, and S. S. Snapp. 2020. Multi-spatial resolution satellite and sUAS imagery for precision agriculture on smallholder farms in Malawi. *Photogrammetric Engineering and Remote Sensing* 86(2):107–119.
- Qi, H., Z. Wu, L. Zhang, J. Li, J. Zhou, Z. Jun, and B. Zhu. 2021. Monitoring of peanut leaves chlorophyll content based on drone-based multispectral image feature extraction. *Computers and Electronics in Agriculture* 187:106292.
- Reynolds, M., S. Chapman, L. Crespo-Herrera, G. Molero, S. Mondal, D.N.L. Pequeno, F. Pinto, F. J. Pinera-Chavez, J. Poland, C. Rivera-Amado, C. Saint Pierre, and S. Sukumaran. 2020. Breeder friendly phenotyping. *Plant Science* 295:110396.
- Rouse, J. W., R. H. Haas, J. A. Schell, and D. W. Deering. 1974. Monitoring vegetation systems in the Great Plains with ERTS. *NASA Special Publication* 351(1974):309.
- Saiz-Rubio, V. and F. Rovira-Más. 2020. From smart farming towards agriculture 5.0: A review on crop data management. *Agronomy* 10(2):207.
- Sakamoto, T., A. A. Gitelson, A. L. Nguy-Robertson, T. J. Arkebauer, B. D. Wardlow, A. E. Suyker, S. B. Verma, and M. Shibayama. 2012. An alternative method using digital cameras for continuous monitoring of crop status. *Agricultural and Forest Meteorology* 154:113–126.
- Schlemmer, M., A. Gitelson, J. Schepers, R. Ferguson, Y. Peng, J. Shanahan, and D. Rundquist. 2013. Remote estimation of nitrogen and chlorophyll contents in maize at leaf and canopy levels. *International Journal of Applied Earth Observation and Geoinformation* 25:47–54.
- Shibayama, M., T. Sakamoto, E. Takada, A. Inoue, K. Morita, T. Yamaguchi, W. Takahashi, and A. Kimura. 2012. Estimating rice leaf greenness (SPAD) using fixed-point continuous observations of visible red and near infrared narrow-band digital images. *Plant Production Science* 15(4):293–309.
- Sun, G. X., X. C. Wang, Y. Q. Ding, W. Lu, and Y. Sun. 2019. Remote measurement of apple orchard canopy information using unmanned aerial vehicle photogrammetry. *Agronomy-Basel* 9(11):774.
- Svensgaard, J., S. M. Jensen, S. Christensen, and J. Rasmussen. 2021. The importance of spectral correction of UAV-based phenotyping with RGB cameras. *Field Crops Research* 269:9840192.
- Taddia, Y., F. Stecchi, and A. Pellegrinelli. 2020. Coastal mapping using DJI Phantom 4 RTK in post-processing kinematic mode. *Drones* 4(2):9.
- Tang, Z., A. Parajuli, C. J. Chen, Y. Hu, S. Revolinski, C. A. Medina, S. Lin, Z. W. Zhang, and L. X. Yu. 2021. Validation of UAV-based alfalfa biomass predictability using photogrammetry with fully automatic plot segmentation. *Scientific Reports* 11(1):3336.
- Thenkabail, P. S., A. D. Ward, and J. G. Lyon. 1994. Impacts of agricultural management-practices on soybean and corn crops evident in ground-truth data and thematic mapper vegetation indexes. *Transactions of the ASAE* 37(3):989–995.
- Vargas, J.J.Q., C. Y. Zhang, J. A. Smitchger, R. J. McGee, and S. Sankaran. 2019. Phenotyping of plant biomass and performance traits using remote sensing techniques in pea (*Pisum sativum*, L.). *Sensors* 19(9):2031.
- Veroustraete, F. 2015. The rise of the drones in agriculture. *EC Agriculture* 2(2):325–327.
- Viña, A., A. A. Gitelson, D. C. Rundquist, G. Keydan, B. Leavitt, and J. Schepers. 2004. Remote sensing—Monitoring maize (*Zea mays* L.) phenology with remote sensing. *Agronomy Journal* 96(4):1139–1147.
- Wu, C. Y., Z. Niu, and S. Gao. 2012. The potential of the satellite derived green chlorophyll index for estimating midday light use efficiency in maize, coniferous forest and grassland. *Ecological Indicators* 14(1):66–73.
- Zhang, C. Y., W. A. Craine, R. J. McGee, G. J. Vandemark, J. B. Davis, J. Brown, S. H. Hulbert, and S. Sankaran. 2020. Image-based phenotyping of flowering intensity in cool-season crops. *Sensors* 20(5):1450.
- Zhang, Q. Y., Y. B. Cheng, A. I. Lyapustin, Y. J. Wang, X. Y. Zhang, A. Suyker, S. Verma, Y. M. Shuai, and E. M. Middleton. 2015. Estimation of crop gross primary production (GPP): II. Do scaled MODIS vegetation indices improve performance? *Agricultural and Forest Meteorology* 200:1–8.

Robust Dynamic Indoor Visible Light Positioning Method Based on CMOS Image Sensor

Senzhen Sun, Guangyun Li, Yangjun Gao, and Li Wang

Abstract

A real-time imaging recognition and positioning method based on visible light communication flat light source is proposed. This method images the visible light communication flat light source through the rolling shutter effect of the complementary metal-oxide semiconductor imaging sensor and obtains the rectangular area outline of the light source. The light and dark stripe information of image with the digital image processing method realizes light source matching recognition by defining the concept, the autocorrelation sequence, which can be used to obtain the identity of the light source, and the rectangular vertex coordinate information of flat light source achieves high-precision vision positioning on the basis of inertial measurement unit attitude sensor-assisted imaging. Simultaneously, the corresponding positioning module is developed for positioning testing. The test results indicate that the plane positioning error is less than 4.5 cm, and the positioning frequency is greater than 10 Hz, which provides a high-precision visual positioning solution for indoor positioning.

Introduction

With the development of urbanization, the demand for indoor positioning technology is increasing in areas such as large building venues, automated factories, underground spaces, and so on. The global satellite navigation system can basically meet the navigation and positioning requirements in most outdoor areas, but it cannot work indoors because of the difficulty in receiving satellite signals. Therefore, base station wireless indoor positioning technologies based on Wi-Fi, Bluetooth, ultrawide band (UWB), pseudosatellite, radio frequency, and so on came into being (Li *et al.* 2020). However, indoor structure is diverse and the electromagnetic environment is complex. Taking the UWB base station-type wireless indoor positioning solution as an example, it needs to set additional positioning base stations, dedicated receiving equipment, special data processing center, and dedicated personnel maintenance. This kind of base station wireless indoor positioning technology requires a balance between positioning accuracy and operation cost, and its versatility is poor. With the development of deep learning technology, indoor positioning methods based on multi-sensor fusion technologies such as semantic simultaneous localization and mapping (SLAM) have made great progress (Huang *et al.* 2021), but the engineering application of large-scale SLAM technology is difficult to adapt to dynamic application scenarios (Shao *et al.* 2019), and absolute position calibration is required. With the wide application of the light-emitting diode (LED) lighting system, the indoor positioning technology based on visible light communication technology shows the prospect of a broad application. For example, the visible light positioning (VLP) system based on imaging has fewer changes to the environment, takes both lighting and positioning into account, and has the advantages of high positioning accuracy, low system cost, no

electromagnetic interference (Luo *et al.* 2017), and is very suitable for mobile robot position calibration.

The implementation models of indoor visible light communication positioning technologies are mainly divided into imaging methods and nonimaging methods according to the types of receivers. The nonimaging positioning method of visible light communication mainly uses the photodiode (PD) at the receiving terminal to receive and analyze the signals and intensity information of multiple light sources to achieve visible light localization; its main implementation methods include the fingerprint matching method and geometric measurement method (Yan *et al.* 2019; Amsters *et al.* 2021; Li *et al.* 2018; Almadani *et al.* 2021; Zheng *et al.* 2017). The image sensor-based visible light communication positioning method mainly includes LED-identification (LED-IDs) (Xie *et al.* 2018) and imaging measurement. LEDs transmit IDs or geographical location information mainly by using the rolling shutter mechanism of complementary metal-oxide-semiconductor (CMOS) sensors (Do and Yoo 2016; Chen *et al.* 2017; Ma *et al.* 2019; Guan *et al.* 2018). On the other hand, the imaging positioning method is based on the principle of photography to achieve positioning, which is to perform imaging measurements on the light source by recognizing and detecting the geometric key points of the light source through digital image processing technology, and by determining the spatial relationship between the camera and the light source according to the photographic geometric relationship (Guan *et al.* 2019). The image sensor-based visible light communication imaging positioning method shows high positioning accuracy and strong portability, while the PD-based visible light communication imaging positioning method shows high positioning rate, but it shows complicated systematic design and poor portability. With the wide application of CMOS imaging sensors in smart terminals, the visible light communication positioning method based on mobile phone imaging has achieved more research and application results (Zhang *et al.* 2019; Wu *et al.* 2019; Ji *et al.* 2019; Kim *et al.* 2016; Sun *et al.* 2020).

Aiming at the decoding problem of visible light communication imaging, Do and Yoo (2016) systematically analyzed the imaging communication mechanism of CMOS sensor's rolling shutter, Chen *et al.* (2017), Ma *et al.* (2019), and Guan *et al.* (2018) analyzed the communication demodulation method based on the rolling shutter of the CMOS sensor, and discussed the method of reducing the bit-free rate. In terms of light source ID recognition, Xie *et al.* (2018) converted the identification of light source ID into an image classification problem and realized the recognition of light source. As for the application research, Guan *et al.* (2019) achieved the positioning accuracy of 4.38 cm by simultaneously recognizing three LED light sources based on the light source image classification and recognition method. Zhang *et al.* (2019) proposed an LED-optical fringe code (OFC) modulation and recognition algorithm using red, green, blue (RGB)-LED as a positioning light source; meanwhile, a Convolution Neural Network was used to recognize light source images, which improved the recognition accuracy and recognition distance of light source. Wu *et al.* (2019) comprehensively considered the positioning accuracy, robustness, and

Senzhen Sun, Guangyun Li, Yangjun Gao, and Li Wang are with the School of Geospatial Information, Information Engineering University, Zhengzhou, Henan 450001, China (guangyun_li_chxy@163.com).

Yangjun Gao and Li Wang are also with the State Key Laboratory of Geo-Information Engineering, Xi'an, Shaanxi 710054, China..

Contributed by Bo Wu, October 6, 2021 (sent for review November 4, 2021; reviewed by Yaxin Li, Shengjun Tang).

Photogrammetric Engineering & Remote Sensing
Vol. 88, No. 5, May 2022, pp. 333–342.
0099-1112/22/333–342

© 2022 American Society for Photogrammetry
and Remote Sensing
doi: 10.14358/PERS.21-00077R3

**PEER-REVIEWED CONTENT
IS ONLY AVAILABLE TO
ASPRS MEMBERS AND SUBSCRIBERS**

**FOR MORE INFORMATION VISIT
MY.ASPRS.ORG**

**PEER-REVIEWED CONTENT
IS ONLY AVAILABLE TO
ASPRS MEMBERS AND SUBSCRIBERS**

**FOR MORE INFORMATION VISIT
MY.ASPRS.ORG**

**PEER-REVIEWED CONTENT
IS ONLY AVAILABLE TO
ASPRS MEMBERS AND SUBSCRIBERS**

**FOR MORE INFORMATION VISIT
MY.ASPRS.ORG**

**PEER-REVIEWED CONTENT
IS ONLY AVAILABLE TO
ASPRS MEMBERS AND SUBSCRIBERS**

**FOR MORE INFORMATION VISIT
MY.ASPRS.ORG**

**PEER-REVIEWED CONTENT
IS ONLY AVAILABLE TO
ASPRS MEMBERS AND SUBSCRIBERS**

**FOR MORE INFORMATION VISIT
MY.ASPRS.ORG**

**PEER-REVIEWED CONTENT
IS ONLY AVAILABLE TO
ASPRS MEMBERS AND SUBSCRIBERS**

**FOR MORE INFORMATION VISIT
MY.ASPRS.ORG**

**PEER-REVIEWED CONTENT
IS ONLY AVAILABLE TO
ASPRS MEMBERS AND SUBSCRIBERS**

**FOR MORE INFORMATION VISIT
MY.ASPRS.ORG**

**PEER-REVIEWED CONTENT
IS ONLY AVAILABLE TO
ASPRS MEMBERS AND SUBSCRIBERS**

**FOR MORE INFORMATION VISIT
MY.ASPRS.ORG**

**PEER-REVIEWED CONTENT
IS ONLY AVAILABLE TO
ASPRS MEMBERS AND SUBSCRIBERS**

**FOR MORE INFORMATION VISIT
MY.ASPRS.ORG**

Comparing the Sensitivity of Pixel-Based and Sub-Watershed-Based Analytic Hierarchy Process to Weighting Criteria for Flood Hazard Estimation

Hongping Zhang, Zhenfeng Shao, Wenfu Wu, Xiao Huang, Jisong Sun, Jinqi Zhao, and Yewen Fan

Abstract

In flood hazard estimation via the analytic hierarchy process (AHP), using the pixel as the basic unit might lead to accuracy relying on the optimal weighting criteria. To this end, considering the sub-watershed as the basic unit is new. In this study, taking the Chaohu Basin in Anhui Province, China, as a study case, the accuracy of the sensitivity of the pixel-based and sub-watershed-based AHP models influenced by weighting criteria was compared. There were 48 judgment matrices defined, following the same order of importance of the involved indicators. Validation ground truthing is constructed by the extracted flooded regions from GF-3 images. As weighting criteria changed, the results indicated that the pixel-based AHP fluctuated significantly, while the correct ratio and fit ratio derived by the sub-watershed-based AHP could improve by >35% and >5%, respectively, over the pixel-based-AHP. It indicated that the sub-watershed-based AHP has an advantage in relying less on in situ weighting criteria than the pixel-based AHP.

Introduction

Floods are worldwide natural events that commonly occur in river networks in interwoven areas, driven by extreme or continuous rainfall. These low-lying areas have a high risk of flood and waterlogging. Meanwhile, the abundant water resources bring convenience to agricultural irrigation and commercial transportation. Most of the interwoven river areas have long histories of human inhabitants. Therefore, to improve the accuracy of flood hazard estimation in river networks, interwoven areas can support better flood risk management practices.

Hongping Zhang is with the State Key Laboratory of Information Engineering in Surveying, Mapping and Remote Sensing, Wuhan University, Wuhan 430079, China; and State Key Laboratory of Severe Weather, Chinese Academy of Meteorological Sciences, Beijing 100081, China.

Zhenfeng Shao is with the State Key Laboratory of Information Engineering in Surveying, Mapping and Remote Sensing, Wuhan University, Wuhan 430079, China.

Wenfu Wu is with the State Key Laboratory of Information Engineering in Surveying, Mapping and Remote Sensing, Wuhan University, Wuhan 430079, China.

Xiao Huang is with the Department of Geosciences, University of Arkansas, Fayetteville, AR 72701.

Jisong Sun is with the State Key Laboratory of Severe Weather, Chinese Academy of Meteorological Sciences, Beijing 100081, China.

Jinqi Zhao is with the School of Environment Science and Spatial Informatics, China University of Mining and Technology, Xuzhou 221116, China.

Yewen Fan is with the State Key Laboratory of Information Engineering in Surveying, Mapping and Remote Sensing, Wuhan University, Wuhan 430079, China.

Contributed by Desheng Liu, October 20, 2021 (sent for review November 29, 2021; reviewed by Ashraf Dewan, Neema Nicodemus Lyimo).

The analytic hierarchy process (AHP) is a popular multi-criteria decision method used in flood hazard estimation. The AHP method relies on expert knowledge to determine involving indices and corresponding criteria (Liu *et al.* 2021). In AHP, the judgment matrix definition determines the final weighting (Saaty 2014), and the weighting might lead to impact flood hazard estimation results (Ohnishi and Imai 1998; Ohnishi *et al.* 2011). As in landslide detecting, Adnan *et al.* (2020) addressed that the uncertainties in the results derived by various models would create challenges in landslide management.

Efforts are still needed to reduce the impact of criteria weight sensitivity on flood hazard estimation results. For example, Koc *et al.* (2021) used a fuzzy AHP method to identify the weight of used criteria. Rahman *et al.* (2021) used the hydrodynamic model coupled with a machine learning algorithm to create a flood hazard map. Costache *et al.* (2020) focused on a combination of AHP, certainty factor, and weights of evidence on the one hand and gradient boosting trees and multi-layer perceptron on the other to evaluate flood potential areas. Ali *et al.* (2020) developed a framework for identifying flood-prone areas using geographic information systems (GIS), a multi-criteria decision making approach, bivariate statistics, and machine learning.

With spatial information techniques, flood hazard estimation can produce involved indicators by GIS and remote sensing images and using the pixel as the basic unit to prepare flood hazard estimation-related indices. The sub-watershed is a boundary reflecting pixels flowing out from the same outlets, and the sub-watershed is always considered as a basic unit to simulate rainfall-runoff processes (Abdulkareem *et al.* 2018; Shao *et al.* 2019; Wang *et al.* 2020; Zhang *et al.* 2020). Therefore, using the sub-watershed as the basic unit in AHP-based flood hazard estimation may capture the terrain features or hydrological characteristics introduced by neighborhood cells at the sub-watershed scale (Zhang *et al.* 2020; Betancourt *et al.* 2021). The sub-watershed has been widely used as the basic unit in hydrology process simulation by hydrology or numerical models, but it is new use it as a basic unit in flood hazard estimation (sub-watershed-based AHP). As a sub-watershed is a group of pixels, taking the sub-watershed as the basic unit to estimate flood hazard may reduce the uncertainty caused by weighting changes compared to using individual pixels as the basic unit. Therefore, this study aims to compare the sensitivity caused by weighting criteria definition between pixel-based AHP and sub-watershed-based AHP.

However, flood hazard map derived by AHP may choose different kinds of indices and thus might lead to individual weighting in different research. In some works (Bathrellos *et al.* 2017; Ghosh and Kar 2018; Kanani-Sadat *et al.* 2019; Shariat *et al.* 2019; Mishra and Sinha 2020; Nachappa *et al.* 2020; Nguyen *et al.* 2020; Ekmekcioglu *et al.* 2021; Pham *et al.* 2021), flood hazard estimation indices consisted of direct flood-caused factors (i.e., rainfall), runoff converging factors (i.e., slope, elevation, and water systems), and surface runoff production characters (i.e., land use type and impervious surfaces). Meanwhile, similar indices,

Photogrammetric Engineering & Remote Sensing
Vol. 88, No. 5, May 2022, pp. 343–352.
0099-1112/22/343–352

© 2022 American Society for Photogrammetry
and Remote Sensing
doi: 10.14358/PERS.21-00087R2

**PEER-REVIEWED CONTENT
IS ONLY AVAILABLE TO
ASPRS MEMBERS AND SUBSCRIBERS**

**FOR MORE INFORMATION VISIT
MY.ASPRS.ORG**

**PEER-REVIEWED CONTENT
IS ONLY AVAILABLE TO
ASPRS MEMBERS AND SUBSCRIBERS**

**FOR MORE INFORMATION VISIT
MY.ASPRS.ORG**

**PEER-REVIEWED CONTENT
IS ONLY AVAILABLE TO
ASPRS MEMBERS AND SUBSCRIBERS**

**FOR MORE INFORMATION VISIT
MY.ASPRS.ORG**

**PEER-REVIEWED CONTENT
IS ONLY AVAILABLE TO
ASPRS MEMBERS AND SUBSCRIBERS**

**FOR MORE INFORMATION VISIT
MY.ASPRS.ORG**

**PEER-REVIEWED CONTENT
IS ONLY AVAILABLE TO
ASPRS MEMBERS AND SUBSCRIBERS**

**FOR MORE INFORMATION VISIT
MY.ASPRS.ORG**

**PEER-REVIEWED CONTENT
IS ONLY AVAILABLE TO
ASPRS MEMBERS AND SUBSCRIBERS**

**FOR MORE INFORMATION VISIT
MY.ASPRS.ORG**

**PEER-REVIEWED CONTENT
IS ONLY AVAILABLE TO
ASPRS MEMBERS AND SUBSCRIBERS**

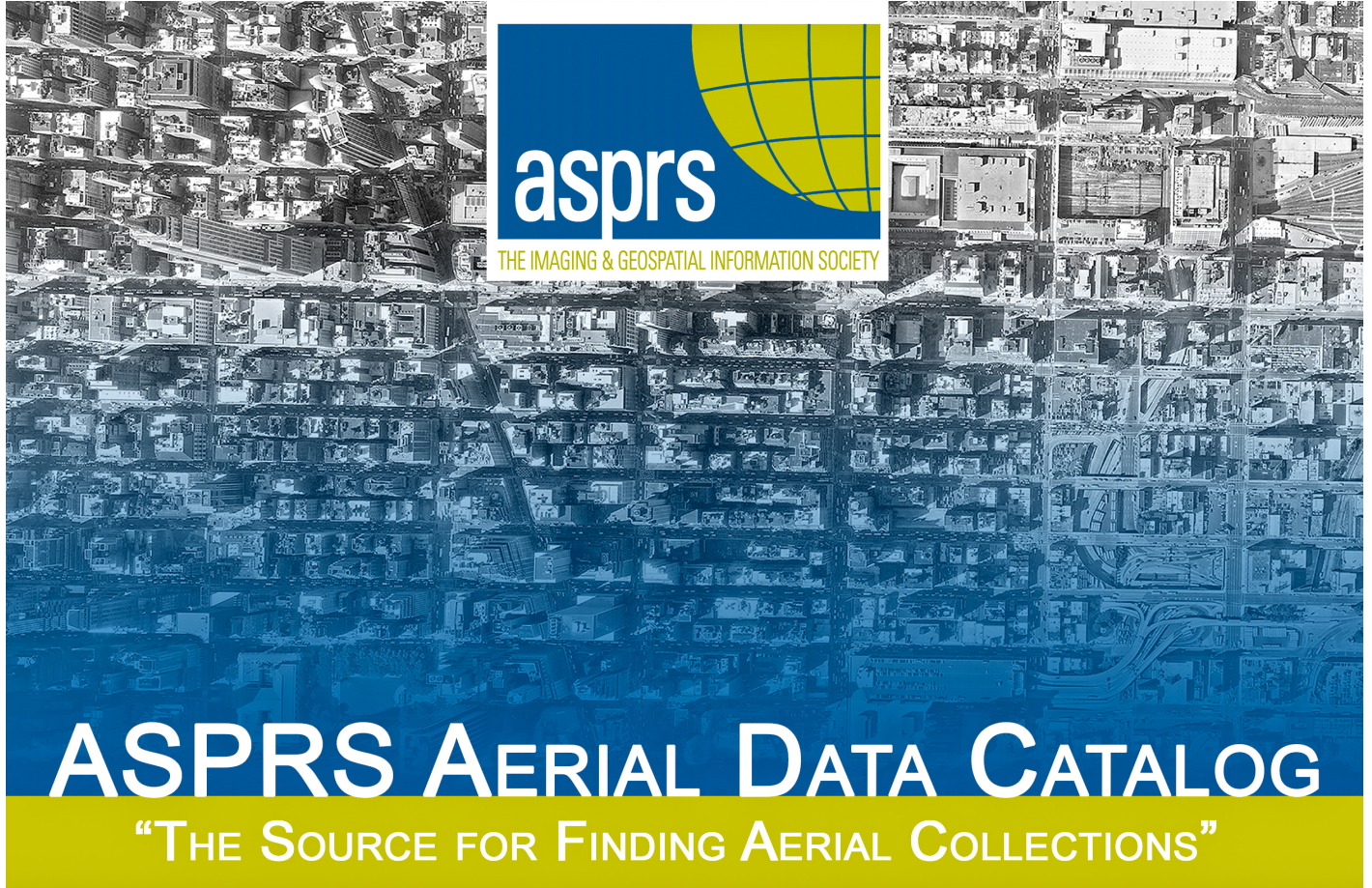
**FOR MORE INFORMATION VISIT
MY.ASPRS.ORG**

**PEER-REVIEWED CONTENT
IS ONLY AVAILABLE TO
ASPRS MEMBERS AND SUBSCRIBERS**

**FOR MORE INFORMATION VISIT
MY.ASPRS.ORG**

**PEER-REVIEWED CONTENT
IS ONLY AVAILABLE TO
ASPRS MEMBERS AND SUBSCRIBERS**

**FOR MORE INFORMATION VISIT
MY.ASPRS.ORG**



[HTTP://DPAC.ASPRS.ORG](http://dpac.asprs.org)

The ASPRS Aerial Data Catalog is a tool allowing owners of aerial photography to list details and contact information about individual collections.

By providing this free and open metadata catalog with no commercial interests, the Data Preservation and Archiving Committee (DPAC) aims to provide a definitive metadata resource for all users in the geospatial community to locate previously unknown imagery.

DPAC hopes this Catalog will contribute to the protection and preservation of aerial photography around the world!

ASPRS Members: We Need Your Help!
There are three ways to get involved

1

USE

Use the catalog to browse over 5,000 entries from all 50 states and many countries. Millions of frames from as early as 1924!

2

SUPPLY

Caretakers of collections, with or without metadata, should contact DPAC to add their datasets to the catalog free of charge!

3

TELL

Spread the word about the catalog! New users and data collections are key to making this a useful tool for the community!

For More Details or To Get Involved Contact:

DAVID RUIZ • DRUIZ@QUANTUMSPATIAL.COM • 510-834-2001 OR DAVID DAY • DDAY@KASURVEYS.COM • 215-677-3119

LEARN
DO
GIVE
BELONG

ASPRS Offers

- » Cutting-edge conference programs
- » Professional development workshops
- » Accredited professional certifications
- » Scholarships and awards
- » Career advancing mentoring programs
- » *PE&RS*, the scientific journal of ASPRS

asprs.org

ASPRS